

University of Central Florida

STARS

Electronic Theses and Dissertations

2018

The Formation and Characterization of Mesoscopic J- and H-aggregates with Controlled Morphologies by the Co- and Templated Assembly of Cyanine Dyes

Samuel Rhodes

University of Central Florida



Part of the [Materials Science and Engineering Commons](#)

Find similar works at: <https://stars.library.ucf.edu/etd>

University of Central Florida Libraries <http://library.ucf.edu>

This Doctoral Dissertation (Open Access) is brought to you for free and open access by STARS. It has been accepted for inclusion in Electronic Theses and Dissertations by an authorized administrator of STARS. For more information, please contact STARS@ucf.edu.

STARS Citation

Rhodes, Samuel, "The Formation and Characterization of Mesoscopic J- and H-aggregates with Controlled Morphologies by the Co- and Templated Assembly of Cyanine Dyes" (2018). *Electronic Theses and Dissertations*. 6245.

<https://stars.library.ucf.edu/etd/6245>

THE FORMATION AND CHARACTERIZATION OF MESOSCOPIC J- AND H-
AGGREGATES WITH CONTROLLED MORPHOLOGIES BY THE CO- AND TEMPLATED
ASSEMBLY OF CYANINE DYES

by

SAMUEL H. RHODES
B.S. Lycoming College, 2014

A dissertation submitted in partial fulfillment of the requirements
for the degree of Doctor of Philosophy
in the Department of Materials Science and Engineering
in the College of Engineering and Computer Science
at the University of Central Florida
Orlando, Florida

Spring Term
2018

Major Professor: Jiyu Fang

© 2018 Samuel H Rhodes

ABSTRACT

The supramolecular aggregates of π -conjugated molecules have become an area of great interest to the scientific community in recent years for their promise in biosensors and optoelectronic devices. Among various supramolecular aggregates, J- and H-aggregates of π -conjugated dye molecules are particularly interesting because of their unique optical and excitonic properties that are not given by individual molecules. H-aggregates are composed of dye molecules in a face-to-face stacking, giving rise to a blue-shifted absorption band compared with the monomer band and a strong emission quenching. In contrast, J-aggregates represent an edge-to-edge stacking of dye molecules, showing a red-shifted absorption band with respect to the monomer band and a strong fluorescence emission. However, the use of J- and H-aggregates in biosensors and optoelectronic devices remains a challenge because of the difficulty of controlling their sizes and morphologies.

In this dissertation, we develop two different paths for controlling the size and morphology of J- and H-aggregates. First, we show that the co-assembly of cyanine dyes and lithocholic acid (LCA) in ammonia solution can lead to the formation of mesoscopic J- and H-aggregate fibers, depending on the condition under which the co-assembly occurs. Second, we report the formation of mesoscopic J-aggregate tubes by using the preformed LCA tubes as a template. The structure, optical, and electronic properties of these J- and H-aggregate fiber and tubes are studied as a function of temperature. Finally, we exploit their applications as photo-induced electron transfer supramolecular probes for the detection of dopamine, an important neurotransmitter in central and peripheral nervous systems.

To my parents, for their constant support and encouragement.

To my sisters; Alaina, Kara, and Madison.

To my friends, for keeping me sane throughout this process.

I can't thank you all enough.

ACKNOWLEDGMENTS

I would first like to thank my advisor, Dr. Jiyu Fang, for without his patient guidance and unyielding support, I would not have made it to this point. His valuable insight and thought discussions have been invaluable to my success. I would also like to thank Dr. Stephen Florczyk, Dr. Tengfei Jiang, Dr. Yajie Dong, and Dr. Shuo Pang for serving on my dissertation committee and for their encouragement and valuable comments.

I would also like to thank my colleagues Dr. Wenlang Liang and Dr. Xiaochen Wang for their help and support while conducting experiments.

Lastly, but not least, I would like to thank my friends and family. Without a strong base of friends from my undergraduate institution I would not have successfully navigated the sometimes-treacherous waters of graduate school. The friends that I have gained here in Orlando were integral to keeping me sane throughout the graduate school experience. I would especially like to thank my parents. They have constantly and unwaveringly supported me my entire life and without their love and support I would have undoubtedly fallen well short of achieving my goals.

TABLE OF CONTENTS

LIST OF FIGURES	ix
CHAPTER 1: INTRODUCTION	1
1.1 Bile Acids	1
1.2 Self-Assembly of Amphiphilic Molecules	3
1.3 Light Harvesting Systems and H-/J-Aggregates of Cyanine Dyes	8
CHAPTER 2: FORMATION OF SPHERULITIC J-AGGREGATES FROM THE CO- ASSEMBLY OF LITHOCHOLIC ACID AND CYANINE DYE.....	14
2.1 Introduction.....	14
2.2 Experimental Methods	15
2.3 Results and Discussion	18
CHAPTER 3: CONTROLLED FORMATION OF J- AND H-AGGREGATE FIBERS BY THE CO-ASSEMBLY OF CYANINE DYES AND BILE ACIDS	33
3.1 Introduction.....	33
3.2 Experimental	35
3.2.1 Materials	35
3.2.2 Methods.....	35
3.2.3 Instruments.....	36
3.3 Results and Discussion	36

CHAPTER 4: TWO-STEP ASSEMBLY OF H- AND J-AGGREGATE COATINGS ON LITHOCHOLIC ACID BASED NANOTUBES.....	54
4.1 Introduction.....	54
4.2 Experimental	55
4.2.1 Materials	55
4.2.2 Formation of J-aggregate Tube.....	56
4.2.3 Characterization	56
4.2.4 Fabrication of Interdigitated Gold Electrodes.....	57
4.3 Results and Discussion	58
4.4 Conclusion	67
CHAPTER 5: TEMPLATED H-/J-AGGREGATE NANOTUBES FOR THE DETECTION OF DOPAMINE	69
5.1 Introduction.....	69
5.2 Experimental	70
5.2.1 Materials	70
5.2.2 Formation of Templated H-/J-aggregate Nanotubes.....	71
5.2.3 Characterization	71
5.2.4 Fabrication of H-/J-aggregate Nanotube-Based Sensor Platform.....	72
5.3 Results and Discussion	73

5.4 Conclusion	81
CHAPTER 6: CONCLUSION	83
REFERENCES	87

LIST OF FIGURES

Figure 1 Schematic of the process that converts cholesterol into primary and secondary bile acids within the human liver. Cholesterol is first converted into 7 α -hydroxycholesterol which is subsequently converted into 7 α -hydroxy-4-cholesten-3-one. At this point both CA and CDCA are produced. Then, in the large intestine, both CA and CDCA are broken down again into DCA and LCA respectively.	2
Figure 2 a) 2D and b) 3D chemical structure of lithocholic acid; a typical secondary bile acid. ...	3
Figure 3 Schematic representation of expected micelle structures for different values of the critical packing parameter.....	5
Figure 4 Schematic representation of the three-possible chiral self-assembly pathways. (a) Width of the helical ribbon stays constant as the pitch of the ribbon decreases and the ribbon fuses together to form a hollow tube. (b) Pitch of the ribbon stays constant as the width of the ribbon increases, eventually fusing together and forming a tube. The last possible option is for the temperature to be above the gel-to-liquid temperature and the ribbon will revert back to a spherical micelle [17,18].....	7
Figure 5 Schematic representation of the exciton energy path in the photosynthetic complex of the green sulfur bacteria.....	9
Figure 6 A schematic representation of H- and J-aggregate structure and the corresponding blue/red shift associated with each structure. H-aggregate is characterized by a blue shift and involves monomer molecules stacking on top of each other. J-aggregate is characterized by a red shift and involves the monomer molecules stacking in a brick layer fashion.	10

Figure 7 Schematic illustration of the fabrication of interdigitated gold electrodes.....	17
Figure 8 Chemical structure of 3,3'-diethylthiacarbocyanine iodide (DiSC ₂ (3)) and (b) lithocholic acid. (c) Adsorption spectra of LCA/DiSC ₂ (3) solution with the mixed ratio of 2:1 and 5:1 after 24-hour incubation at room temperature, together with the adsorption spectrum of 0.5 mM DiSC ₂ (3) in 1% w/w ammonia solution. (d) Optical microscopy, (e) polarizing optical microscopy, and (f) SEM images of spherulitic J-aggregates formed in LCA/DiSC ₂ (3) solution with the mixed ratio of 2:1 after 24-hour incubation. The concentration of LCA is 1 mM.	18
Figure 9 Adsorption spectrum of LCA/DiSC ₂ (3) solution with the mixed molar ratio of 1:1 after 24-hour incubation at room temperature, together with the adsorption spectrum of 0.5 mM DiSC ₂ (3) in 1% w/w ammonia solution. The concentration of LCA is 1 mM.	19
Figure 10 (a) Adsorption spectra of CA/ DiSC ₂ (3) and (b) DCA/ DiSC ₂ (3) solution with the mixed molar ratio of 5:1 after 24-hour incubation at room temperature. The concentration of CA is 1 mM and 13 mM, respectively. The concentration of DCA is 1 mM and 9 mM, respectively. The critical micelle concentration is 13 mM for CA and 9 mM for DCA[81].	20
Figure 11(a) Low-resolution optical microscopy and (b) SEM images of spherulitic J-aggregates formed in LCA/ DiSC ₂ (3) solution with the mixed ratio of 2:1 after 24-hour incubation. The concentration of LCA is 1 mM.	21
Figure 12 SEM image of a collapsed spherulitic J-aggregate.....	22
Figure 13 Growth kinetics of J-aggregate spherulites formed in LCA/ DiSC ₂ (3) solution with a mixed ratio of 2:1 and 5:1. The representative optical microscopy images of J-aggregate spherulites formed at the mixed ratio of 2:1 are inset in Figure 2. The concentration of LCA is 1 mM.	24

Figure 14 Optical microscopy images of broken spherulitic J-aggregates by (a) 1 min and (b) 5 min sonication time. (c) AFM image of J-aggregate fibrils from broken spherulitic J-aggregates by 10 min sonication. (d) TEM images of LCA nanotubes and (e) J-aggregate fibrils. The spherulitic J-aggregates were formed in LCA/ DiSC ₂ (3) solution with the mixed ratio of 2:1. The concentration of LCA is 1 mM	25
Figure 15 Adsorption spectra of J-aggregate spherulite solution before and after 10 min sonication.	26
Figure 16 (a) Time-dependent adsorption spectra of LCA/ DiSC ₂ (3) solution with the mixed ratio of 2:1. (b) Intensity of J-band at 590 nm as a function of incubation time. The concentration of LCA is 1 mM. (c) Schematic representation of a LCA micelle with the J-aggregates of DiSC ₂ (3) molecules in its hydrophobic cavity and (d) autocatalytic aggregation of J-aggregate incorporated LCA micelles into J-aggregate fibrils.	27
Figure 17 Absorption spectrum of LCA/ DiSC ₂ (3) solution with the mixed molar ratio of 5:1 after 24-hour incubation at room temperature. The concentration of LCA is 0.5 mM.....	28
Figure 18 a) IV curves of J-aggregate spherulites and b) J-aggregate spherulites bridging the gap of interdigitated Au electrodes with 20 μ m gap.....	29
Figure 19 a) Current as a function of temperature at various voltage levels and b) cycle behavior of J-aggregate spherulites under a bias voltage of 3V at 16°C and 24°C.....	30
Figure 20 a) UV-vis spectra of J-aggregate spherulites at various temperatures and b) percent change in absorption intensity and number of molecules coupled as a function of temperature.	31
Figure 21 Chemical structures of (a) DiSC ₂ (3) and (b) LCA. (c) absorption spectra of LCA/DiSC ₂ (3) solution with the mixed ratio of 5:1 after 24 hour incubation at room temperature	

in 1%, 5%, 10% and 30% w/w ammonia solution. (d) Optical microscopy image of J-aggregate spherulites. (e) and (f) are optical microscopy and SEM images of H-aggregate fibers	38
Figure 22 SEM image of random aggregates of 0.2 mM DiSC ₂ (3) in 1% ammonia solution.	39
Figure 23 Absorption spectra of H-aggregate fibers from the co-assembly of LCA and DiSC ₂ (3) with the molar ratio of (a) 2:1 and (b) 5:1 in 30% ammonia solution before and after 19.5 hours of evaporation at room temperature.	40
Figure 24 (a) Time-dependent absorption spectra of LCA/DiSC ₂ (3) solution with the mixed ratio of 1:1 as the evaporation of ammonia solution takes place at room temperature. (b) Intensity of J-band at 590 nm and H-band at 426 nm as a function of evaporation time. Optical microscopy of H-/J-aggregate hybrid rods (c) before and (d) after 19 hours evaporation time. (e) SEM image of J-aggregate fibers from the splitting of H-/J-aggregate hybrid rods.....	41
Figure 25 a) H-aggregate solution formed at a 1:1 molar ratio before evaporation takes place and b) J-aggregate solution formed at a 1:1 molar ratio via the evaporation of ammonia after 24-hours evaporation time.....	42
Figure 26 (a) Absorption and emission spectra of J-aggregate fibers formed from the co-assembly of LCA and DiSC ₂ (3) with the molar ratio of 1:1 in 30% ammonia solution. (b) Fluorescent microscope image of J-aggregate fibers.....	43
Figure 27 (a – c) Polarized optical microscopy images of H-/J-aggregate hybrid rods during the drying of a drop of rod solution on a glass substrate. (d) AFM image of H-/J-aggregate rods dried on glass substrate. (e) Schematic representation of H- to J-aggregate transition during the splitting of H-/J-aggregate rods	44

Figure 28 Absorption spectra of H-/J-aggregate rods formed from the co-assembly of LCA and DiSC ₂ (3) with the molar ratio of 1:1 in 30% ammonia solution as a function of time. The rod solution was sealed in a glass bottle.	45
Figure 29 (a) Absorption spectra of J-aggregate fiber solution before (black) and after the addition of 1 mL 30% ammonia solution (blue) and 500 mM NaCl (red). (b) Optical microscopy images of dispersed J-aggregate fibers (c) H-/J-aggregate hybrid rods after the addition of 1 mL 30% ammonia solution and (d) loosely packed J-aggregate fiber bundles after the addition of 500 mM NaCl	47
Figure 30 (a) AFM image of H-aggregate fibers bridging the 20 μ m gap between interdigitated Au electrodes. (b) Temperature-dependent I-V curves of H-aggregate fibers and (c) J-aggregate fibers. (d) Resistance of H- and J-aggregate fibers as a function of temperature and (e) temperature-dependent absorption spectra of J- and H-aggregate fibers in solution.....	48
Figure 31 a) CV curves of H-aggregates formed at a 5:1 mix ratio (black) and J-aggregates formed via evaporation of ammonia from 1:1 mix ratio sample (red) done in 1 M KCl solution and b) Energy level diagram of the HOMO/LUMO levels of the H- and J-aggregates compared to the Fermi level of Au. The red line denotes the LUMO level of J-aggregates, blue line the LUMO level of H-aggregates and the gold line is the Fermi level of Au.	50
Figure 32 Number of coherently coupled molecules in the J-aggregate fibers as a function of temperature	52
Figure 33 a) TEM and b) SEM of tubes formed in 1% ammonia.....	58
Figure 34 Dye structures of a) D25 and b) D35. UV-vis of aggregates formed by c) D25 coating and d) D35 coating of LCA tubes in 1% ammonia.....	59

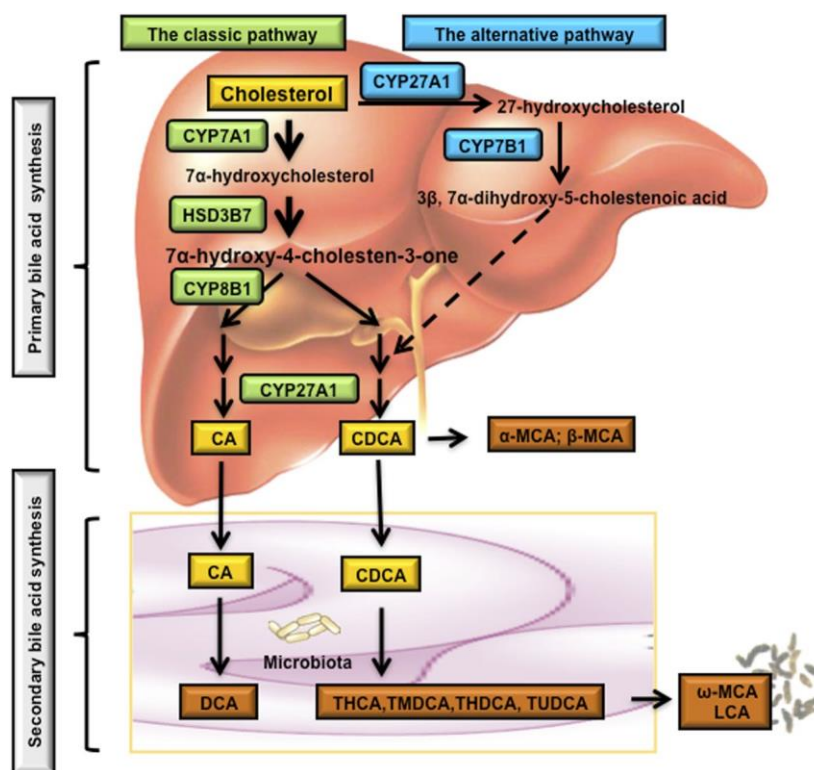
Figure 35 TEM showing patches of dye coating on the surface of LCA tubes during the coating process.....	60
Figure 36 a) Time-dependent UV-vis absorption spectra of the D25 coated LCA tubes showing the transition of the H-aggregate coating into the J-aggregate coating and b) a plot of UV-vis absorption intensity as a function of time showing the gradual decrease of the H-band and increase of the J-band.....	62
Figure 37 a) IV curve of fresh D25 coated LCA nanotubes, b) IV curve of D25 coated LCA nanotubes that were aged for 3 days, c) IV curve of D35 coated LCA tubes showing the behavior of a pure J-aggregate and d) SEM image of the dye coated LCA nanotubes bridging the interdigitated Au electrodes.	64
Figure 38 Cyclic curves of a) D25 H-aggregate coated tubes and b) D35 J-aggregate coated tubes. Schematic energy level diagram (c) of the HOMO/LUMO levels of H-aggregate and J-aggregate coatings with respect to the fermi level of Au electrodes.	65
Figure 39 a) IV curves at different temperatures for the D25 coating and b) IV curves at different temperatures for the D35 coating.....	66
Figure 40 UV-vis absorption spectra at different temperatures for LCA tubes coated with a) D25 and b) D35.....	67
Figure 41 (a) Chemical structure of lithocholic acid and (b) 3,3'-diethylthiadicarbocyanine iodide.....	72
Figure 42(a) AFM of LCA nanotubes dried on glass substrates and (b) TEM images of LCA nanotubes dried on a carbon coated copper grid.....	73

Figure 43 (a) AFM image of templated H-/J-aggregate nanotubes dried on a glass substrate. (b) Absorption spectra of templated H-/J-aggregate nanotubes and D25 monomer in NH_4OH solution.....	75
Figure 44 (a) Schematic of J-aggregate nanotube-based sensor platform. (b) Optical microscopy and (c) SEM images of interdigitated Au electrodes with deposited J-aggregate nanotube networks.....	76
Figure 45 I-V curves of H-/J-aggregate nanotube-based sensors with (circle) and without (square) visible light irradiation.....	77
Figure 46 Schematic illustration of the oxidization of DA induced by pH values.	78
Figure 47 Current change of H-/J-aggregate nanotube-based sensor platform in response to 20 nM DA in buffer solution at pH 10 with and without 30s visible light irradiation. Schematic of photoinduced electron transfer (PET) from the templated H-/J-aggregate nanotube to the adsorbed DA is insert in figure.	79
Figure 48 Cyclic voltammogram of H-/J-aggregate nanotubes immobilized on ITO in aqueous solution containing 1M KCL. Scan rate: 0.1 v/s.....	80
Figure 49(a) Current changes of H-/J-aggregate nanotube-based sensor platform as a function of DA concentrations in buffer solution at pH 10 with 30s visible light irradiation. (b) Current changes of H-/J-aggregate nanotube-based sensor platform in response to 10 nM DA and 10 μM UA in buffer solution at pH 10 with 30s visible light irradiation.	81

CHAPTER 1: INTRODUCTION

1.1 Bile Acids

Bile acids are important physiological molecules within the human body and researchers have been trying to determine the full extent of the role they play since their first discovery. It was originally believed the bile acids only served the role of helping maintain cholesterol homeostasis[1]. The breakdown of cholesterol is the primary formation mechanism of bile acids within the body. This occurs within the hepatocyte as a byproduct of cholesterol breakdown and bile acids formed in this fashion are termed ‘primary’ bile acids. Bile acids can also form via the removal of a hydroxy group by bacteria inside the colon and these are termed ‘secondary’ bile acids[2]. The formation of bile acids via the breakdown of cholesterol is a highly catabolic process that ends up eliminating half of the total amount of cholesterol in the body[1, 3, 4]. The process begins with the breakdown of cholesterol into 7α -hydroxycholesterol which is further broken down into the bile acids cholic acid (CA) and chenodeoxycholic acid (CDCA), an illustration of this can be seen in Figure 1. The secondary bile acid, lithocholic acid (LCA), which is part of the primary focus of this dissertation, is formed by the further breakdown of CDCA. While in the large intestine, the bacteria 7α -hydroxylase removes a hydroxyl group from CDCA that ultimately produces LCA. The majority of LCA produced is then secreted into bile, while a small amount is circulated back into the liver[5]. The structure of LCA can be seen in Figure 2a and Figure 2b.



Reproduced with permission from T. Li and J. Y. L. Chiang, "Bile Acid Signaling in Metabolic Disease and Drug Therapy," *Pharmacological Reviews*, vol. 66, no. 4, pp. 948-983, 2014. Copyright 2014 The American Society for Pharmacology and Experimental Therapeutics [5].

Figure 1 Schematic of the process that converts cholesterol into primary and secondary bile acids within the human liver. Cholesterol is first converted into 7 α -hydroxycholesterol which is subsequently converted into 7 α -hydroxy-4-cholesten-3-one. At this point both CA and CDCA are produced. Then, in the large intestine, both CA and CDCA are broken down again into DCA and LCA respectively.

For the longest time bile acids were only considered as detergent molecules that only served important roles in the digestive process such as cholesterol solubilization. They recently have been discovered to be even more physiologically important. Bile acids can also act as hormones that activate signaling pathways in cells and nuclear receptors in the liver and gastrointestinal tract[6].

Even with all this research into the role of bile acids in the human body, all the answers are not currently known. High concentrations of secondary bile acids within different portions of the

body have been correlated to increased incidence of certain diseases, including colon cancer[6, 7]. It is currently believed that by controlling the formation of secondary bile acids within the colon one can alter the toxicity and pathophysiology of bile acids to cells in the liver and gastrointestinal tract[6]. However, it is not due to the physiological importance of bile acids that there is an interest in them from a materials science aspect. Their planar structure differs from most other types of amphiphilic molecules and this allows them to exhibit interesting self-assembly abilities that prove useful in the formation of different nanostructures from nanotubes to spherulites, as will be examined in later chapters.

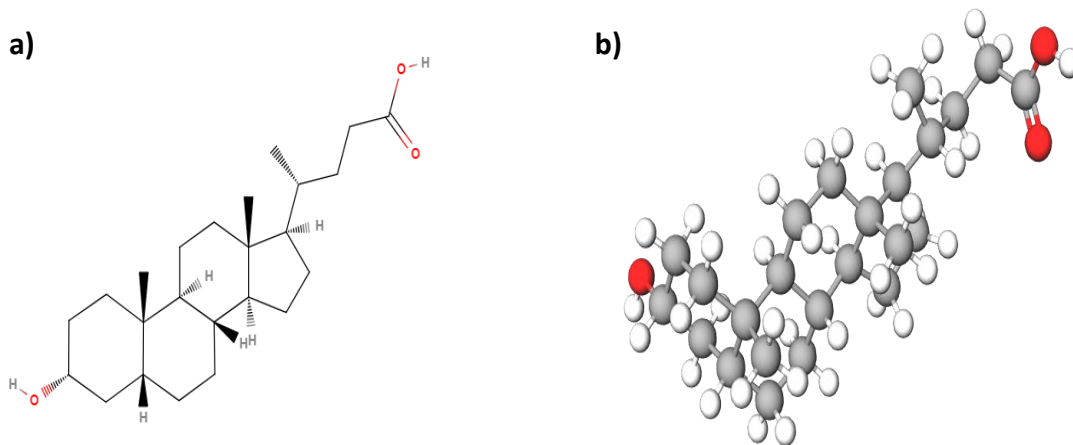


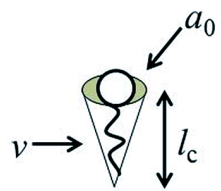
Figure 2 a) 2D and b) 3D chemical structure of lithocholic acid; a typical secondary bile acid.

1.2 Self-Assembly of Amphiphilic Molecules

Depending on the surrounding environment, certain molecules are able to organize themselves via non-covalent interactions (i.e. van Der Waals, electrostatic, hydrophobic) into organized supramolecular structures without the need of outside intervention. This process is known as self-assembly and it can occur in a static environment or a dynamic environment. In the former case, no external energy needs to be added to the system in order for the self-assembly to take place. In

the case of dynamic self-assembly, there needs to be some external energy sources providing additional energy to the system[8]. Often, molecules that can undergo a self-assembly process are amphiphilic in nature. For a molecule to be an amphiphile it needs to contain both hydrophilic and hydrophobic moieties. Nature is full of amphiphilic molecules, and an example would be carbohydrate amphiphiles. These biological amphiphiles are an important stability and functional contributor of cell membranes[9, 10]. These molecules are able to precisely self-assemble into supramolecular structures that range from simple micelles and vesicles to monolayers and tubules in solution or at an interface. The primary driving force in the self-assembly process is the desire for the hydrophobic or non-polar portion of the molecule to extricate itself from contact with water. The type of structure that is formed can depend on many factors including the size and geometry of the hydrophobic and hydrophilic portion of the molecule and the composition of the solvent environment.

Surfactants (surface active agents) are one of the most highly studied groups of amphiphilic molecules. They typically consist of a long tail that is built primarily of hydrocarbons and a head group that can be ionic or non-ionic in nature. Due to being composed of hydrocarbons, the tails of surfactants are hydrophobic. They tend to aggregate at the air-water interface where the tails can stick out through the surface into air and the head group remains in the aqueous solution. When the concentration of surfactants is high enough, micelle formation in aqueous solution will take place. This will allow the hydrophobic tails to shield themselves from the aqueous environment while allowing the head group to contact with the aqueous environment. The concentration at which this occurs is called the critical micelle concentration (CMC) and for commonly used surfactants the CMC is usually less than 0.01M [11].



$$CPP = v/a_0 l_c$$

Critical Packing Parameter ($v/a_0 l_c$)	Critical Packing Shape	Structures Formed
$< 1/3$	Cone	Spherical micelles
$1/3 - 1/2$	Truncated cone	Cylindrical micelles
$1/2 - 1$	Truncated cone	Flexible bilayers, vesicles
~ 1	Cylinder	Planar bilayers
> 1	Inverted truncated cone or wedge	Inverted micelles

Reproduced with permission from M. Salim, H. Minamikawa, A. Sugimura, and R. Hashim, "Apmphiphilic designer nanocarriers for controlled release: from drug delivery to diagnostics," *MedChemComm*, vol. 5, no. 11, pp. 1602-1618, 2014. Copyright 2014 Royal Society of Chemistry [12].

Figure 3 Schematic representation of expected micelle structures for different values of the critical packing parameter.

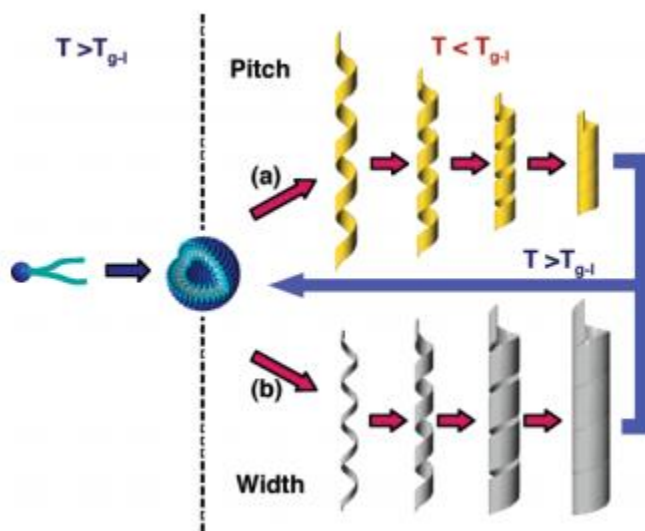
The type of structures that are formed during micelle formation is strongly dependent on the geometry of the amphiphile being used. Because surfactants are composed of a head group and long hydrophobic chain, they are typically the easiest to use when predicting micelle shape. Micelle formation is dependent upon the critical packing factor of the surfactant which is defined as $C_{pp} = V_0/A_{mic}l_c$; where V_0 is the effective volume of the hydrocarbon tail, A_{mic} is the head

group surface area at the aggregate-solution interface, and l_c is the chain length of the hydrocarbon tail. The value of this factor will determine whether the formed micelle is spherical, cylindrical or lamellar in nature [11, 13]. Schematic representations and value ranges for each case can be seen in Figure 3[12].

Aside from surfactants, there is another particularly interesting class of amphiphilic molecules that undergoes a micelle formation process, and that is bile salts. Bile salts are not typical amphiphilic molecules, as discussed briefly in Section 1.1. Instead of the head to tail configuration of their hydrophilic and hydrophobic groups, bile salts are arranged in a nearly planar fashion with hydrophilic and hydrophobic sides. This unusual amphiphilic geometry arises from the fact that the hydrophilic -OH groups and the hydrophobic -CH₃ groups are arranged on opposite sides of the tetracyclic ring system. Because of their geometry, bile salts also tend to have a much lower CMC than other amphiphiles [14]. The first mechanism devised to explain the aggregation behavior of bile salts was developed by Small [15]. He developed a primary-secondary micelle model in which, at first, micelle formation takes place in the usual way. The bile salts come together and turn their hydrophobic faces in towards each other which results in the expulsion of water from the micelle core. Once the concentration becomes high enough, hydrogen bonding between the hydrophilic faces of the bile salts can occur, allowing for the elongation of the primary micelle into a host of different structures[15].

Another possible mechanism is known as a chiral self-assembly and it involves the formation of an intermediate helical ribbon that is able to then collapse into a hollow tube [16]. Once the helical ribbon is formed there are three possible pathways forward, a schematic of these pathways may be seen in Figure 4 [17, 18]. First the molecules assemble into spherical micelles that then aggregate to form the helical ribbons. As long as the temperature stays below the gel-to-liquid

transition temperature, one of two different routes will occur. Either the pitch of the ribbon will shorten while maintaining a constant width and collapsing into a tube or the width will increase while maintaining a constant pitch and the ribbon will expand into a tube. If the temperature is raised above the gel-to-liquid transition temperature the structure will revert back to the spherical micelle formation. There are a number of different molecules that have been shown to undergo chiral self-assembly. These include carbohydrate amphiphiles [19-21], amino-acid based amphiphiles [18, 22-24], nucleotide-based amphiphiles [25, 26] and bile acids [17, 27-29]. LCA is one of the bile acids that can undergo a variety of self-assembly mechanisms, including chiral self-assembly.



Reproduced with permission from T. Shimizu, M. Masuda, and H. Minamikawa, "Supramolecular nanotube architectures based on amphiphilic molecules," *Chemical Reviews*, vol. 105, no. 4, pp. 1401-1444, 2005. Copyright 2005 American Chemical Society [16].

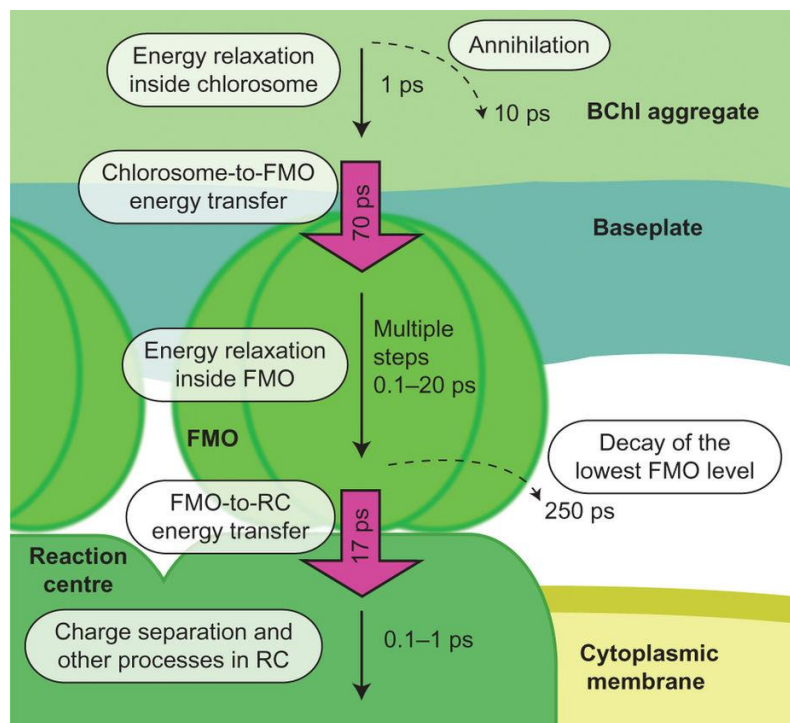
Figure 4 Schematic representation of the three-possible chiral self-assembly pathways. (a) Width of the helical ribbon stays constant as the pitch of the ribbon decreases and the ribbon fuses together to form a hollow tube. (b) Pitch of the ribbon stays constant as the width of the ribbon increases, eventually fusing together and forming a tube. The last possible option is for the temperature to be above the gel-to-liquid temperature and the ribbon will revert back to a spherical micelle [17,18]

Previous studies have shown that LCA can form small vesicles that linearly aggregate into hollow tubes over time in alkaline solution without the intermediate helical ribbon stage [29]. That same study found that LCA tubes could withstand changes in pH from 12.3 down to 7.4 all while reversibly changing their morphology from helical to straight. It is because of its many self-assembly mechanisms and various morphologies that LCA is an attractive option to be used in research involving the formation of molecular dye aggregates, as will be seen in later chapters.

1.3 Light Harvesting Systems and H-/J-Aggregates of Cyanine Dyes

Nature has proven to be the designer of some of the most efficient structures and processes, and it is for this reason that humans have striven to mimic these natural structures and processes for centuries. One of the best examples of a highly efficient natural process is that of photosynthesis. It is a constant goal of researchers to attain high efficiency, artificial photosynthetic systems and promising advance have been made[30-33]. Within nature the largest and most efficient light-harvesting devices in the natural world are chlorosomes. They form the light-harvesting antenna of the green sulfur bacteria which allows the bacteria to harvest light in incredibly low light intensities[34]. Chlorosomes do this by forming energy gradients, made up of closely-packed molecular aggregates, between different light harvesting complexes that allow absorbed light energy to be funneled downhill to its eventual destination, the reaction complex[35, 36]. This downhill funneling is what allows the natural light harvesting systems to become large on a microbial scale and maintain their high efficiency. It has been found that while trying to mimic these natural systems that without the energy gradient found in nature, the energy gets lost in the system before reaching its final destination[35]. A schematic representation of the energy gradient

within the photosynthetic complex of the green sulfur bacteria can be seen in Figure 5[37]. Here we see that after light absorption in the bacteriochlorophyll (BChl) aggregate the exciton relaxes down into the Fenna-Matthews-Olson (FMO) protein complex. From here the energy is transferred into the reaction center of the green sulfur bacteria.

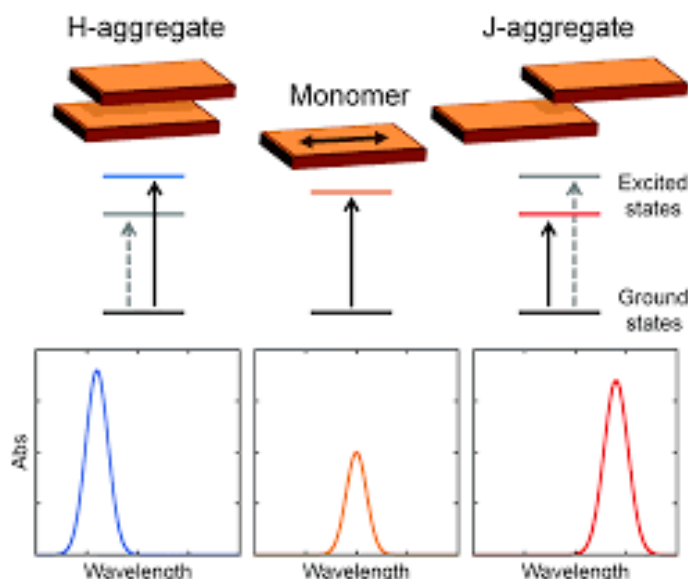


Reproduced with permission from J. Dostál, J. Pšenčík, and D. Zigmantas, “In situ mapping of the energy flow through the entire photosynthetic apparatus,” *Nature Chemistry*, Article vol. 8, p. 705, 05/30/online 2016. Copyright 2016 Springer Nature [37].

Figure 5 Schematic representation of the exciton energy path in the photosynthetic complex of the green sulfur bacteria.

The first step towards this goal was the discovery, by Jelley and Scheibe, of the organized supramolecular structure of dye molecules, specifically of pseudoisocyanine chloride[38-41]. They found that at high enough concentrations, the adsorption band of pseudo isocyanine, which was typically broad and centered around 525 nm, would become sharp and shift to 570 nm. This aggregation of dye molecules would come to be termed J-aggregates. J-aggregates exhibit a narrow

and intense absorption band (J-band), red-shifted with respect to the monomer, that is due to the electronic coupling of molecular dipoles[39, 42]. J-aggregates form a bricklike structure that allows for high exciton transfer rates that are facilitated by the strong exciton delocalization within the J-aggregate structure[43]. A schematic representation[44] of this structure can be seen in Figure 6.



Reproduced with permission from G. Pesitelli, L. Di Bari, N. Berova, “Application of electronic circular dichroism in the study of supramolecular systems,” *Chemical Society Reviews*, vol. 43, no. 15, pp. 5211-5233, 2014. Copyright 2014 Royal Society of Chemistry [44].

Figure 6 A schematic representation of H- and J-aggregate structure and the corresponding blue/red shift associated with each structure. H-aggregate is characterized by a blue shift and involves monomer molecules stacking on top of each other. J-aggregate is characterized by a red shift and involves the monomer molecules stacking in a brick layer fashion.

Around the same time as their discovery, the model that could be used to describe the optical properties of J-aggregates had already been developed. This model is termed the Frenkel exciton model and was developed in the 1931 by Frenkel[45]. In a system of N identical molecules, when one molecule is brought into its excited state, it forms an N -fold degenerate excited state, barring any intermolecular interactions. Due to the coupling of the optical transition dipoles

between different molecules, this N -fold degeneracy results in the formation of new excited states that are shared coherently by the molecules[46]. Using the Frenkel exciton model, many of the optical properties of J-aggregates can be understood[47]. For example, the red-shift in the absorption band was described mathematically by Knoester. He described the eigenstates of linear J-aggregates as Bloch states, where the eigen states are given by Equation 1 [48]:

$$|k\rangle = \frac{1}{N} e^{2\pi i k n / N} |n\rangle \quad (1)$$

with the energy eigenstates given by:

$$E_k = \epsilon_0 - 2J \sum_{n=1}^{(N-1)/2} \frac{1}{n^3} \cos \frac{2\pi k n}{N} \quad (2)$$

where k denotes the quantum number and takes the values $k = 0, \pm 1, \pm 2, \pm((N-1)/2)^2$. Here then the molecular oscillator strengths of the exciton states are given by:

$$|M_k|^2 = N\mu^2 \delta_{k,0} \quad (3)$$

And this is the most important result of Knoester’s mathematical run-through. In this result, we see that the $k=0$ state collects all the molecular oscillator strength, and all of the other states remain “dark”. This is due to the fact that all the molecular dipoles oscillate in phase in the $k=0$ state. The result of this is that within the exciton band, all of the energy is bound up in the lowest energy state, leading to a superradiant, red-shifted absorption band[48]. The opposite of this is true for molecular aggregates that are stacked in a parallel fashion, termed H-aggregates. In that case, all the molecular oscillator strength is bound up in the topmost energy state within the exciton band. This leads to a blue-shifted absorption band compared to the monomer absorption.

The previous result by Knoester is for the case when you have linear aggregations, which were common for dyes known to form J-aggregate. However, as is the case in nature with the green

sulfur bacteria, cylindrical molecular aggregates can form and therefore require a different mathematical treatment to describe their more complex optical properties. The primary difference between linear and cylindrical molecular aggregates is that often there is more than one state that exhibits a superradiant emission. The Bloch eigenstates and energy equations are significantly more complex and the oscillator strength is given by the following equation:

$$|M_k|^2 = N_1 N_2 \mu^2 \left[\cos^2 \beta \delta_{k,0} + \frac{1}{2} \sin^2 \beta (\delta_{k,h} + \delta_{k,-h}) \right] \quad (4)$$

with $\mathbf{h} = (\gamma N_1 / 2\pi, 1)$, which is the helical wave vector[48, 49]. As can be seen in the equation above, there will be three superradiant states in a cylindrical or helical system. The first superradiant state will arise from the case where $k = 0$, which is polarized along the long axis of the cylinder. The $k = \pm h$ states are perpendicular to the long axis of the cylinder and are degenerate which implies that they together create one superradiant state. Therefore, it stands that a cylindrical or helical molecular aggregate will have two superradiant states that appear within the absorption spectrum when one accounts for the fact that the second state is degenerate.

The applications of the J-type structure are far-reaching, from biomolecular science to organic solid-state science to nonlinear optics and quantum computing. J-aggregates of amphiphilic cyanine dyes have been shown to promote the growth of silver nanowires by behaving as structure-directing agents with the ability to reduce silver ions to silver nanoparticles[50]. J-aggregates have also been used in the development of solid-state integrated devices that operate in the strong coupling limit of cavity quantum electrodynamics, due to exhibiting a collective narrow linewidth high oscillator strength optical transition that arises from their molecular arrangement and strong dipole coupling[51]. Cyanine dyes in general are an important near-infrared dye that have been in use since the mid-1800's for applications ranging from photography to industrial

paints and from biological probes to laser materials[52]. Cyanine dyes are able to self-assemble into J-aggregate films in certain situations but in order to fully utilize their electron transport properties it is important for them to be arranged in a tubular fashion, similar to the green sulfur bacteria's light harvesting antenna. The dyes used in our experiments consist of two nitrogen-containing heterocyclic rings that are joined by a polymethine bridge. The LCA molecule can be deprotonated in alkaline solution, leading to the formation of a COO^- group that allows the cyanine dye to electrostatically interact with the LCA. In this work, we synthesize J- and H-aggregates in two different fashions. First, we utilize a co-assembly process between LCA and cyanine dyes in ammonia solution and analyze how varying the molar ratio of LCA and cyanine dyes can change the morphology of the J- and H-aggregates formed via the co-assembly process. We also analyze the kinetics of the formation process and the size of the final product at the different molar ratios of LCA and cyanine dyes. We then analyze how altering the ammonia concentration of the solvent can change the type of molecular aggregates. Next, we utilize a two-step assembly process to form J- and H-aggregate of cyanine dyes on an LCA tube template at different ammonia concentrations. We also characterize the H- and J-aggregate coated LCA tubes optically and electronically. Finally, we look at potential applications of the H- and J-aggregate coated tubes by attempting to detect dopamine in buffer solution.

CHAPTER 2: FORMATION OF SPHERULITIC J-AGGREGATES FROM THE CO-ASSEMBLY OF LITHOCHOLIC ACID AND CYANINE DYE

Portions of this chapter were originally published in Rhodes, S.; Liang, W.; Shteinberg, E.; Fang, J.; Formation of Spherulitic J-aggregates from the Co-assembly of Lithocholic Acid and Cyanine Dye. *J. Phys. Chem. Lett.*, **2017**, 8(18), 4504-4509.

2.1 Introduction

Supramolecular aggregates of organic dyes through non-covalent interactions have attracted great interest in chemistry and materials science because they exhibit collective optical and excitonic properties[53, 54]. Cyanine dyes with two aromatic nitrogen-containing heterocycles linked by a polymethine chain are an important class of cationic dyes, which are widely used in color photography, nonlinear optics, and photoelectric devices[52]. The polarizability and hydrophobicity of cyanine dyes are the main driving forces for the formation of supramolecular aggregates. Depending on the spatial stacking of dye molecules, two types of supramolecular aggregates can be formed[38, 39]. J-aggregates represent an edge-to-edge stacking of dye molecules, showing a red-shifted absorption band with respect to the monomer band and a strong fluorescence emission. On the contrary, H-aggregates represent a face-to-face stacking of dye molecules, showing a blue-shifted absorption band compared with the monomer band and a strong emission quenching. The collective optical and excitonic properties of J- and H-aggregates can be explained by the Frenkel exciton theory[45]. Despite the importance of J-and H-aggregates of cyanine dyes in diverse optoelectronic applications, the control of their morphologies remains a challenge.

Recently, efforts have been made in the use of the self-assembly of amphiphilic cyanine dyes to form tubular J-aggregates[55-63]. The co-assembly of amphiphilic cyanine dyes with surfactants has been used to alter the size and morphology of tubular J-aggregates and consequently their optical properties[64-66]. Bile acids are an amphipathic biological surfactant with a rigid steroid skeleton[67]. The concave side of the steroid skeleton of bile acids is hydrophilic, while the convex side is hydrophobic. The structure of bile acids is different from that of conventional surfactants, which often have a long hydrophobic tail and a hydrophilic polar headgroup. The amphipathic nature of bile acids is manifested in their unusual self-assembly ability. For example, lithocholic acid (LCA) in alkaline solution is able to self-assemble into well-ordered supramolecular aggregates including micelles, ribbons, and tubes, depending on the condition under which the self-assembly occurs[29, 68-73]. The co-assembly of bile acids and other molecules has been proven to be an effective way to form complex supramolecular aggregates[74-78]. Herein, we report the formation of spherulitic J-aggregates from the co-assembly of LCA with 3,3'-diethylthiacarbocyanine iodide ($\text{DiSC}_2(3)$) in ammonia solution. The structure and optical properties of spherulitic J-aggregates are studied at different mixed molar ratios of LCA and $\text{DiSC}_2(3)$. We show that each spherulite contains a core, which serves as a nucleus for the growth of radially oriented J-aggregate fibrils. The growth kinetics of spherulitic J-aggregates are studied with absorption spectroscopy and optical microscopy.

2.2 Experimental Methods

Bile acids used in our experiments were CA, DCA, and LCA purchased from Sigma-Aldrich. $\text{DiSC}_2(3)$ was from Molecular Probes. All chemicals were used without further purification. Ammonia solution was from Sigma-Aldrich. Water used in the experiments was

purified with an Easypure II system (18 M Ω cm, pH 5.7. Holey Formvar filmed grids were from SPI.

The co-assembly of LCA and DiSC₂(3) at different molar ratios was carried out in 1% w/w ammonia solution, in which the concentration of LCA was always kept at 1 mM. The mixture was sonicated in an ultrasonic bath (Branson 1510, Branson Ultrasonics) at ~60°C for 5 min and then allowed to cool to room temperature. The structure and morphology of supramolecular aggregates from the co-assembly were characterized with an optical microscope (Olympus BX), an SEM (Hitachi S3500N), a TEM (FEW Technai F30), and an AFM (Dimension 3100 Veeco Instruments). The optical property of supramolecular aggregates was characterized with a Cary 300 UV-Vis spectrophotometer. For SEM and TEM measurements, aggregate solution was dried on a holey Formvar filmed grid at room temperature for 24 hours and then imaged at an accelerating voltage of 20 and 100 kV, respectively. AFM images were taken with a silicon nitride cantilever (Nanosensors) with a spring constant of 30 N/m and a resonant frequency of 260 kHz in tapping mode. For optical microscope observations, a drop of aggregate solution was placed on a glass substrate, followed by placing a cover glass slide on the top of the drop. IV curves were obtained using a Keithley 2400 Sourcemeter and the temperature was manipulated using an Instec Heating Stage.

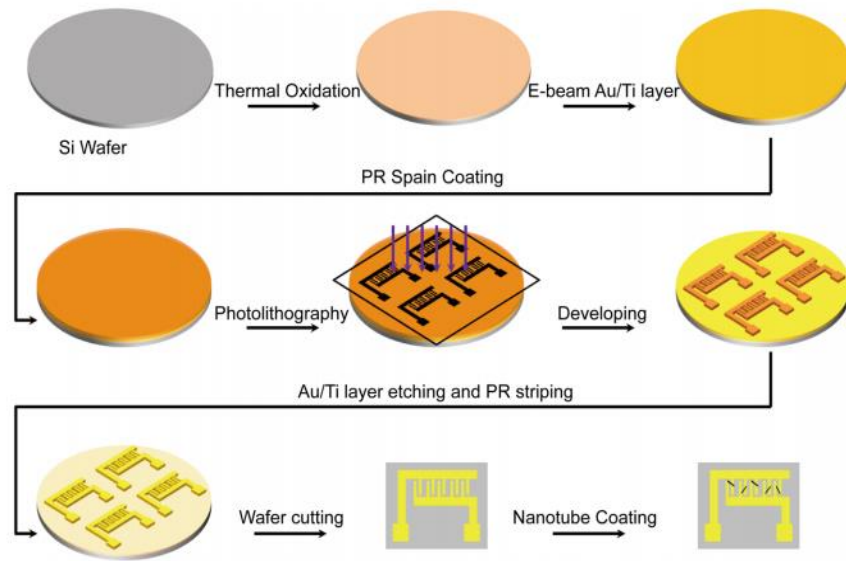


Figure 7 Schematic illustration of the fabrication of interdigitated gold electrodes

For the fabrication of interdigitated gold (Au) electrodes, a 100 nm thick SiO_2 insulation layer was first grown on a 3-inch Si wafer by thermal oxidation process. A metallic seed film which consists of 100 nm Au layer over 10 nm Ti layer was then deposited on the top of the SiO_2 layer by e-beam evaporation. A thin layer of positive photoresist (Microposit S1813, Dow Electronic Materials) was then spin-coated (3000 rpm, 30 sec), soft-baked (105°C , 3 min), exposed under I-line UV aligner (8 seconds) and developed (Microposit MF CID-26 Developer, 35 sec) to obtain photoresist patterns for the interdigitated electrodes with a gap of 20 μm . The developed patterns were hard-baked at 105°C for 10 min and used as a protective layer for subsequent etching steps. The Au/Ti seed layer in exposed areas was chemically etched with an Au etchant (KI and I_2 mixture solution) and a Ti etchant (0.5% HF). The remaining photoresist was dissolved in acetone and the interdigitated Au electrodes were formed after cleaning in methanol and deionized water. The schematic illustration of the fabrication of the interdigitated gold electrodes is shown in Figure 7.

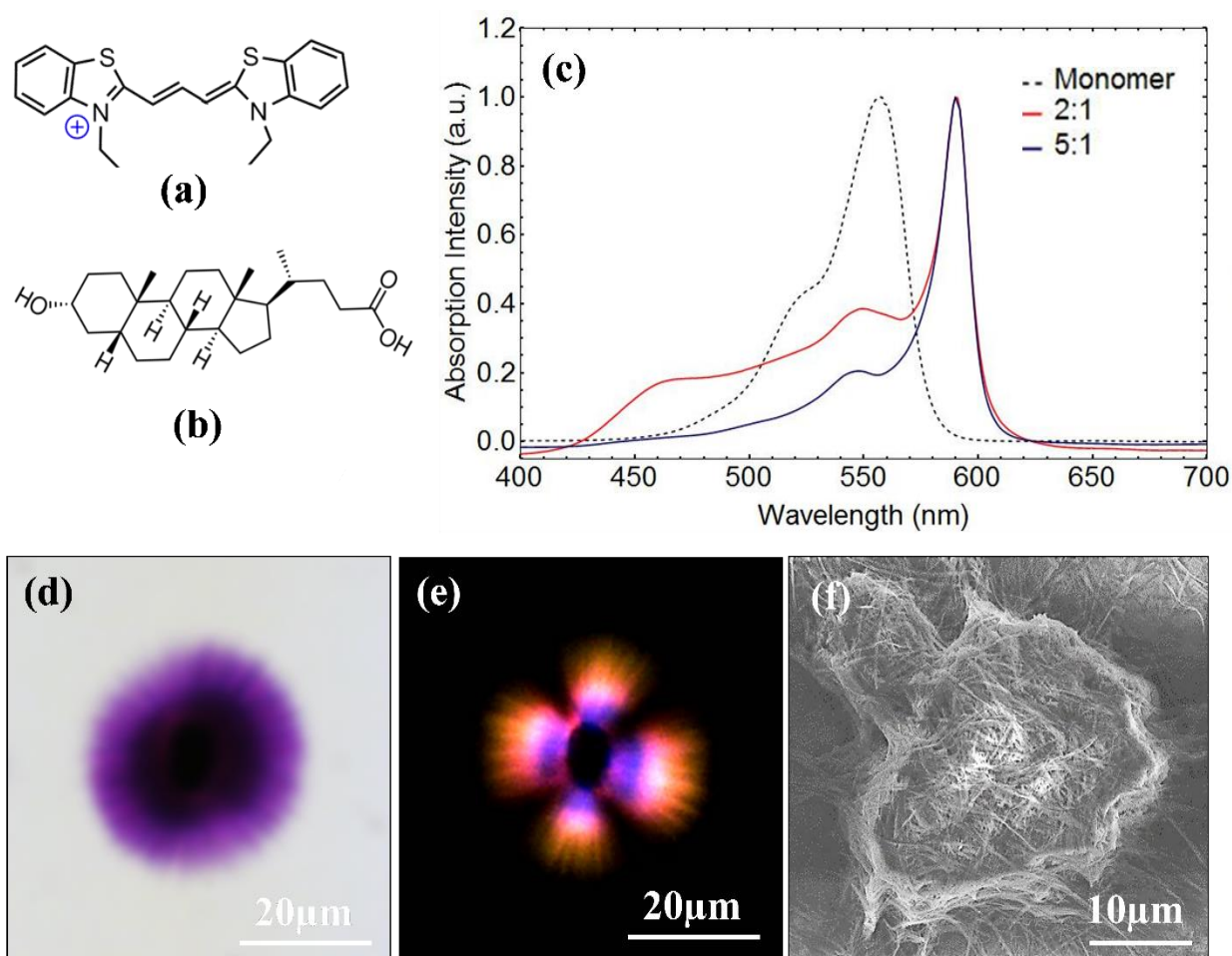


Figure 8 Chemical structure of 3,3'-diethylthiacarbocyanine iodide (DiSC₂(3)) and (b) lithocholic acid. (c) Adsorption spectra of LCA/DiSC₂(3) solution with the mixed ratio of 2:1 and 5:1 after 24-hour incubation at room temperature, together with the adsorption spectrum of 0.5 mM DiSC₂(3) in 1% w/w ammonia solution. (d) Optical microscopy, (e) polarizing optical microscopy, and (f) SEM images of spherulitic J-aggregates formed in LCA/DiSC₂(3) solution with the mixed ratio of 2:1 after 24-hour incubation. The concentration of LCA is 1 mM.

2.3 Results and Discussion

The chemical structure of DiSC₂(3) and LCA used here is shown in Figure 8a,b. We find that LCA is able to induce the J-aggregation of DiSC₂(3) in 1% w/w ammonia solution. As can be seen in the absorption spectra shown in Figure 8c, DiSC₂(3) in 1% w/w ammonia solution shows a strong band at 558 nm, which agrees with the monomer absorption band (556 nm) reported in

the literature[79]. The addition of 1 mM LCA in DiSC₂(3) solution at the mixed molar ratio of 5:1 and 2:1 results in the significant decrease and the slight shift of the monomer band. Interestingly, a new strong band at 590 nm appears, which is red-shifted with respect to the monomer band. The red-shifted band at 590 nm is a result of the J-aggregation of DiSC₂(3) through the interaction with LCA. At the mixed molar ratio of 2:1, a weak H-band at 459 nm is also observed, suggesting that a small fraction of DiSC₂(3) forms H-aggregates. The weak H-band disappears at the mixed molar ratio of 5:1. When the mixed molar ratio is reduced to 1:1, there is still a large fraction of DiSC₂(3) presenting as monomers, which is evident from the strong monomer band seen in Figure 9.

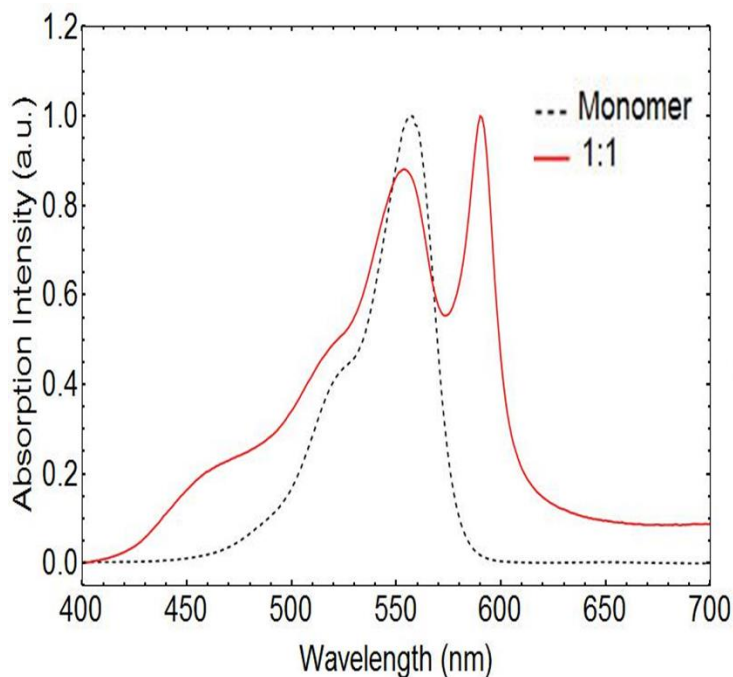


Figure 9 Adsorption spectrum of LCA/DiSC₂(3) solution with the mixed molar ratio of 1:1 after 24-hour incubation at room temperature, together with the adsorption spectrum of 0.5 mM DiSC₂(3) in 1% w/w ammonia solution. The concentration of LCA is 1 mM.

Our results suggest the higher mixed molar ratio of LCA and DiSC₂(3) is required to form J-aggregates. Interestingly, the absorption spectrum of DiSC₂(3) in 1% w/w ammonia solution remains unchanged after the addition of either deoxycholic acid (DCA) or cholic acid (CA) with

the concentration below and above their critical micelle concentrations, which can be seen in the absorption spectra in Figure 10, suggesting that they are unable to induce the J-aggregation of DiSC₂(3). CA, DCA, and LCA in 1% w/w ammonia solution with pH 11.3 are ionized due to the deprotonation of the carboxyl group. These bile acids differ from each other in the number and position of hydroxyl groups on their steroid skeleton. It has been shown that the order of the hydrophobicity is LCA > DCA > CA[80]. Thus we conclude that the hydrophobic interaction of LCA and DiSC₂(3) plays a major role in the formation of J-aggregates.

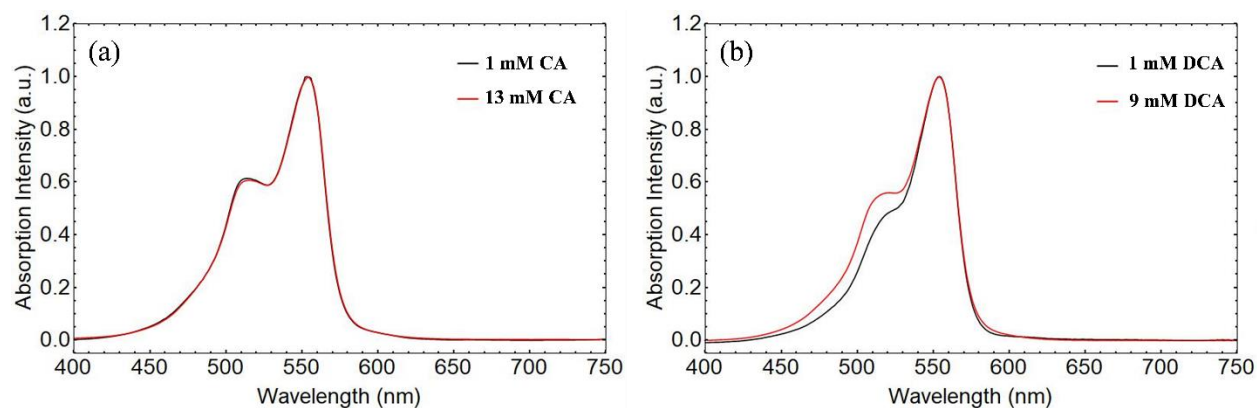


Figure 10 (a) Adsorption spectra of CA/ DiSC₂(3) and (b) DCA/ DiSC₂(3) solution with the mixed molar ratio of 5:1 after 24-hour incubation at room temperature. The concentration of CA is 1 mM and 13 mM, respectively. The concentration of DCA is 1 mM and 9 mM, respectively. The critical micelle concentration is 13 mM for CA and 9 mM for DCA[81].

Optical microscopy images reveal that the J-aggregates from the co-assembly of LCA and DiSC₂(3) have a spherulitic morphology (Figure 8d). Each spherulite contains a core surrounded by radially oriented fibrils with pink color, which is the evidence of the presence of DiSC₂(3) in the fibrils. The absorption spectra shown in Figure 8c suggest that DiSC₂(3) in the fibrils forms J-aggregates. The spherulitic J-aggregates exhibit a characteristic Maltese-cross extinction pattern of light extinction when being viewed under a polarizing optical microscope (Figure 8e). However, the core of the spherulites appears to be nonbirefringent, suggesting that it does not have a long-

range ordered molecular arrangement. The structure of J-aggregate spherulites is further examined with a scanning electron microscope (SEM). Although SEM images show the spherulites collapse after being dried on substrates (Figure 8f), individual J-aggregate fibrils can still be resolved. They either stick out or lay down at the surface of the collapsed spherulites. The diameter of the J-aggregate fibrils is measured in the range from 200 to 300 nm. Low-resolution optical microscopy and SEM images reveal the presence of many spherulitic aggregates in LCA/ DiSC₂(3) solution (Figure 11). Occasionally, we can see the core in the SEM image of collapsed spherulitic aggregates (Figure 12). The surface of the core appears to be featureless.

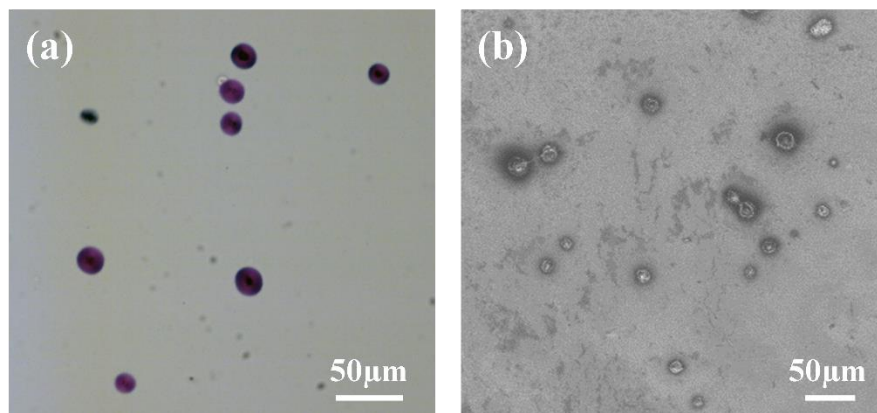


Figure 11(a) Low-resolution optical microscopy and (b) SEM images of spherulitic J-aggregates formed in LCA/ DiSC₂(3) solution with the mixed ratio of 2:1 after 24-hour incubation. The concentration of LCA is 1 mM.

In general, spherulites can be divided into two categories based on nucleation mechanisms[82]. Category I spherulites are a result of heterogenous nucleation, in which fibers grow outward radially from a nucleation site and branch intermittently to maintain a space-filling character. In contrast, Category II spherulites are a result of homogeneous nucleation, in which needles first form in solution and then subsequently split at their tips. Clearly, the spherulitic J-aggregates from the co-assembly of LCA and DiSC₂(3) resemble Category I spherulites. The

representative optical microscopy images inset in Figure 13 shows the growth of J-aggregate fibrils from the core over time. The formation mechanism of spherulitic J-aggregates is similar to that of spherulitic amyloid fibrils[83, 84]. In addition, the representative optical microscopy images also show that the core gradually disassociates by changing its color over a long incubation time.

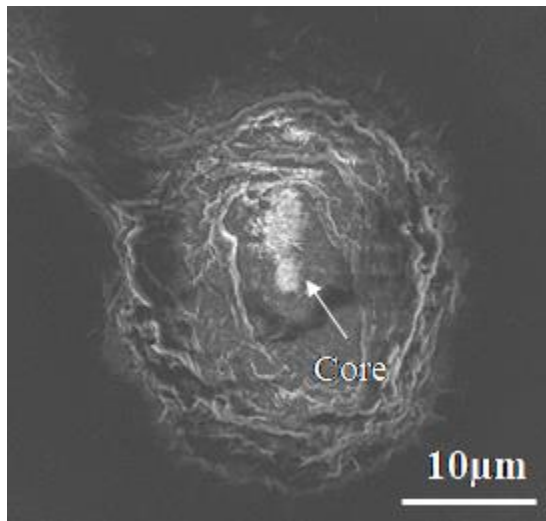


Figure 12 SEM image of a collapsed spherulitic J-aggregate

The radius of J-aggregate spherulites formed in LCA/ DiSC₂(3) solution with the mixed molar ratio of 2:1 increases from ~5.0 to ~34 μm as the incubation time increases from 1 to 48 hours; beyond that it remains almost unchanged (Figure 13). It is also evident in Figure 13 that the radius of spherulitic J-aggregates formed at the mixed molar ratio of 2:1 is slightly larger than that formed at the mixed molar ratio of 5:1 for the same incubation time. We note that spherulitic J-aggregates formed at the mixed molar ratio of 5:1 have a slightly smaller core compared with the spherulitic J-aggregates formed at the mixed molar ratio of 2:1. In addition, the number of spherulitic J-aggregates decreases with the increase in the mixed molar ratio. When the mixed molar ratio increases to 10:1, there are very few J-aggregate spherulites observed.

Spherulitic J-aggregates can be disrupted by sonicating spherulite solution in an ultrasonic bath (Figure 14a,b). The J-aggregate fibrils broken from the spherulites were examined with atomic force microscopy (AFM) and transmission electron microscopy (TEM). Both individual J-aggregate fibrils and branched fibrils are observed in the AFM image shown in Figure 14c. The J-aggregate fibrils have a smooth surface with the tip at their ends. After the sonication, the intensity of the J-band at 590 nm slightly decreases and a weak H-band at 453 nm appears (Figure 15), suggesting that a small fraction of DiSC₂(3) transits into H-aggregates in the fibrils. We would like to point out that 1 mM LCA is able to self-assemble into nanotubes with a diameter of ~70 nm in 1% w/w ammonia solution only after 1-week incubation (Figure 14d), in which helical ribbons serve as a precursor of LCA nanotubes. The closing of the gap of helical ribbons leads to the formation of nanotubes. However, there is no hollow structure observed in the TEM image of J-aggregate fibrils (Figure 14e). The formation mechanism of J-aggregate fibrils is different than that of LCA nanotubes.

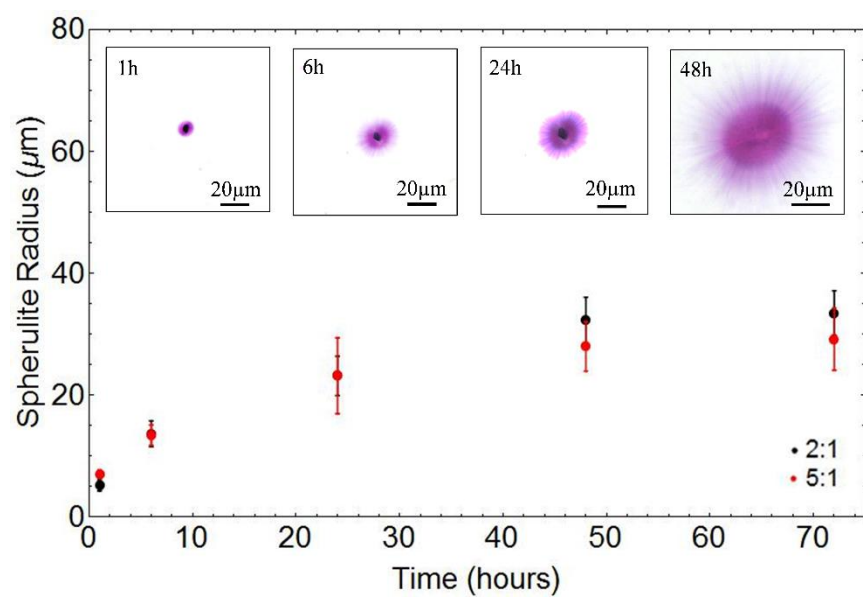


Figure 13 Growth kinetics of J-aggregate spherulites formed in LCA/ DiSC₂(3) solution with a mixed ratio of 2:1 and 5:1. The representative optical microscopy images of J-aggregate spherulites formed at the mixed ratio of 2:1 are inset in Figure 2. The concentration of LCA is 1 mM.

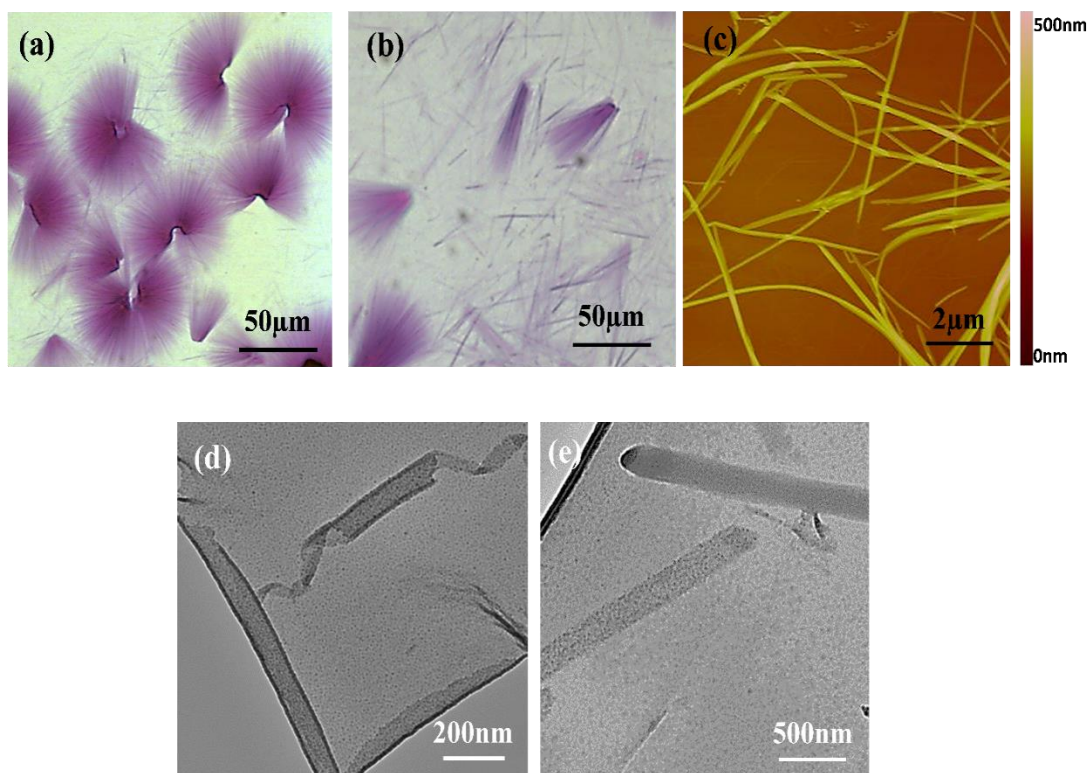


Figure 14 Optical microscopy images of broken spherulitic J-aggregates by (a) 1 min and (b) 5 min sonication time. (c) AFM image of J-aggregate fibrils from broken spherulitic J-aggregates by 10 min sonication. (d) TEM images of LCA nanotubes and (e) J-aggregate fibrils. The spherulitic J-aggregates were formed in LCA/ DiSC₂(3) solution with the mixed ratio of 2:1. The concentration of LCA is 1 mM

Figure 16a shows the time-dependent adsorption spectra of LCA/ DiSC₂(3) solution with the mixed molar ratio of 2:1. In the early stage after the addition of LCA in DiSC₂(3) solution, a broad absorption band with a maximum at 459 nm is observed, suggesting the formation of H-aggregates. The intensity of the less well-defined J-band at 590 nm appears, and its intensity increases over time. There is an isosbestic point in the time-dependent absorptions spectra; that is, the absorbance at 530 nm is not changed during the growth of J-aggregates and the decay of H-aggregates. The isosbestic point represents the equilibrium between J-aggregates and H-aggregates. Figure 16b is the plot of the intensity of the J-band as a function of incubation time,

showing a sigmoidal shape with an initial lag time, followed by a period of rapid growth and finally a slow approach to the equilibrium position. The sigmoidal growth kinetics of J-aggregate fibrils resembles that of amyloid β peptide fibrils[85].

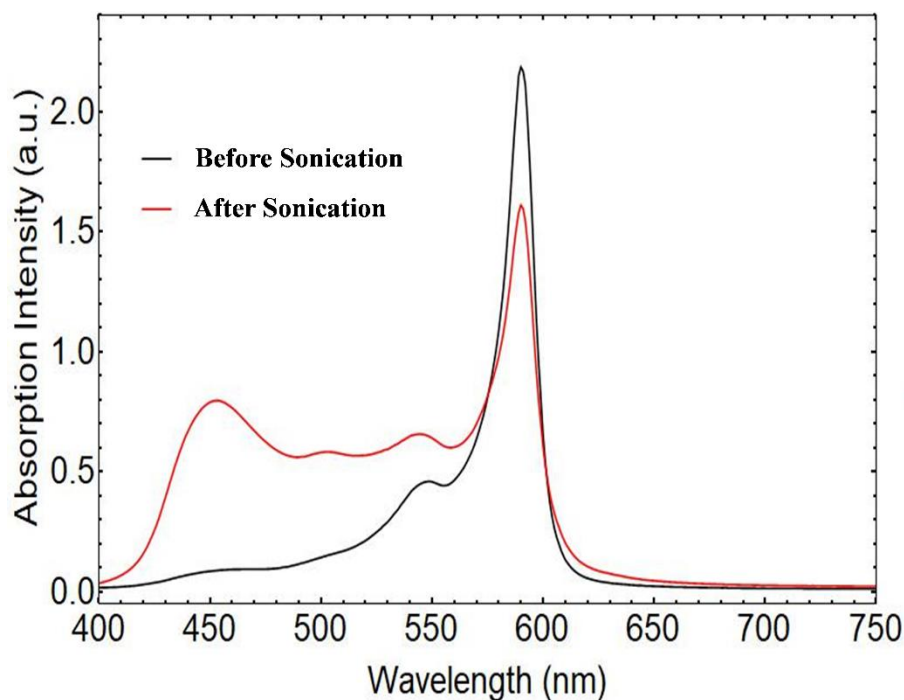


Figure 15 Adsorption spectra of J-aggregate spherulite solution before and after 10 min sonication.

Bile acids are known to form either primary or secondary micelles in aqueous solution as their concentrations approach the critical micelle concentration (CMC)[86]. Primary micelles contain a small aggregation number (2-10) formed through the hydrophobic interaction of bile acids, while secondary micelles are formed via the hydrogen bonding of primary micelles. It has been reported recently that hydrophobic molecules can be incorporated in the hydrophobic cavity of bile acid micelles[87, 88]. In our experiments, the concentration of LCA is 1 mM, which is close to its CMC[81]. Thus, it is reasonable for us to assume that DiSC₂(3) molecules are incorporated in the hydrophobic cavity of LCA micelles through hydrophobic interaction. To verify this

hypothesis, we carried out the co-assembly of LCA and DiSC₂(3) in 1% w/w ammonia solution with the mixed molar ratio of 5:1, where LCA concentration was 0.5 mM, which is lower than its CMC. In this case, a broad absorption band with a maximum at 459 nm is observed (Figure 17). The intensity of the less well-defined H-band at 459 nm remains unchanged even after 24 hours of incubation. The intense J-band at 590 nm, which appears at the LCA concentration of 1 mM, is not observed at the LCA concentration of 0.5 mM.

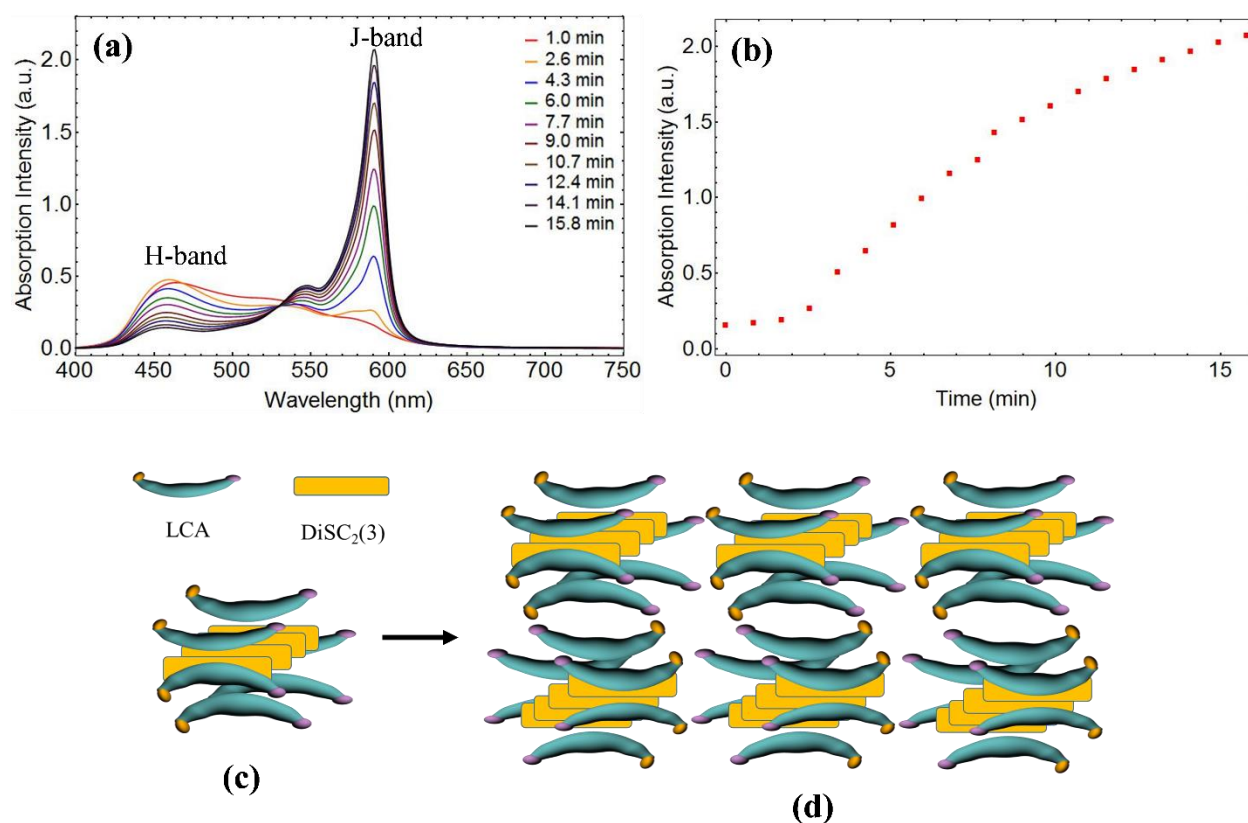


Figure 16 (a) Time-dependent adsorption spectra of LCA/ DiSC₂(3) solution with the mixed ratio of 2:1. (b) Intensity of J-band at 590 nm as a function of incubation time. The concentration of LCA is 1 mM. (c) Schematic representation of a LCA micelle with the J-aggregates of DiSC₂(3) molecules in its hydrophobic cavity and (d) autocatalytic aggregation of J-aggregate incorporated LCA micelles into J-aggregate fibrils.

The length of LCA molecules from its hydroxyl to its carboxyl group (~1.5 nm) is slightly longer than the length of DiSC₂(3) molecules (~1.4 nm). Thus, the hydrophobic cavity of LCA

micelles should be able to accommodate DiSC₂(3) molecules. The formation of the intense J-band at 590 nm suggests that the DiSC₂(3) molecules incorporated in the hydrophobic cavity of LCA micelles form J-aggregates. The number of coherently coupled molecules (N_{coh}) in J-aggregates can be estimated from their absorption spectra according to equation[66]

$$N_{coh} = \frac{3 \Delta v_m^2}{2 \Delta v_j^2} - 1 \quad (5)$$

where Δv_m and Δv_j are the full widths at the half-maxima of the monomer and J-aggregate bands, respectively. On the basis of the adsorption spectra shown in Figure 8c, we estimate that there are four or five DiSC₂(3) molecules incorporated in the hydrophobic cavity of LCA micelles to form J-aggregates (Figure 16c). It has been shown that the carboxylate ion of a LCA engages itself in hydrogen binding with the hydroxyl group of another LCA[70]. The linear aggregation of LCA vesicles through hydrogen binding has been reported in the literature[29]. Thus, we propose that the growth of J-aggregate incorporated LCA micelles through the hydrogen binding.

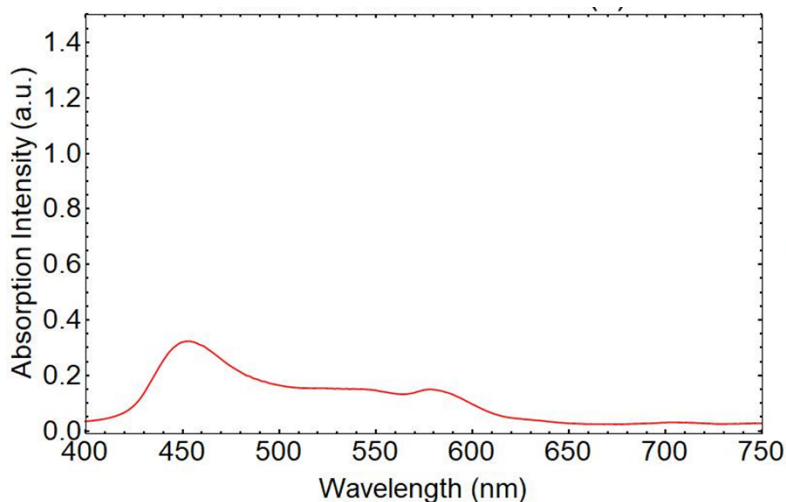


Figure 17 Absorption spectrum of LCA/ DiSC₂(3) solution with the mixed molar ratio of 5:1 after 24-hour incubation at room temperature. The concentration of LCA is 0.5 mM.

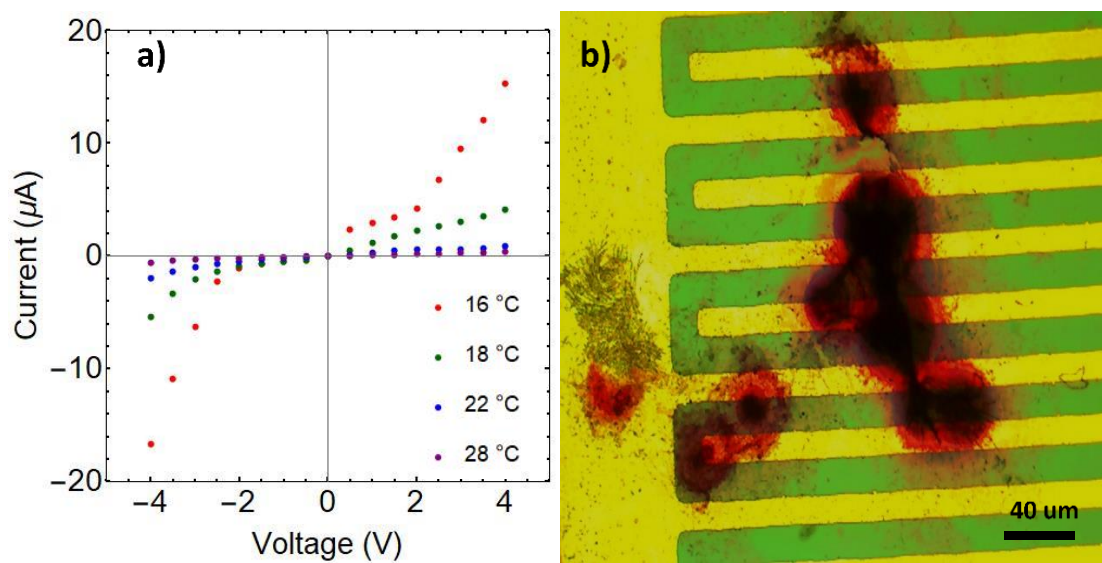


Figure 18 a) IV curves of J-aggregate spherulites and b) J-aggregate spherulites bridging the gap of interdigitated Au electrodes with 20 μm gap.

Upon drying of the J-aggregate spherulites on an interdigitated Au electrode, the IV characteristics of the spherulites were able to be determined. The IV curve of the sample prepared at a 5:1 mix ratio can be seen in Figure 18a. An optical microscope image of the spherulite bridging the electrode can also be seen in Figure 18b. It should be noted that slight variations in the temperature of the sample produced drastically different current levels. At low temperatures, there were much higher current levels than at high temperature and changes in current level could be seen in temperature changes as little as 2°C . The reduction in current is exponential as the temperature increases, with the largest drops occurring in the first few degrees of change. This can be seen in Figure 19a where we measure the current changes as a function of temperature for individual voltage levels. Figure 19b shows the cycling behavior of the J-aggregate spherulites. When cycled between 16°C and 24°C , the current level is reduced by more than half after the first two cycles and then levels off for a time before again dropping after the 14th cycle. These changes in current

level at different temperatures are believed to be caused by a reduction in the number of coherently coupled molecules as the temperature of the J-aggregate fibers increases. As the sample is cycled between low and high temperature, the molecules in the J-aggregate fibers become more and more disjointed and lose their ability to recover as the number of cycles increases.

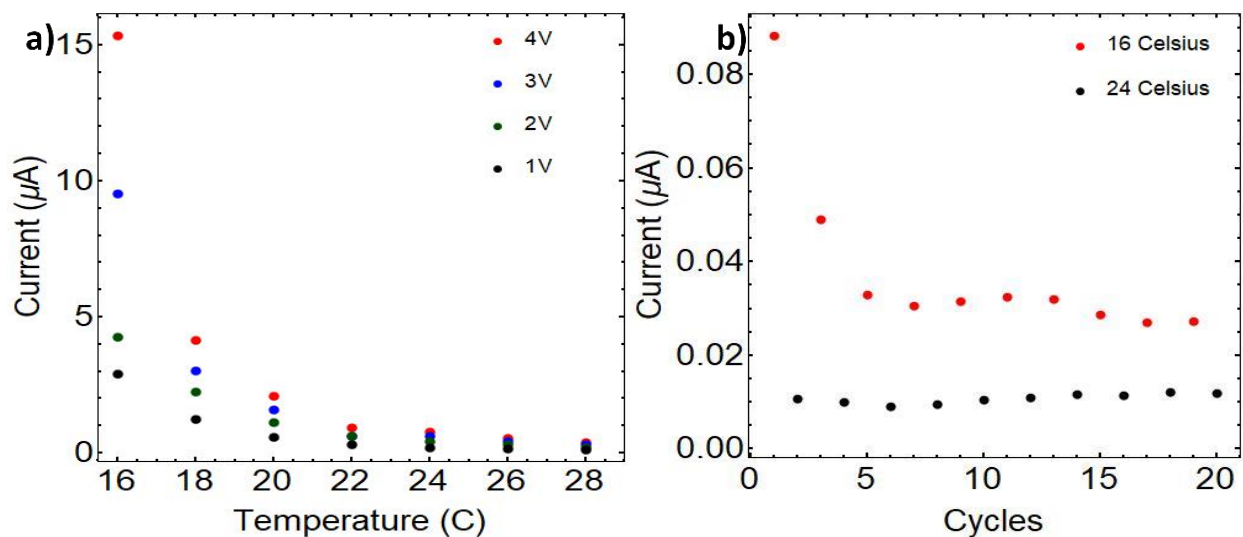


Figure 19 a) Current as a function of temperature at various voltage levels and b) cycle behavior of J-aggregate spherulites under a bias voltage of 3V at 16°C and 24°C.

Another indication this may be the case is that the UV-vis absorption intensity of the J-band is affected by variations in temperature. Results of taking the UV-vis spectrum of the J-aggregate fibrils at different temperatures can be seen in Figure 20a. Similar to the IV curves, there is a noticeable reduction in absorption intensity as temperature of the sample solution is increased. The change from 18°C to 28°C results in a reduction of peak intensity corresponding to nearly 60% which can be seen in Figure 20b showing the absolute percent change of absorption intensity and number of coherently coupled molecules as a function of temperature. The number of coherently coupled molecules could be calculated in the same manner as above and the average

number of coupled molecules decreases as the temperature of the solution is increased with a maximum average decrease of 1.86 molecules.

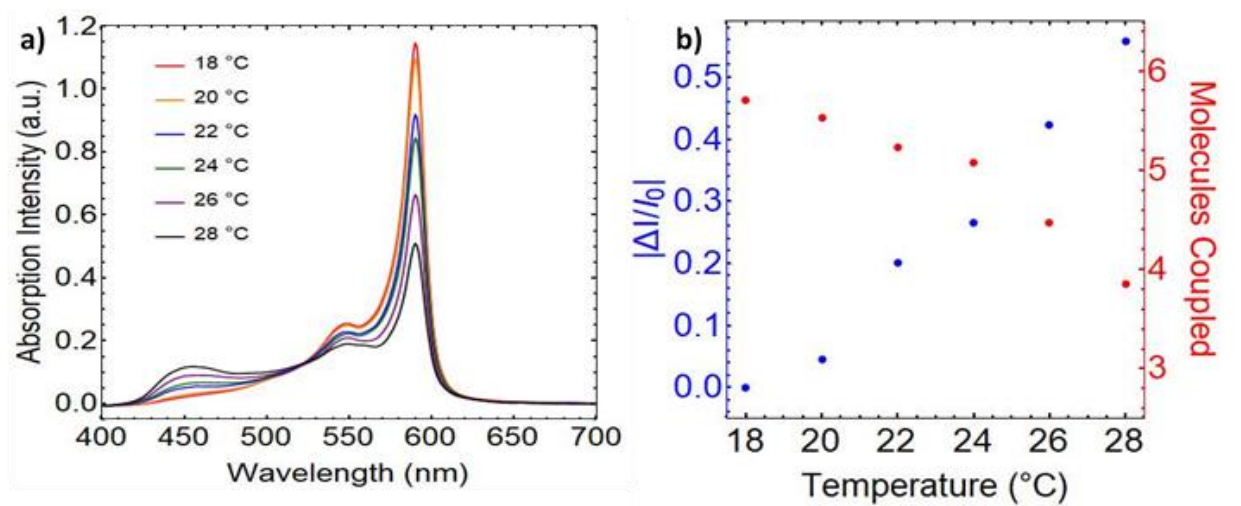


Figure 20 a) UV-vis spectra of J-aggregate spherulites at various temperatures and b) percent change in absorption intensity and number of molecules coupled as a function of temperature.

In conclusion, we report the spherulitic J-aggregates formed by the co-assembly of LCA and DiSC₂(3) in ammonia solution. Microscopy studies show that the spherulites contain a core, which serves as a nucleus for the growth of J-aggregate fibrils. Spectroscopy studies reveal that the growth of spherulitic J-aggregates follows a sigmoidal kinetic curve with an initial lag time, followed by a period of rapid growth and finally a slow approach to equilibrium. On the basis of spectroscopy measurements, we estimate that there are four or five DiSC₂(3) molecules in LCA micelles to form J-aggregates through the hydrophobic interaction. The linear aggregation of J-aggregate incorporated LCA micelles through the hydrogen binding leads to the growth of J-aggregate fibrils.

The J-aggregate spherulites are capable of bridging the gap of an electrode and exhibit temperature-dependent electrical properties that are semi-reversible and cyclable. The changes in

the IV curves can be explained by the decrease in the number of coherently coupled molecules as the temperature of the sample is increased which is evidenced by a corresponding decrease in the absorption intensity upon heating of the sample solution. The average decrease in number of coupled molecules between low temperature (18°C) and high temperature (28°C) is nearly 2 molecules.

In the following chapter, we examine the structure and properties of co-assembled structures formed by DiSC₂(3) and LCA at higher ammonia concentrations.

CHAPTER 3: CONTROLLED FORMATION OF J- AND H-AGGREGATE FIBERS BY THE CO-ASSEMBLY OF CYANINE DYES AND BILE ACIDS

3.1 Introduction

There has been great interest in designing one-dimensional (1D) supramolecular structures of π -conjugated molecules for the development of organic electronic and optoelectronic devices[89-94]. The arrangement of π -conjugated molecules in 1D supramolecular structures defines their physical properties and consequently device performances. Among various 1D supramolecular structures, J- and H-aggregates of π -conjugated dye molecules are particularly interesting because of their unique optical and excitonic properties that are not given by individual dye molecules[53]. H-aggregates are composed of dye molecules in a face-to-face stacking, giving rise to a blue-shifted absorption band compared with the monomer band and a strong emission quenching. In contrast, J-aggregates represent an edge-to-edge stacking of dye molecules, showing a red-shifted absorption band with respect to the monomer band and a strong fluorescence emission[38, 40]. It has been shown that the optical and excitonic properties of J- and H-aggregates depend on their dimensions and morphologies.

Inspired by the antennae of photosynthetic green sulfur bacteria, which is the most efficient natural light-harvesting complexes, in which large numbers of bacteriochlorophylls organize into 1D supramolecular aggregates with delocalized excitation[95], there has been great interest in designing J-aggregate ribbons, fibers, and tubes to achieve excellent optical and excitonic properties for electronic and optoelectronic applications. Cyanine dyes are a highly conjugated molecule composed of two nitrogen-containing heterocyclic rings, which are linked by a polymethine bridge[52]. Great efforts have been made in the use of the self-assembly of

amphiphilic cyanine dyes with the hydrophobic substituents chemically linked to their chromophores to form J-aggregate nanotubes[55-57, 60-63, 96-98]. However, it is still a challenge to form H-aggregate fibers and tubes using the self-assembly of amphiphilic cyanine dyes[99]. Recently, the co-assembly of structurally different molecules has been proven to be a promising approach for forming 1D supramolecular structures without requiring time-consuming processes for the synthesis of amphiphilic molecules, in which the structure and properties can be easily tuned by properly choosing molecules[100-102]. Lithocholic acid (LCA) is a biological surfactant having a rigid and planar steroid backbone and a carboxyl group linked to the steroid backbone through a short alkyl chain[67]. Due to its unique self-assembly capability[29, 68, 70, 72, 73], LCA has been used as a directing agent to organize other molecules into 1D supramolecular structures such as ribbons and tubes at different length scales[74-78, 103, 104].

Here, we report the use of the co-assembly of 3,3'-diethylthiacarbocyanine iodide ($\text{DiSC}_2(3)$) and lithocholic acid (LCA) in ammonia solution to control the formation of J- and H-aggregate fibers by altering the condition under which the co-assembly occurs. Specifically, we find that the co-assembly of $\text{DiSC}_2(3)$ and LCA in 30% ammonia solution at the mixed molar ratio of 5:1 and 2:1 form H-aggregate fibers. When the mixed molar ratio is reduced to 1:1, the co-assembly of LCA and $\text{DiSC}_2(3)$ leads to the formation of H-/J-aggregate hybrid rods, which split into J-aggregate fibers as ammonia evaporates. The electronic properties of J- and H-aggregate fibers placed on interdigitated gold electrodes are measured as a function of temperature.

3.2 Experimental

3.2.1 Materials

Lithocholic acid (LCA), 3,3'-diethylthiacarbocyanine iodide (DiSC₂(3)), and ammonia water were purchased from Sigma-Aldrich and used without further purification. Water used in our experiments was purified with an Easypure II system (18 MΩ cm, pH 5.7). Holey Formvar filmed grids were from SPI.

3.2.2 Methods

The co-assembly of LCA and DiSC₂(3) with different mixed molar ratios was carried out in 1%, 5%, 10%, 15% and 30% w/w ammonia solution, in which the concentration of LCA was always kept at 1 mM. The mixture was sonicated in an ultrasonic bath (Branson 1510, Branson Ultrasonics Co.) at ~23°C for 5 min and then allowed to sit in the dark overnight for the formation of J- and H-aggregate fibers.

Interdigitated gold (Au) electrodes were formed with a conventional photolithography process. Briefly, a 100 nm thick SiO₂ insulation layer was first grown on a 3-inch Si wafer by thermal oxidation process. A metallic seed film which consists of 100 nm Au layer over 10 nm Ti layer was then deposited on the top of the SiO₂ layer by e-beam evaporation. A thin layer of positive photoresist (Microposit S1813, Dow Electronic Materials) was then spin-coated (3000 rpm, 30 sec), soft-baked (105 °C, 3 min), exposed under I-line UV aligner (8 seconds) and developed (Microposit MF CID-26 Developer, 35 sec) to obtain photoresist patterns for the interdigitated electrodes with a gap of 20 μm. The developed patterns were hard-baked at 105°C for 10 min) and used as a protective layer for subsequent etching steps. The Au/Ti seed layer in exposed areas was chemically etched with an Au etchant (KI and I₂ mixture solution) and a Ti

etchant (0.5% HF). The remaining photoresist was dissolved in acetone and the interdigitated Au electrodes were formed after cleaning in methanol and deionized water. The interdigitated Au electrodes were cleaned with deionized water before the deposition of J and H-aggregate fibers. In our experiments, 4 μ L J- and H-aggregate fiber solution was dropped on the interdigitated Au electrodes and dried in air at room temperature.

3.2.3 Instruments

The structure and morphology of supramolecular aggregates from the co-assembly of LCA and DiSC₂(3) were characterized with an optical microscope (Olympus BX), a scanning electron microscope (SEM, Hitachi S3500N), and an atomic force microscope (AFM, Dimension 3100 from Veeco Instruments). The optical properties of the supramolecular aggregates were characterized with a Cary 300 Uv-vis spectrophotometer. For SEM measurements, aggregate solution was dried on a holey Formvar filmed grid at room temperature for 24 hours and then imaged at an accelerating voltage of 20 kV. AFM images were taken with a silicon nitride cantilever (Nanosensors) with a spring constant of 30 N/m and a resonant frequency of 260 kHz in tapping mode. For optical microscope observations, a drop of aggregate solution was placed on a glass substrate, followed by placing a cover slide on the top of the drop. Current-voltage (I-V) measurements were performed with a Keithley 2400 sourcemeter.

3.3 Results and Discussion

The chemical structure of DiSC₂(3) and LCA is shown in Figure 21a and b, respectively. LCA has a carboxyl group and several chiral centers. It was shown that the interplay of electrostatic, van der Waals, and chiral interactions was responsible of the self-assembly behavior of LCA in aqueous solution. In a previous publication, we showed that LCA and DiSC₂(3) at the

mixed molar ratio of 1:1, 2:1 and 5:1 were able to co-assemble into spherulitic J-aggregates in 1% w/w ammonia solution[104]. In each case, the concentration of LCA was kept at 1 mM, which was higher than its critical micelle concentration (CMC). There was no J-aggregation observed if the co-assembly of LCA and DiSC₂(3) occurred at an LCA concentration below 1 mM. In our current work, the co-assembly of LCA and DiSC₂(3) with the molar ratio of 1:1, 2:1 and 5:1 was carried out in aqueous solution with the ammonia concentration from 1% to 30%, in which the concentration of LCA was kept at 1 mM. The absorption spectra from the co-assembly at the molar ratio of 5:1 reveals a sharp J-band at 590 nm, which is red-shifted with respect to the monomer band of DiSC₂(3) (556 nm), in the ammonia concentration from 1% to 15% (Figure 21c). The J-aggregates from the co-assembly of LCA and DiSC₂(3) show a spherulitic morphology containing a core surrounded by radially oriented fibrils (Figure 21d).

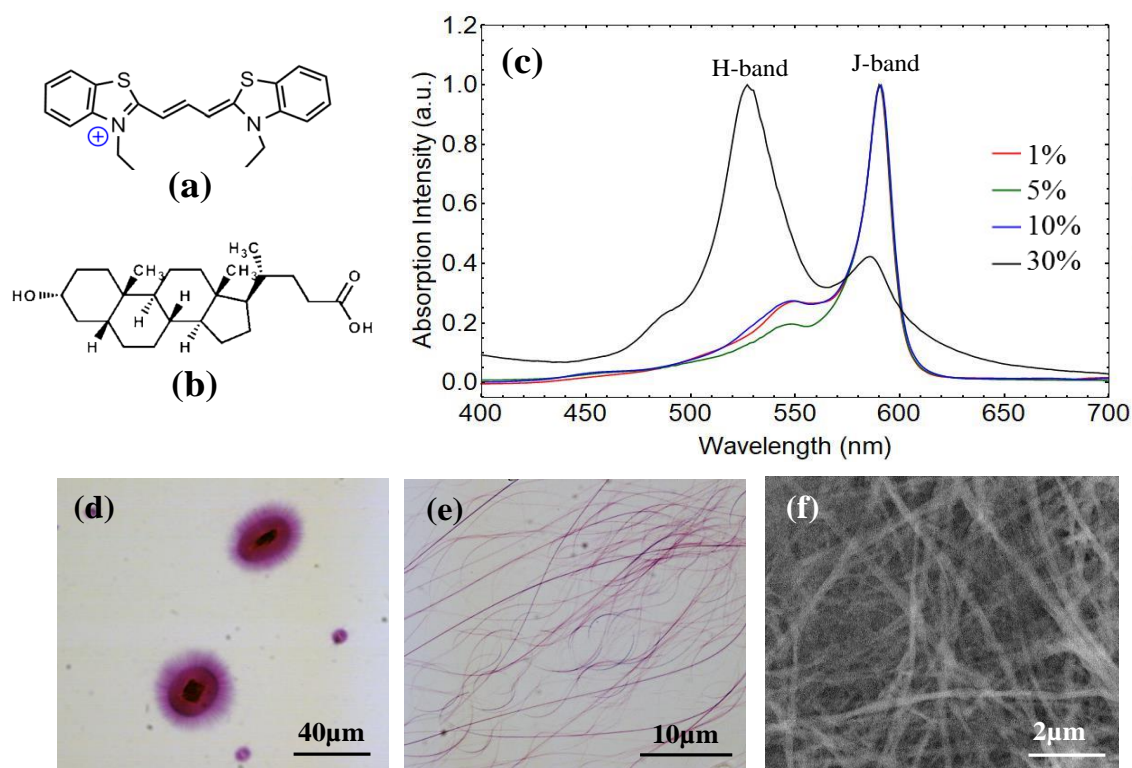


Figure 21 Chemical structures of (a) DiSC₂(3) and (b) LCA. (c) absorption spectra of LCA/DiSC₂(3) solution with the mixed ratio of 5:1 after 24 hour incubation at room temperature in 1%, 5%, 10% and 30% w/w ammonia solution. (d) Optical microscopy image of J-aggregate spherulites. (e) and (f) are optical microscopy and SEM images of H-aggregate fibers

The J-band at 590 nm significantly decreases as the ammonia concentration increases to 30%. Instead, we observed a sharp and intense H-band at 530 nm (Figure 21c), which is blue-shifted with respect to the monomer band of DiSC₂(3) (556 nm). The H-aggregates have a fiber-like morphology with pink color (Figure 21e). The pink color suggests the incorporation of DiSC₂(3) in the fibers. The sharp and blue-shifted H-band at 530 nm indicates that the incorporated DiSC₂(3) forms H-aggregates. Figure 21f shows the typical SEM image of the H-aggregate fibers. The diameter of H-aggregate fibers is in the range from 200 nm to 300 nm. The bundles of H-aggregate fibers are also visible in Figure 21f. It is clear that the formation of J-aggregate

spherulites and H-aggregate fibers follows different pathways. We note that the solubility of DiSC₂(3) molecules in 1% ammonia solution is low.

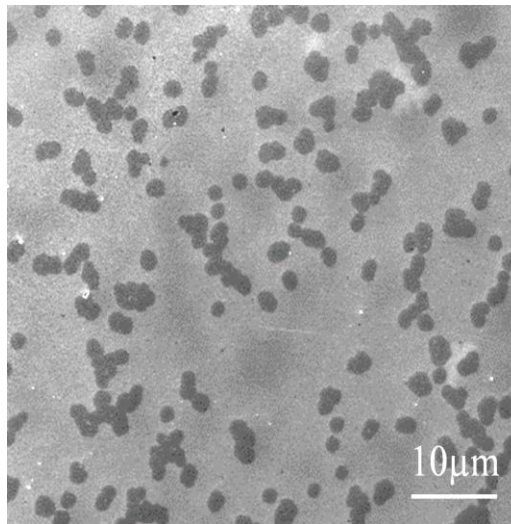


Figure 22 SEM image of random aggregates of 0.2 mM DiSC₂(3) in 1% ammonia solution.

They randomly aggregate together to form particles (Figure 22). Thus, the J-aggregate fibers from the co-assembly of LCA and soluble DiSC₂(3) in 1% ammonia solution efficiently nucleate on the surface of the random aggregated particles, resulting ultimately in the formation of J-aggregate spherulites (Figure 21d). The solubility of DiSC₂(3) in 30% ammonia solution is significantly improved. There is no random aggregate particle of DiSC₂(3) observed. In this case, the H-aggregate fibers from the co-assembly of LCA and DiSC₂(3) nucleate and grow in solution (Figure 21e). Our results also show the nature of the aggregation of DiSC₂(3) in the fibers depends on the co-assembly pathways. DiSC₂(3) forms J-aggregates in the fibers grown out from the surface of the randomly aggregated particles, while the H-aggregates of DiSC₂(3) are formed in the fibers grown in solution.

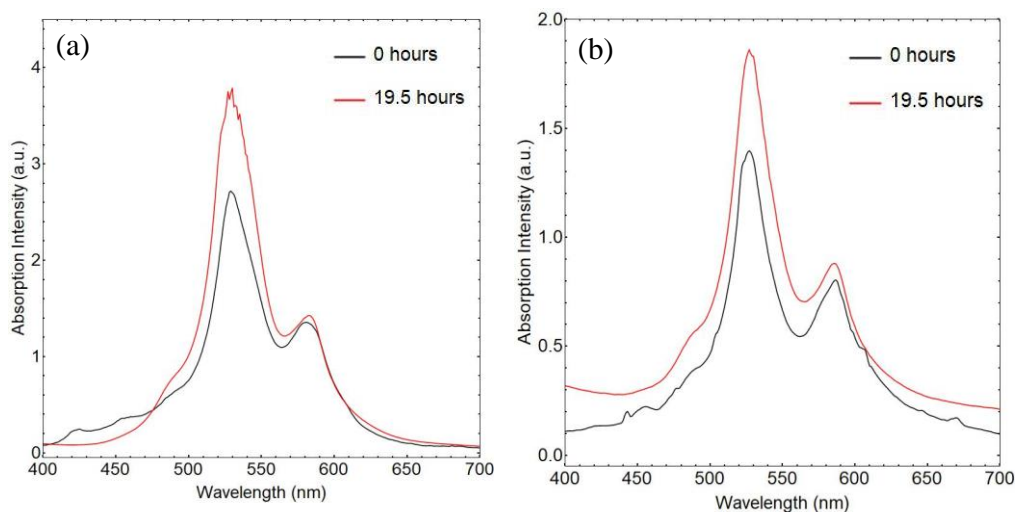


Figure 23 Absorption spectra of H-aggregate fibers from the co-assembly of LCA and DiSC₂(3) with the molar ratio of (a) 2:1 and (b) 5:1 in 30% ammonia solution before and after 19.5 hours of evaporation at room temperature.

The sharp H-band at 530 nm is also observed from the co-assembly of LCA and DiSC₂(3) with molar ratio of 2:1 in 30% ammonia solution (Figure 23a). However, when the molar ratio of LCA and DiSC₂(3) is reduced to 1:1, a broad band with the maximum at 426 nm is observed (Figure 24a), which is blue-shifted with respect to the monomer band of DiSC₂(3). Surprisingly, the change of the absorption spectra takes place as ammonia evaporates at room temperature. The broad H-band decreases, while a well-defined J-band at 590 nm appears and rapidly increases over time as the evaporation progresses. Figure 24b is the plot of the intensity of the sharp J-band at 590 nm and broad H-band with the maximum at 426 nm as a function of evaporation time. The broad H-band gradually decreases over time as the evaporation of ammonia takes place. The intensity of the J-band shows a sigmoidal shape with an initial lag time (~ 9 hours) followed by a period of rapid growth and reaches a saturation region after 19 hours.

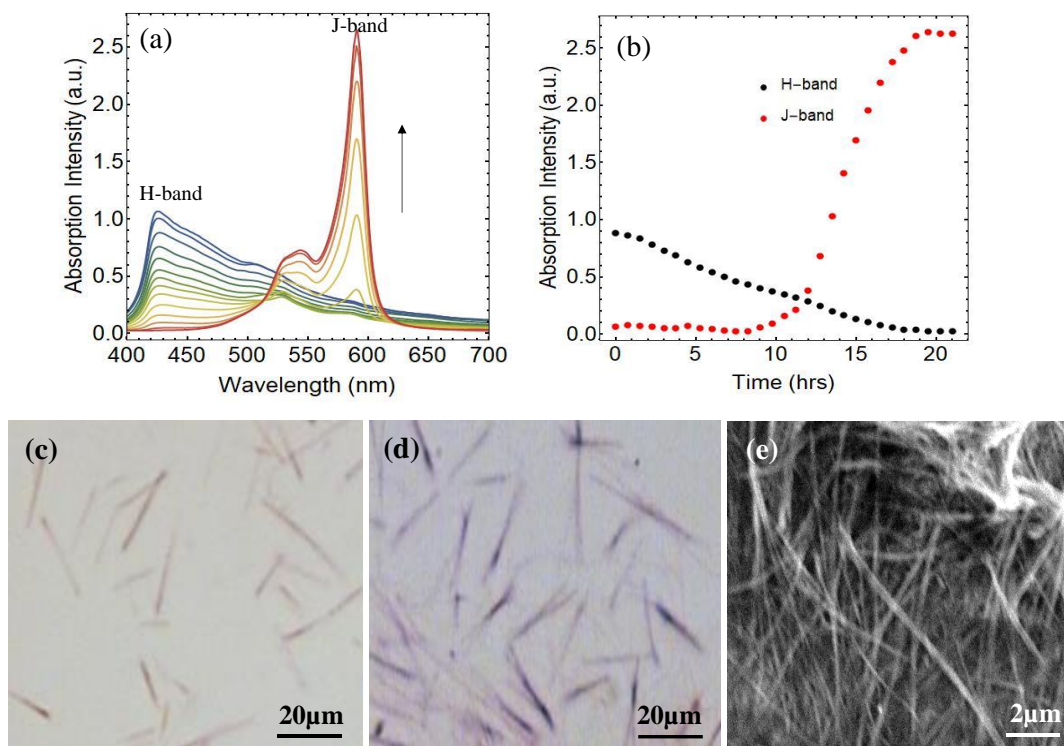


Figure 24 (a) Time-dependent absorption spectra of LCA/DiSC₂(3) solution with the mixed ratio of 1:1 as the evaporation of ammonia solution takes place at room temperature. (b) Intensity of J-band at 590 nm and H-band at 426 nm as a function of evaporation time. Optical microscopy of H-/J-aggregate hybrid rods (c) before and (d) after 19 hours evaporation time. (e) SEM image of J-aggregate fibers from the splitting of H-/J-aggregate hybrid rods.

This result indicates that the H- to J-aggregate transition begins to take place after 9 hours evaporation and completes after 19 hours evaporation, at which time the H-band completely disappears. An image of the solution before and after the evaporation process can be seen in Figure 25a and Figure 25b, respectively. There is no H- to J-aggregate transition observed for H-aggregate fibers with the sharp H-band at 530 nm from the co-assembly of LCA and DiSC₂(3) with the molar ratio of 5:1 and 2:1 in 30% ammonia solution (Figure 23).

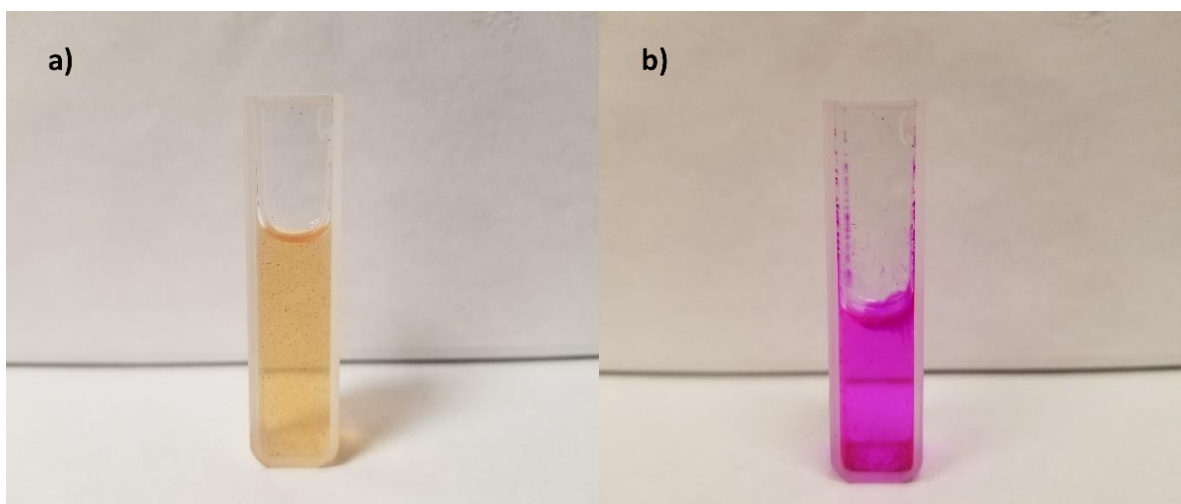


Figure 25 a) H-aggregate solution formed at a 1:1 molar ratio before evaporation takes place and b) J-aggregate solution formed at a 1:1 molar ratio via the evaporation of ammonia after 24-hours evaporation time.

Optical microscopy observations show that the H-aggregates have a rod-like morphology with brown color (Figure 24c). The H-aggregate rods have the length in the range from 25 μm to 40 μm . They appear to be unstable. After 15 hours evaporation of ammonia at room temperature, the rods split into fibers at their ends and their color shifts to a dark purple (Figure 24d). After 20 hours evaporation, a large amount of dispersed fibers through the splitting of rods are observed (Figure 24e). After being excited at 580 nm, the J-aggregate fibers show a strong emission at 610 nm and can be clearly seen with a fluorescent microscope (Figure 26), which is another feature of J-aggregates besides the red-shifted absorption band at 590 nm.

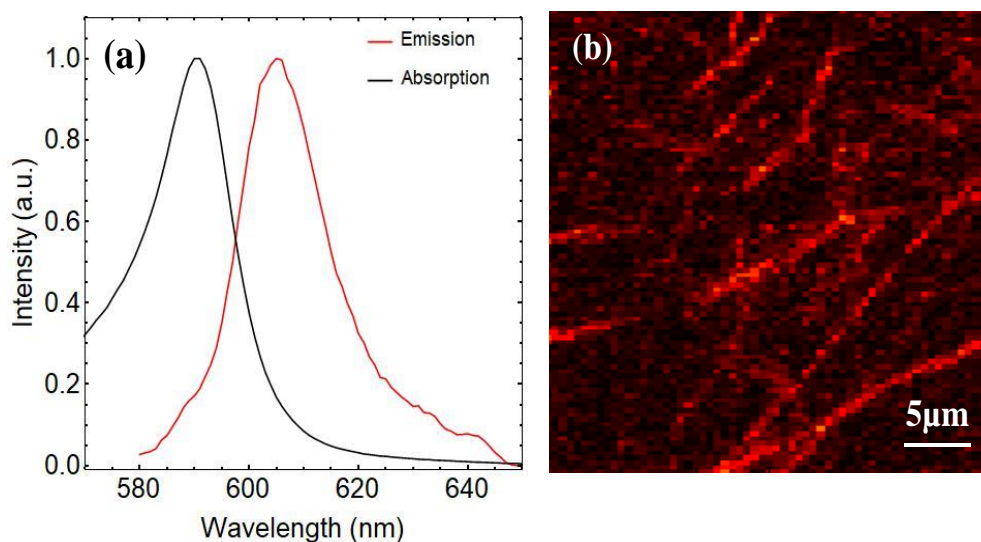


Figure 26 (a) Absorption and emission spectra of J-aggregate fibers formed from the co-assembly of LCA and DiSC₂(3) with the molar ratio of 1:1 in 30% ammonia solution. (b) Fluorescent microscope image of J-aggregate fibers

The H- to J-aggregate transition of individual rods can be in situ monitored with a polarizing optical microscope (POM) during the drying of a drop of solution on a glass substrate, in which the evaporation occurs rapidly. As can be seen in the POM images shown in Figure 27a, three rods marked with white circles show initially blue color and then transform into a red color within 10 minutes. The blue-to-red color transition starts from the ends of the rods and then extends along their long axis (Figure 27b and c). The different colors of H- and J-aggregates in POM images can be explained by their different absorption regions[105]. Thus, which light illumination under a POM can provide different transmission of colors. The apparent diameter of the rods in the POM image enlarges after the H- to J-aggregate transition (Figure 27c). The enlarged diameter is a result of the splitting of the rods, which is evident in the AFM image shown in Figure 27d. The AFM image shows that the rods appeared in the optical microscopy images (Figure 24c, Figure 27a) are actually the bundles of tightly packed fibers. After being dried on glass substrates, the

rods split into fibers from their ends to form sheaf-like bundles, in which individual fibers with the diameter of 120 ± 20 nm and the length of 30-40 μm are clearly visible in the AFM image.

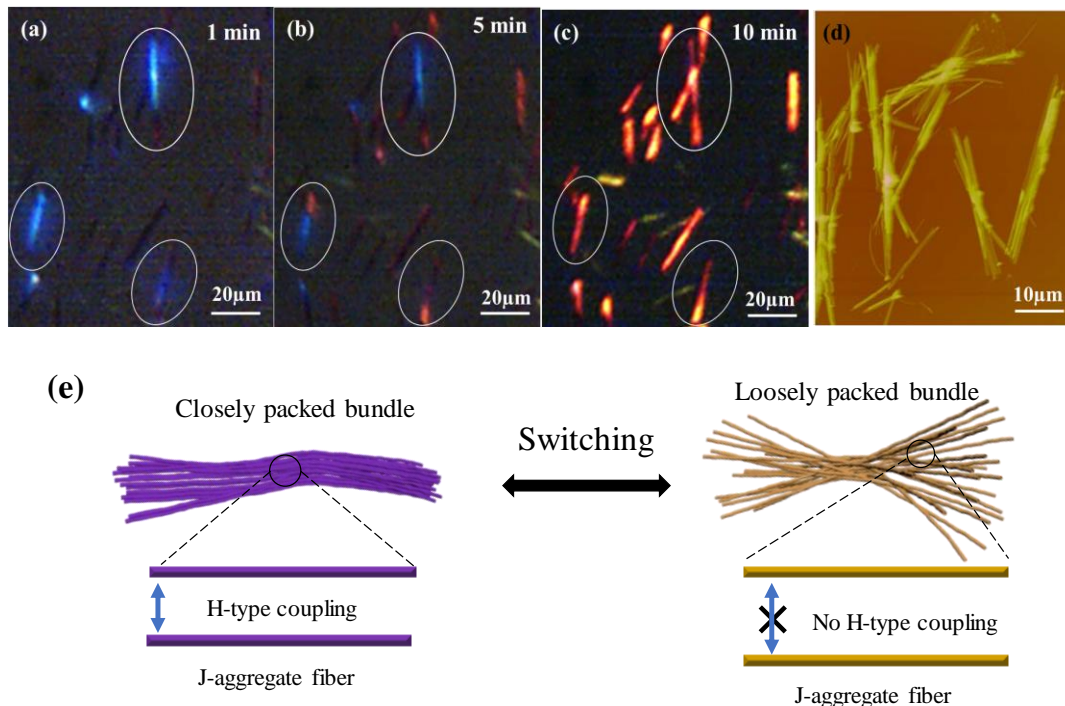


Figure 27 (a – c) Polarized optical microscopy images of H-/J-aggregate hybrid rods during the drying of a drop of rod solution on a glass substrate. (d) AFM image of H-/J-aggregate rods dried on glass substrate. (e) Schematic representation of H- to J-aggregate transition during the splitting of H-/J-aggregate rods

The absorption spectra shown in Figure 24a reveals that DiSC₂(3) forms J-aggregates in the fibers split from the rods. The broad H-band of the rods is likely due to the formation of the possible H-type coupling of the DiSC₂(3) molecules in the neighboring J-aggregate fibers, which are tightly packed in the rods (Figure 27e). The H-type coupling of interfibers may mark (suppress) the J-coupling of DiSC₂(3) molecules in the fibers, leading to the apparent optical property of rods resembling H-aggregate character. The splitting of fibers breaks the H-coupling of interfibers and restores the J-aggregate character of the fibers (Figure 27e). Thus, the rods can be considered as a J-/H-aggregate hybrid system.

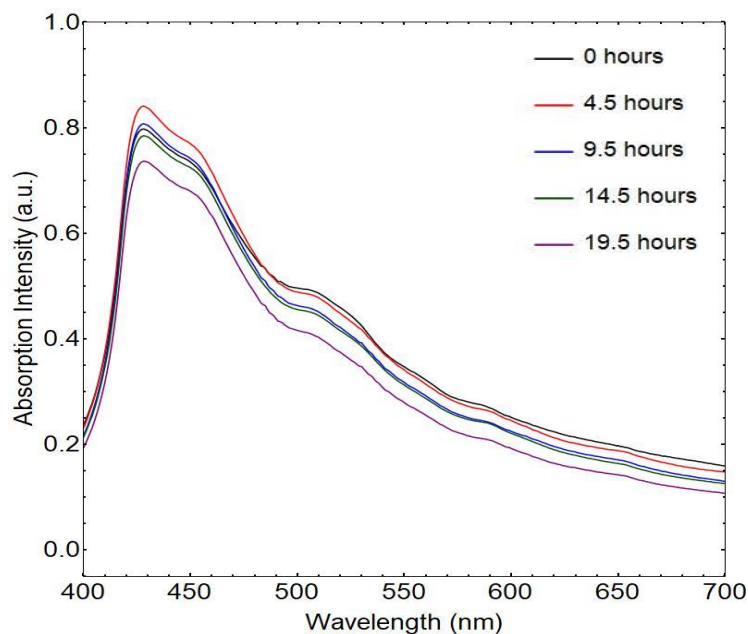


Figure 28 Absorption spectra of H-/J-aggregate rods formed from the co-assembly of LCA and DiSC₂(3) with the molar ratio of 1:1 in 30% ammonia solution as a function of time. The rod solution was sealed in a glass bottle.

Our control experiments show that there is no H- to J-aggregate transition if the rod solution was sealed in a glass bottle (Figure 28), suggesting that the evaporation of ammonia causes the splitting of H-/J-aggregate hybrid rods. The pK_a value of LCA is ~ 7.0 . In 30% ammonia solution with pH 11.2, LCA should be deprotonated. Thus, J-aggregate fibers should be negatively charged. The interplay between van der Waals attraction and electrostatic repulsion should contribute to the formation and splitting of rods (bundles of J-aggregate fibers). The formation of rods is likely to be a result of the charge screening of J-aggregate fibers by NH_4^+ counterions. As the evaporation of ammonia occurs, the concentration of NH_4^+ counterions will drop. The electrostatic repulsion of J-aggregate fibers causes the splitting of the rods. To verify this hypothesis, we restored J-aggregate fiber solution back to its original volume by filling 30% ammonia solution. As can be seen in Figure 29a, the sharp J-band at 590 nm significantly decreases 24 hours after the addition

of 30% ammonia solution. Two H-bands appear, one at 426 nm and the second at 525 nm. The appearance of the H-bands is due to the interaction of DiSC₂(3) molecules in adjacent J-aggregate fibers in the rods, which masks the J-band at 590 nm. Optical microscopy images reveal that purple J-aggregate fibers recombine together to form brown H-/J-aggregate hybrid rods due to the charge screening as the concentration of NH₄⁺ counterions increases, reverting to H-type coupling (Figure 29b and c). Our observations confirm the rods are J-/H-aggregate hybrid systems, in which H-type coupling among the fibers masks the J-type coupling in the fibers. The absorption spectra show that there is no J- to H-aggregate transition taken place after the addition of 500 mM NaCl (Figure 29a). In this case, loosely packed bundles of J-aggregate fibers are observed (Figure 29d). There is no color change taken place after the formation of loosely packed bundles. The lateral interaction of J-aggregate fibers is responsible for H-type coupling. This result may suggest that Na⁺ counterions partially mask the electrostatic repulsions between J-aggregate fibers, leading to the formation of loosely packed bundles, in which the H-coupling does not occur. It has been shown that NH₄⁺ counterions can induce the formation of hexagonally packed bundles of self-assembled LCA tubes[68]. While the highly ordered organization of LCA tubes is not observed in Na⁺ counterions. The fine charge screening by NH₄⁺ allows van der Waals attraction to overwhelm the electrostatic repulsion of J-aggregate fibers to form closely packed bundles, in which the H-type coupling between J-aggregate fibers occurs. The H-type coupling of J-aggregate fibers from the co-assembly of LCA and DiSC₂(3) is similar to that which occurs from the assembly of conjugated polymers, which also exhibit two classes of electronic couplings: J-type coupling within a polymer chain and H-type coupling between polymer chains when they bundled together. The increase of the separation distance between the polymer chains breaks the H-coupling[106].

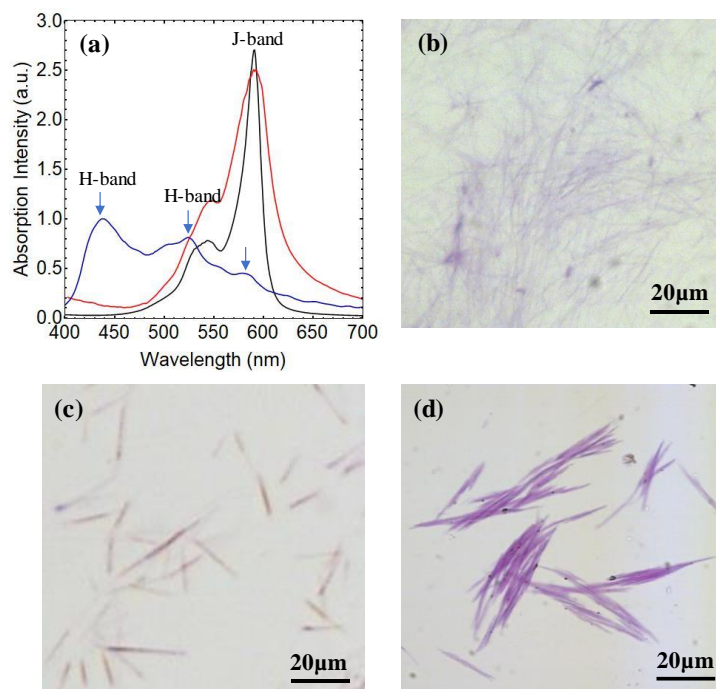


Figure 29 (a) Absorption spectra of J-aggregate fiber solution before (black) and after the addition of 1 mL 30% ammonia solution (blue) and 500 mM NaCl (red). (b) Optical microscopy images of dispersed J-aggregate fibers (c) H-/J-aggregate hybrid rods after the addition of 1 mL 30% ammonia solution and (d) loosely packed J-aggregate fiber bundles after the addition of 500 mM NaCl

The current understanding of electronic transport properties of J- and H-aggregates, even for the well-studied J-aggregate tubes, is rather limited[107, 108]. To exploit the potential application of J-and H-aggregate fibers in electronic devices, we measure their electrical properties by depositing them on the interdigitated Au electrodes with a gap of 20 μm , which were fabricated on a SiO_2 substrate by photolithography and a schematic representation can be seen in Figure 7. The electronic transport through the H- and J-aggregate fibers should depend on both the properties of the fibers and the fiber-electrode contact. The bridging of the deposited H-aggregate fibers of the gap between the Au electrodes was confirmed by AFM (Figure 30a).

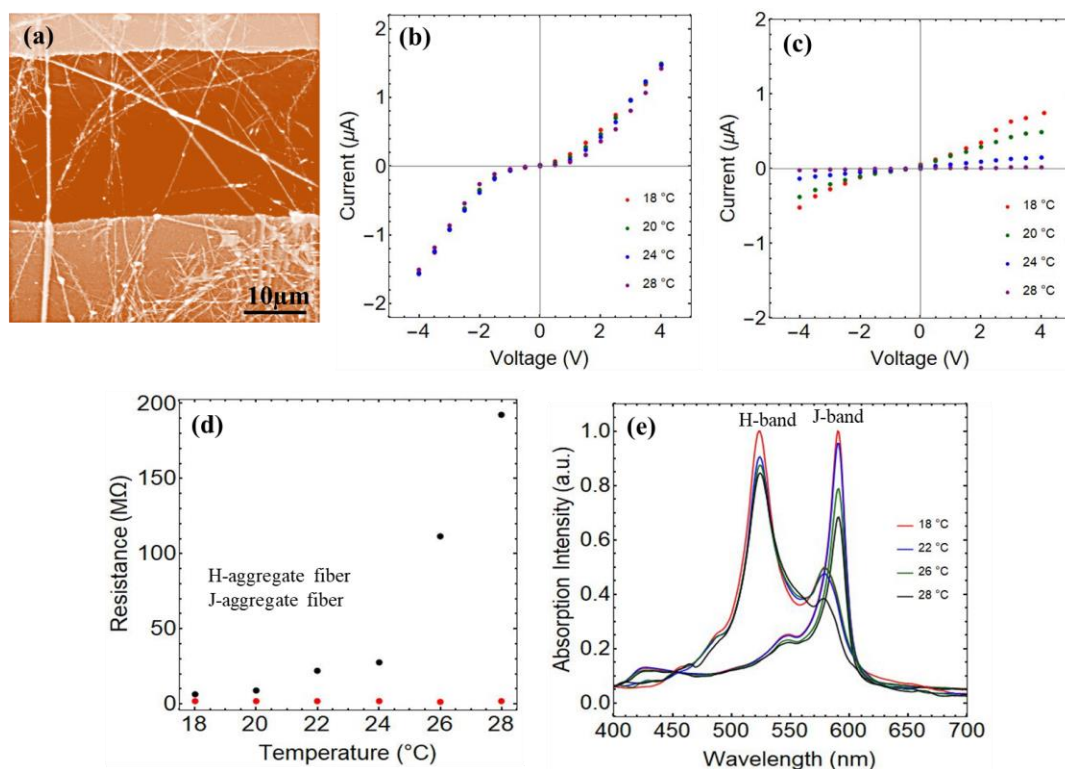


Figure 30 (a) AFM image of H-aggregate fibers bridging the 20 μm gap between interdigitated Au electrodes. (b) Temperature-dependent I-V curves of H-aggregate fibers and (c) J-aggregate fibers. (d) Resistance of H- and J-aggregate fibers as a function of temperature and (e) temperature-dependent absorption spectra of J- and H-aggregate fibers in solution.

We find that the I-V curves of H-aggregate fibrils are non-linear with the threshold voltage of ~ 1.2 V (Figure 30b). Above the threshold, the current I increases rapidly with the increase of voltage. The nonlinear I-V curves suggest the Schottky contact between the H-aggregate fibers and the Au electrodes. In contrast, the I-V curves of J-aggregate fibers are linear (Figure 30c), suggesting the Ohmic contact of the J-aggregate fibers and the Au electrode. The different contacts of J- and H-aggregate fibers with Au electrodes can be explained by their different electron energy levels with respect to the Fermi level of the Au electrodes. In order to obtain the HOMO/LUMO levels of the J- and H-aggregate fibers, cyclic voltammetry was done in 1 M KCl solution with the samples dried on ITO. The scan rate was 1 mV/s. The CV curves of the H- and J-aggregates can

be seen in Figure 31a. The HOMO/LUMO levels were calculated using the empirical equations [109]:

$$E(HOMO) = -e(E_{onset} + 4.4), \quad (6)$$

$$E(LUMO) = E_g + E(HOMO), \quad (7)$$

The band gap energy, E_g , of J- and H-aggregate fibers can be calculated according to the equation[109]: $E_g = 1242/\lambda_{onset}$. For J-aggregate fibers, λ_{onset} is 590 nm and thus E_g is 2.10 eV. For the H-aggregate fibers, λ_{onset} is 530 nm and E_g is 2.34 eV. Based on these values for the band gaps of the H- and J-aggregate fibers we can calculate the HOMO/LUMO levels by finding the onset potential of oxidation in the CV curves provided in Figure 31a. For the H-aggregate fibers, $E(HOMO) = -4.65$ eV and $E(LUMO) = -2.32$ eV. For the J-aggregate fibers, $E(HOMO) = -4.63$ eV and $E(LUMO) = -2.51$ eV. This indicates that the conduction band of the H-aggregate fibers is higher than that of the J-aggregate fibers which agrees with the fact that the excited state of H-aggregates being higher energy than that of J-aggregates. A schematic energy level diagram of H- and J-aggregate fibers together with the Fermi level of Au electrodes is shown in Figure 31b.

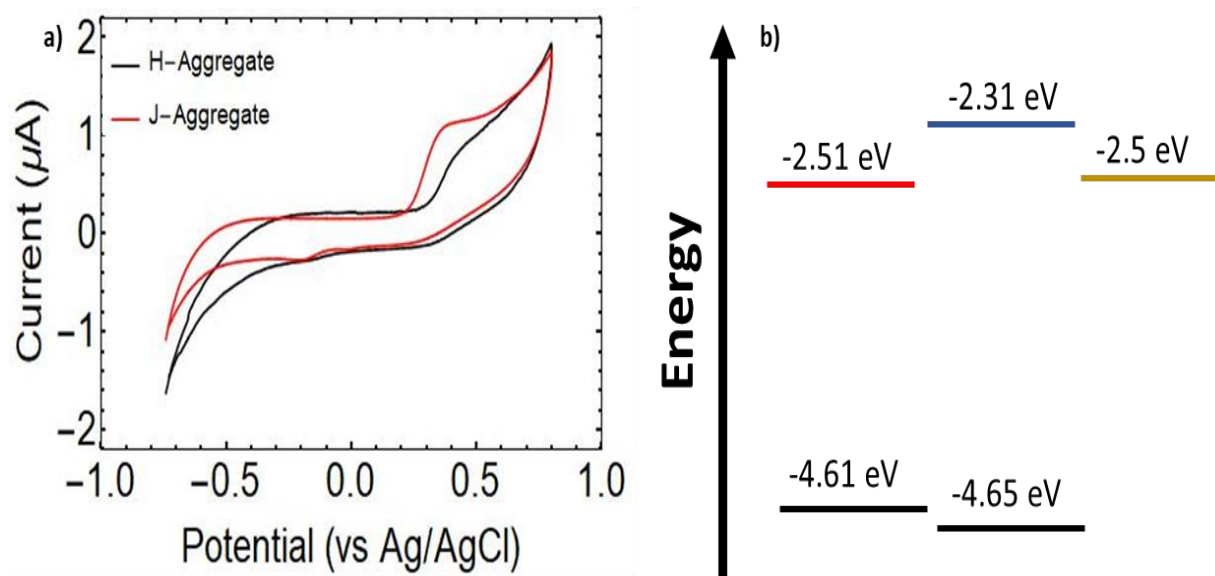


Figure 31 a) CV curves of H-aggregates formed at a 5:1 mix ratio (black) and J-aggregates formed via evaporation of ammonia from 1:1 mix ratio sample (red) done in 1 M KCl solution and b) Energy level diagram of the HOMO/LUMO levels of the H- and J-aggregates compared to the Fermi level of Au. The red line denotes the LUMO level of J-aggregates, blue line the LUMO level of H-aggregates and the gold line is the Fermi level of Au.

The Schottky contact indicates that the Fermi level of Au electrodes is located between the conduction and valence bands of H-aggregate fibers. Thus, a large voltage is required to remove the difference and make the electronic injection from the Au electrode to the H-aggregate fibers. The Ohmic contact indicates that the conduction band of J-aggregate fibers is lower than the Fermi energy of Au electrodes. There is a negligible contact resistance, allowing the electrons to freely flow across the contact. During the drying process on the Au electrodes, the large amount of ammonia ions in solution will adsorb onto the Au electrodes and alter the Fermi level of the Au electrodes[110]. This coupled with changes in the Fermi level due to being at room temperature will bring the Au Fermi level to a value of -2.5 eV which lines up almost exactly with the conduction band of the J-aggregate fibers and below the conduction band of the H-aggregate fibers[111]. In addition, the I-V curves of H-aggregate fibers are only slightly affected by

temperatures in the range from 18°C to 28°C (Figure 30b). However, large changes in the I-V curves of J-aggregate fibers are observed as the temperature is increased from 18°C to 28°C (Figure 30c). For the H-aggregate fibers, the resistance was calculated from the slope of the linear part of the I-V curves. As can be seen in Figure 30d, the resistance of the H-aggregate fibers remains a near constant of 4 MΩ as the temperature increase from 18°C to 28°C. while the resistance of the J-aggregate fibers increases from 6 MΩ to 190 MΩ as the temperature increase from 18°C to 28°C. To better understand the difference in the temperature-dependent resistances between J-aggregate and H-aggregate fibers, we measure the temperature-dependent absorption spectra of J-aggregate and H-aggregate fibers in solution. Upon heating of the solution from 18°C to 28°C at a rate of 5 degree/minute, the intensity of the J-band drops 37%, while the intensity of the H-band only drops 15% (Figure 30e). Since there is no monomer band observed during the heating, the intensity decrease should be a result of the change of molecular packing in the fibers. Our results suggest that the face-to-face interaction of DiSC₂(3) in the H-aggregate fibers is stronger than the edge-to-edge interaction of DiSC₂(3) in the J-aggregate fibers, which agrees with the results of J- and H-aggregates formed within the groove of DNA templates[112]. The number of coherently coupled molecules (N_{coh}) in the J-aggregate fibers is significantly reduced. N_{coh} can be calculated from the absorption spectra according to Equation (5) [66, 113]. Thus, we use the equation to calculate the N_{coh} , which decreases from 4 to 2 as the increase of temperature from 18 °C to 28°C (Figure 32). This explains the strong temperature-dependent resistance change of J-aggregate fibers.

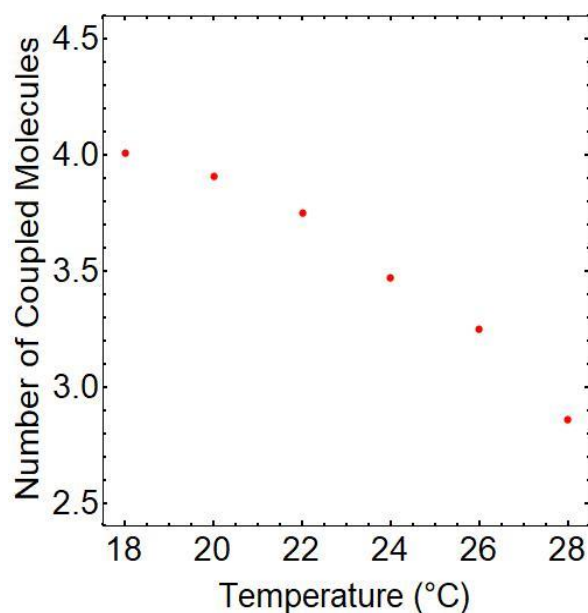


Figure 32 Number of coherently coupled molecules in the J-aggregate fibers as a function of temperature

In summary, we show that the co-assembly of LCA and DiSC₂(3) in NH₄OH solution can lead to the formation of J- and H-aggregate fibers, depending on the condition under which the co-assembly occurs. Significantly, the co-assembly of LCA and DiSC₂(3) at the mixed molar ratio of 5:1 and 2:1 in 30% ammonia solution form H-aggregate fibers. When the molar ratio is reduced to 1:1, the co-assembly of LCA and diSC₂(3) leads to the formation of H-/J-aggregate hybrid rods, which gradually split into J-aggregate fibers as ammonia evaporates. The transition from H-/J-aggregate hybrid rods to J-aggregate fibers is reversible and can be in situ observed by optical microscopy due to their color changes. The I-V curves of interdigitated Au electrodes bridged by J- and H-aggregate fibers shows that H-aggregate fibers form a Schottky junction with Au electrodes and J-aggregate fibers show Ohmic contact with Au electrodes. Our findings offer a simple way for controlling the formation of J- and H-aggregate fibers by the co-assembly of LCA

and DiSC₂(3). The J- and H-aggregate fibers with distinct physical properties might serve as the functional materials for electronic devices.

CHAPTER 4: TWO-STEP ASSEMBLY OF H- AND J-AGGREGATE COATINGS ON LITHOCHOLIC ACID BASED NANOTUBES

4.1 Introduction

Self-assembled supramolecular structures have been of great interest in the scientific community over the last two decades due to their wide range of potential applications. Of most interest has been the structures formed by amphiphilic molecules, of which an important class is the surfactant. Surfactants are able to self-assemble into a wide range of geometries with a wide range in sizes[114]. These structures have been studied for their potential in microelectronics, as drug delivery systems, and for their unique encapsulation abilities[115]. As mentioned before in Chapter 1, bile acids are an important class of amphiphilic molecules. They are biologically active surfactants that serve a valuable role in the human body as emulsifiers of cholesterol. They also have a unique molecular structure which consists of a concave hydrophilic face and a convex hydrophobic face that leads to aggregation behavior that is different than that of typical surfactants[15]. They are able to aggregate at much lower concentrations into primary micelles that will continue to aggregate into elongated secondary micelles via hydrogen bonding between the outward facing hydrophilic groups[14]. Further study of bile acid aggregation has shown that certain derivatives of bile acids are able to assemble into a wide range of different morphologies including helical fibers[116], ribbons[28], and straight tubes[69] depending on a variety of factors. These can include things such as solution pH, the ionic strength of the solvent, as well as concentration of bile acid. Our current work is solely focused on the self-assembly behavior of LCA. LCA has very low solubility at physiological pH, and therefore the pH of the solvent needs to be increased to alkaline values in order to increase solubility. This increase in solubility is due

to the deprotonation of the carboxyl group from COOH into COO⁻[72]. With an increase in solubility the formation time of LCA tubes is decreased from two months to only a few days. LCA tube formation is indicated by a transition in solution appearance from clear to a milky white which takes place over a time period of 48 hours. In this work we form LCA tubes in 1% w/w NH₄OH solution and study its structure via optical microscopy, SEM, TEM and AFM measurements.

Cyanine dyes are an important class of near-infrared dyes that are composed of two nitrogen containing heterocyclic rings that are joined by a polymethine bridge of varying length[52]. Dyes used in our experiments are cationic dyes and therefore are able to interact with the deprotonated LCA to form H- and J-aggregate coatings on the surface of the preformed LCA tubes. In this work we show a path towards the templated formation of H- and J-aggregates on the surface of preformed nanotubes via the electrostatic interaction. H- and J-aggregate coatings are then characterized via UV-vis absorption spectra, TEM, and electrical measurements using a sourcemeter.

4.2 Experimental

4.2.1 Materials

Lithocholic acid (LCA), NH₄OH solution, 3,3'-diethylthiadicarbocyanine iodide (D25), and 3,3'-dipropylthiadicarbocyanine iodide (D35) were purchased from Sigma Aldrich. All chemicals were used without further purification. Water used in the experiments was purified an Easypure II system (18 MΩ cm, pH 5.7). Silicon wafer and carbon coated copper grids were from Sigma-Aldrich and Electron Microscopy Science, respectively.

4.2.2 Formation of J-aggregate Tube

LCA was added, at a concentration of 3 mM, to aqueous solution containing 1% and 15% NH_4OH at room temperature. The samples were then sonicated for 2-3 minutes at a temperature of 50°C , after which they were stored for 24-48 hours at room temperature to allow for tube growth. Once LCA tube formation had occurred D25 and D35 were added to the tube solution for a final dye concentration of .13 mM per sample. The samples were then stored in the dark to allow for the dye to coat the tubes overnight.

4.2.3 Characterization

The adsorption properties of the J-aggregate tubes were characterized with a Cary 300 UV-vis spectrophotometer. The morphology of the J-aggregate tubes was imaged with a transmission electron microscope (FEW Technai F30 TEM), a scanning electron microscope (Hitachi S3500N SEM), an atomic force microscope (AFM) and an optical microscope (Olympus BX51). For the TEM measurements, tubes were dried on carbon coated copper grids. AFM images of tubes dried on a glass substrate were taken with a Dimension 3100 AFM from Veeco Instruments in air at room temperature. A silicon nitride cantilever (Nanosensors) with a spring constant of 30 N/m and a resonant frequency of 260 kHz was used in tapping mode. The size of the cantilever tips (radius of curvature) was about 15 nm according to the manufacturer. Cyclic voltammetry (CV) measurements were performed in aqueous solution containing 1M KCl using a CS 350 Electrochemical workstation, in which J-aggregate nanotubes were deposited on an ITO working electrode, a platinum wire acted as the counter electrode and Ag/AgCl served as a reference electrode. Current-voltage measurements were performed with a Keithley 2400 sourcemeter.

4.2.4 Fabrication of Interdigitated Gold Electrodes

For the fabrication of interdigitated gold electrodes, a 100 nm thick SiO₂ insulation layer was first grown on a 3-inch Si wafer by thermal oxidation process. A metallic seed layer which consists of 100 nm Au over 10 nm Ti was then deposited on the top of the SiO₂ layer by e-beam evaporation. A thin layer of positive photoresist (Microposit S1813, Dow Electronic Materials) was then spin-coated (3000 rpm, 30 sec), soft-baked (105 °C, 3 min), exposed under I-line UV aligner (8 sec) and developed (Microposit MF CID-26 Developer, 35 sec) to obtain photoresist patterns for interdigitated electrodes with a gap of 50 µm. The developed patterns were hard-baked at 105°C for 10min) and used as a protective layer for subsequent etching steps. The Au/Ti seed layer in exposed areas was chemically etched with an Au etchant (KI and I₂ mixture solution) and a Ti etchant (0.5% HF). The remaining photoresist was dissolved in acetone and the interdigitated electrodes were made ready after cleaning in methanol and deionized water. A schematic representation of this process can be seen in Figure 7.

4.3 Results and Discussion

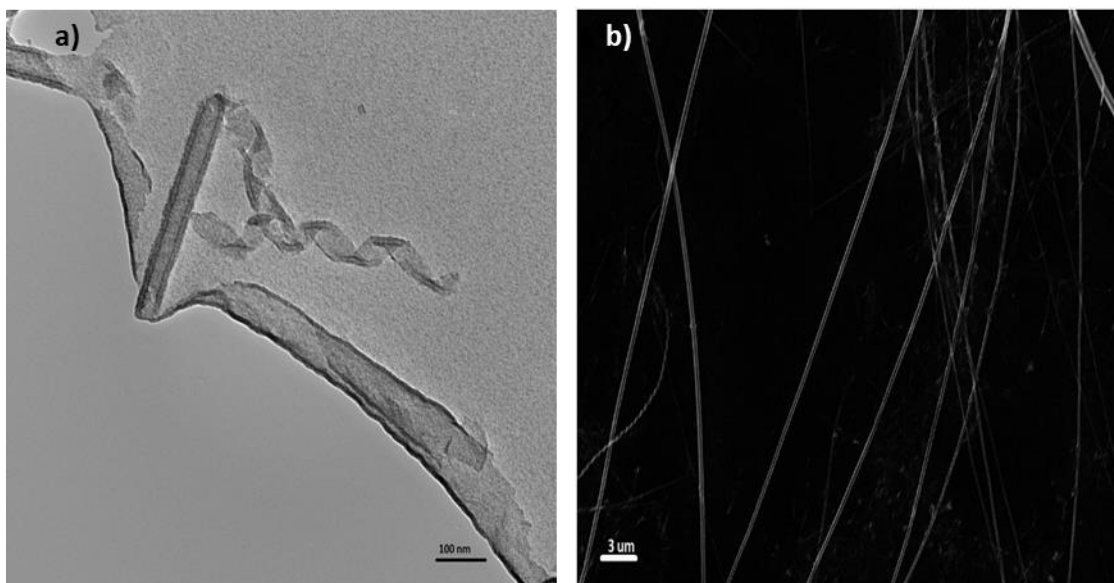


Figure 33 a) TEM and b) SEM of tubes formed in 1% ammonia

LCA dissolved in 1% ammonia solution was observed to form long, straight tubes over a period of 24-48 hours. Figure 33 shows the tubes under a) TEM and b) SEM. The TEM image supplies information on the active formation mechanism in ammonia solution. Previously in our group it had been shown that in NaOH solution, LCA forms small vesicles that linearly aggregate into tubes over time. These tubes formed via small vesicle aggregation were able to switch their morphology from helical to straight as the pH of the solution was changed. In the current case, it is shown that the LCA tubes form via a different mechanism. In ammonia solution, LCA sheet formation takes place initially. Over time these sheets begin to twist and collapse in on themselves to form tubes via a chiral self-assembly process as described in Chapter 1. TEM supplies us with the direct evidence of this, as Figure 33a clearly shows helical ribbon that appears to be collapsing in on itself alongside an already formed LCA tube. The tube walls are clearly visible and appear

to have a thickness of approximately 20 ± 5 nm. The SEM image provided in Figure 33b shows a large number of tubes formed in the solution with an overall thickness on the order of .1-.5 μ m.

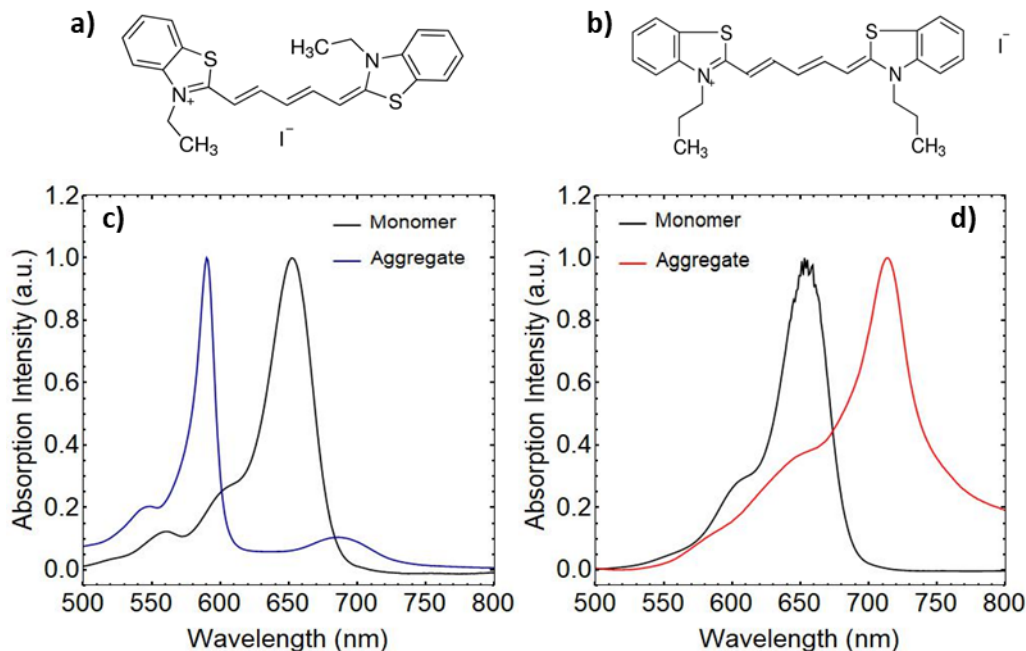


Figure 34 Dye structures of a) D25 and b) D35. UV-vis of aggregates formed by c) D25 coating and d) D35 coating of LCA tubes in 1% ammonia.

Once tube formation had occurred, dye solutions were prepared and the tubes were coated. The solution was left overnight to allow ample time for the coating to form before measurements were carried out. The dye structures for D25 and D35 can be seen in Figure 34a and Figure 34b respectively. The two dyes have a conjugate backbone with the same length, while the length of the two side chains includes one additional carbon bond for D35. This variation in the side chain length will affect how the dye is able to pack on the outside of the LCA tube. The UV-vis absorption spectra for both the dye monomers and aggregates can be seen in Figure 34c (D25) and Figure 34d (D35). All the spectra were normalized to max intensity of 1 for the sake of comparison. For D25, the monomer band appears at 652 nm in a solution of methanol. Once coated on the LCA

tubes, the primary aggregate formed is H-aggregate, with a peak appearing at 590 nm which is blue-shifted from the monomer by 62 nm. There is also a small J-band that forms at 686 nm, with a 34-nm red-shift from the monomer. For D35, the monomer band appears at 653 nm in methanol. Upon coating of the LCA tubes, there is only one peak that forms and that is at 714 nm, which is red-shifted from the monomer by 61 nm which indicates the formation of J-aggregate. Figure 35 shows the LCA tubes with large dark patches that indicate the dye has absorbed onto the surface of the tubes. Of note is that the tube is also surrounded by a large number of dark particles. The dark patches on the tubes also seem to consist of multiple small particles that have adsorbed onto the surface. This would indicate that the coating is formed by the adsorption of small aggregate particles.

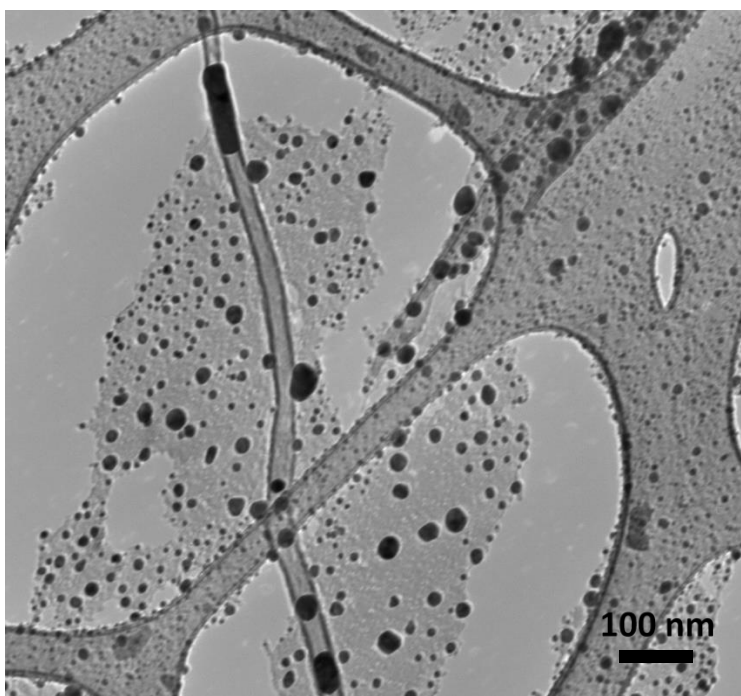


Figure 35 TEM showing patches of dye coating on the surface of LCA tubes during the coating process.

Over time, the J-aggregate formed by D35 remains stable on the surface of the LCA tubes, however the same cannot be said for the H-aggregate formed by D25. This H-aggregate appears to be a metastable state that partially dissociates and then undergoes an aggregation into a J-aggregate configuration with a peak at 701 nm, which can be seen in Figure 36a. Unlike in Chapter 3, where H-aggregate directly slips and transforms into J-aggregate, there is no isosbestic point which indicates that the H-aggregate must be partially dissociating over time. This then free monomer can aggregate into a head-to-tail fashion and form J-aggregate. Another indication that this is the likely formation mechanism of the J-aggregate is that the absorption intensity at 650 nm is nearly 0 on day 1 but fluctuates at non-zero values over the course of the next few days, producing a shoulder on the J-aggregate peak. It never becomes as defined as pure monomer since the share of free molecules to H- or J-aggregated molecules is low. The dissociation of H-aggregate is governed by an inverse power law, while the consequent J-aggregate formation is governed by a power law suggesting that at equilibrium there will always be both H- and J-aggregate for the coating formed by D25 as can be seen in Figure 36b.

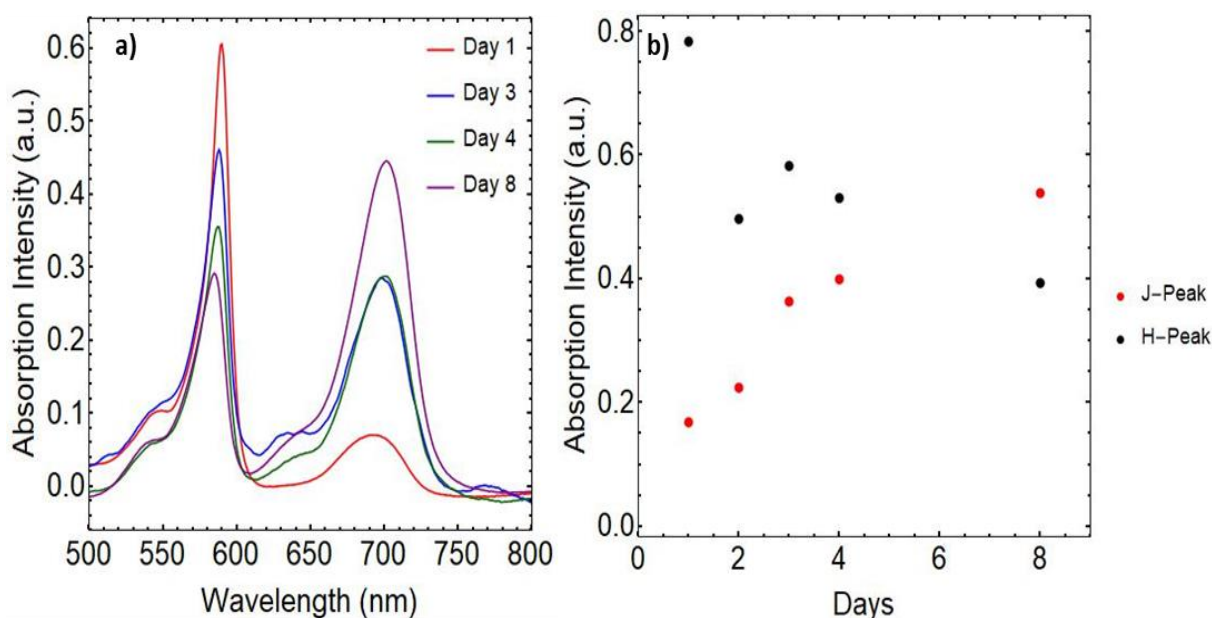


Figure 36 a) Time-dependent UV-vis absorption spectra of the D25 coated LCA tubes showing the transition of the H-aggregate coating into the J-aggregate coating and b) a plot of UV-vis absorption intensity as a function of time showing the gradual decrease of the H-band and increase of the J-band.

The templated H- and J-aggregates were deposited on interdigitated gold electrodes and their IV characteristics were measured. As was the case with the H-aggregate formed via co-assembly in Chapter 3, the D25 H-aggregates also exhibit semiconductor behavior with a threshold voltage of approximately 2.5V as can be seen in Figure 37a. However, once the H- to J- transition begins to occur, the electrical properties become slightly different. The current level under negative bias begins to grow exponentially once a bias voltage of -2V is reached, and dramatically increases between -4V and -5V. Under positive bias, the current increase is not nearly as dramatic as under negative bias, as can be seen in Figure 37b. This data was taken after the solution was aged for 3 days and therefore there was a substantial J-aggregate peak formed. When the dye used forms only J-aggregate, as is the case with the D35 coating, the electrical properties change once more, seen in Figure 37c. The same behavior is seen at negative bias where the current begins to increase at

an exponential rate. However, instead of showing semiconductor behavior under a positive bias, there is a drastically reduced current level as opposed to negative bias. The overall characteristics of the curve seem to be shifting towards a more linear nature. This change in behavior as the aggregation type switches from H- to J-aggregate can be understood in terms of changes of the band gap with respect to the fermi level of the Au electrodes. When the H-aggregate begins to transit into J-aggregate, it results in a reduction in the band gap energy of the dye aggregate. This reduction in the band gap energy will also result in the position of the Au electrode fermi level shifting with respect to the HOMO and LUMO levels of the dye coating. Figure 38a and Figure 38b show CV curves of the D25 H-aggregate coating and the D35 J-aggregate coating respectively. From these curves we can calculate the HOMO/LUMO levels via Equation (6) and Equation (7). We calculate the HOMO level of the H-aggregate coating to be -4.83 eV and the LUMO level to be -2.73 eV. For the J-aggregate coatings the HOMO and LUMO levels are -4.76 and -3.01 eV respectively. Figure 38c shows a schematic representation of the energy levels with respect to the fermi level of Au. The literature shows that with low ammonia adsorption on the surface of Au, the fermi level can be altered, and in this case, end up at -3.25 eV[110]. Due to this difference in the HOMO/LUMO levels between H- and J-aggregates with respect to the fermi level of Au, the IV characteristic behavior will change from being a semiconductor with a symmetric shape to having more linear nature in the middle of the curve. Because the H-aggregate peak never completely disappears there is still some semiconductor behavior observed after the solution is aged a few days. However, when the dye used forms solely a J-aggregate, we no longer observe any symmetric semiconductor IV curve behavior, and instead we shift to slightly more ohmic behavior. Figure 37d shows the coated tubes bridging the gap of the interdigitated Au electrodes.

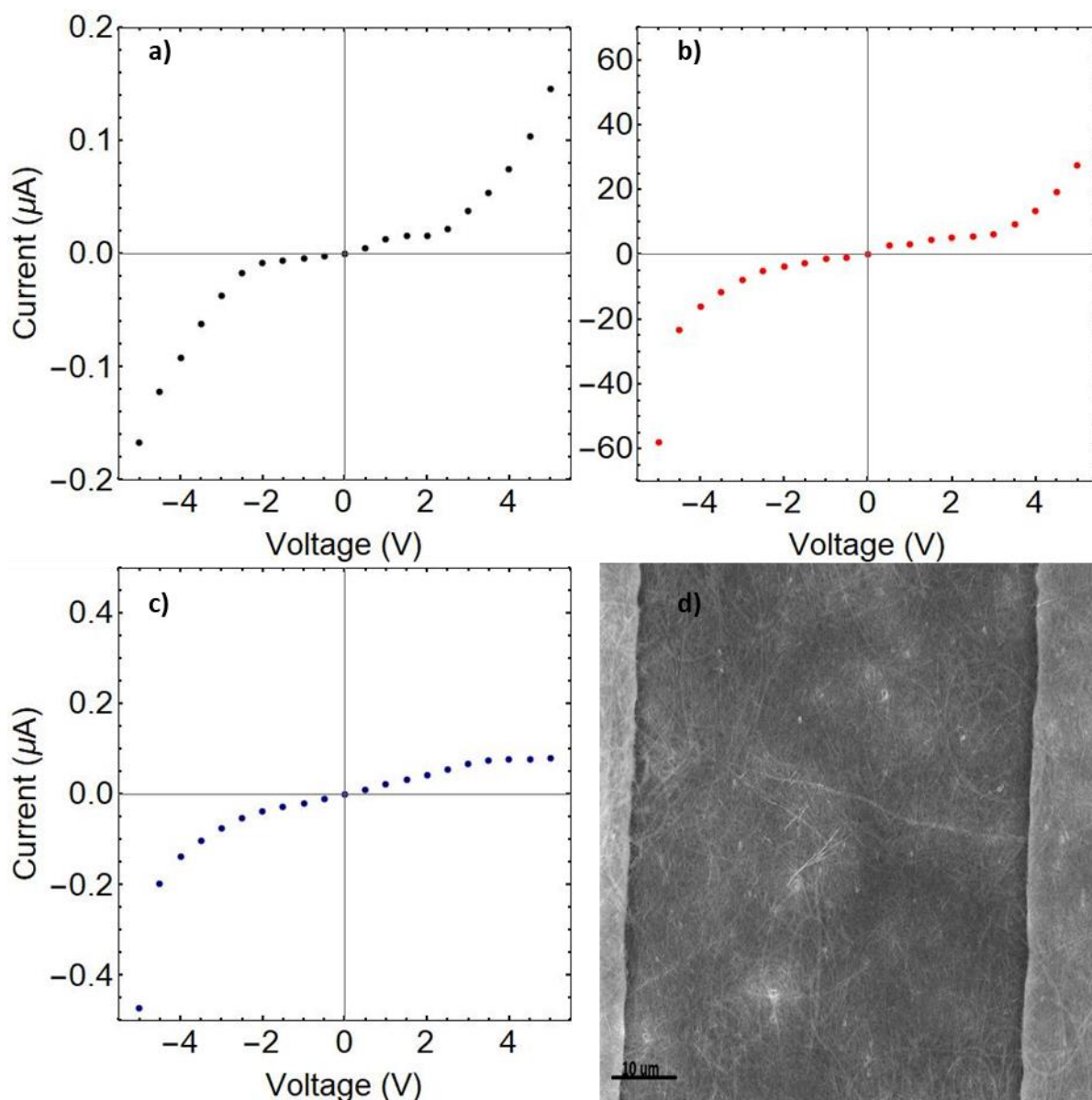


Figure 37 a) IV curve of fresh D25 coated LCA nanotubes, b) IV curve of D25 coated LCA nanotubes that were aged for 3 days, c) IV curve of D35 coated LCA tubes showing the behavior of a pure J-aggregate and d) SEM image of the dye coated LCA nanotubes bridging the interdigitated Au electrodes.

Similar to the co-assembled H- and J-aggregates, both dye coatings respond sensitively to changes in temperature. The IV curves at different temperature can be seen in Figure 39a for D25 and Figure 39b for D35. In both cases there is an appreciable decrease in current level as the

temperature is increased. However, unlike the co-assembled structures formed in Chapter 2 and Chapter 3, there is a different explanation for the reduction of the current level with increasing temperature for the coated LCA tubes. The dye coatings on the LCA tubes consist of a large number of smaller dye aggregates adsorbed onto the surface of the tubes. Once dried on the interdigitated Au electrodes, the coating becomes brittle in nature and therefore as the temperature is increased, the coating can crack and become disjointed at the interfaces between individual patches of dye absorbed on the surface. This cracking and disjointed nature will result in fewer conduction paths as the temperature is increased and therefore the current level should show a drop as temperature of the sample rises.

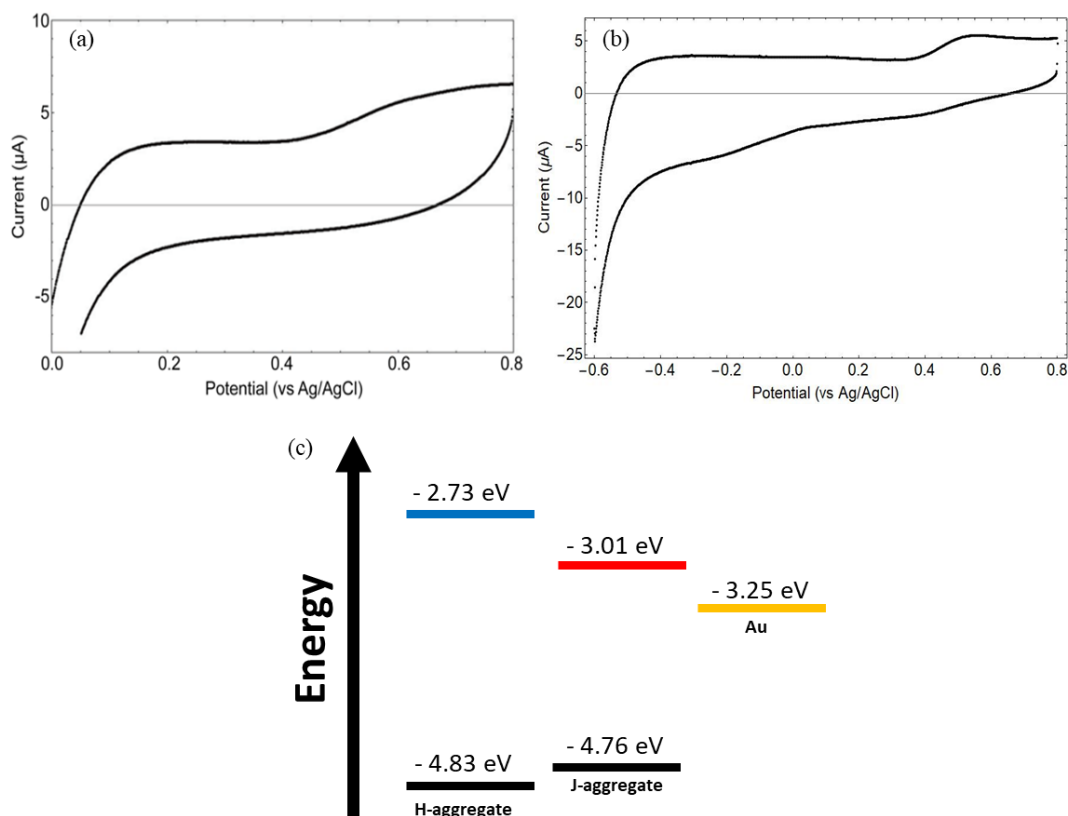


Figure 38 Cyclic curves of a) D25 H-aggregate coated tubes and b) D35 J-aggregate coated tubes. Schematic energy level diagram (c) of the HOMO/LUMO levels of H-aggregate and J-aggregate coatings with respect to the Fermi level of Au electrodes.

One way in which to verify that this is the cause of the current level drop is to examine the absorption spectrum as a function of temperature. The UV-vis absorption spectra as a function of temperature for both the D25 H-aggregate coating and D35 J-aggregate coating can be seen in Figure 40a and Figure 40b, respectively. Unlike the case with the co-assembled structures seen in Chapters 2 and 3, there is no appreciable change in the absorption spectra of the H- and J-aggregate coatings. This indicates that there is no change in the molecular arrangement as the temperature of the aggregates are increased in solution. Thus, the changes as a function of temperature in the IV curves must be the result of physical changes in the quality of the coating as opposed to changes in the molecular packing of the aggregates as the temperature is increased.

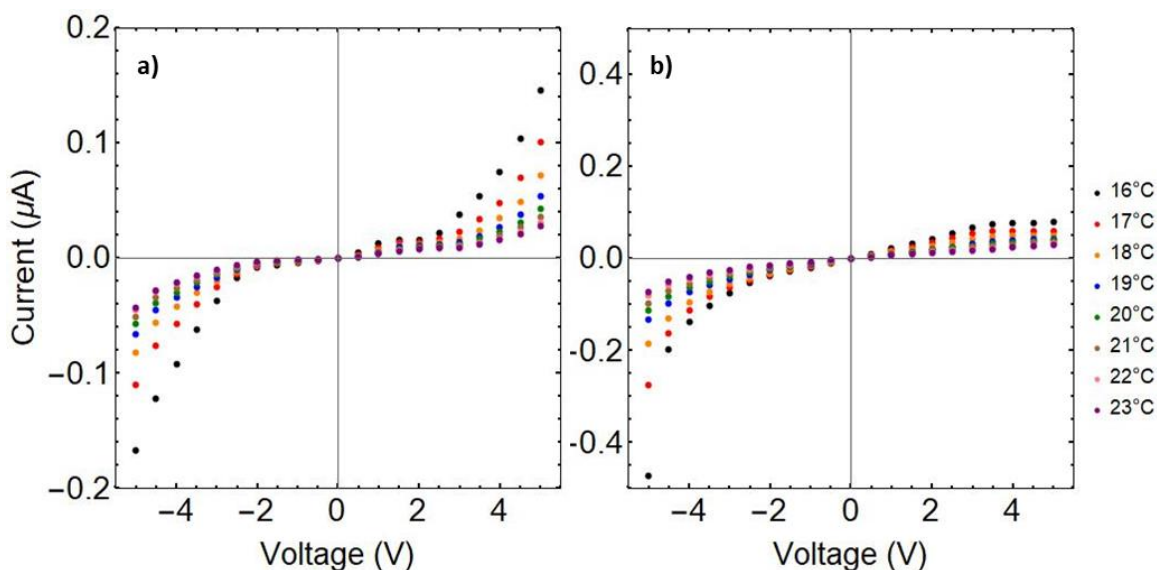


Figure 39 a) IV curves at different temperatures for the D25 coating and b) IV curves at different temperatures for the D35 coating.

4.4 Conclusion

In this chapter we examined the ability of cyanine dyes to coat the surface of preformed LCA tubes in 1% w/w ammonia solution. We found that cyanine dyes D25 and D35 were both able to effectively coat the LCA tubes. For D25, a quasi-stable H-aggregate is formed that transforms over time into a J-aggregate. Plots of UV-vis intensity versus time indicated that over time the system would reach an equilibrium in which both H- and J-aggregates of D25 exist on the surface of the LCA tubes. For D35, a pure J-aggregate is formed that remains stable over time. The IV behavior of the fresh D25 H-aggregate coating shows that it behaves like a semiconductor and as time passes and the H- to J-aggregate transition occurs, the behavior begins to change to show less symmetry in the IV curve. This would indicate a shift in the HOMO and LUMO levels of the D25 H-/J-aggregate coating. For a pure J-aggregate of D35, the IV curve shows highly non-symmetric behavior with much higher current levels under negative bias and a nearly flat IV curve under positive bias. In the next chapter we will utilize these H-/J-aggregate coatings to detect dopamine in pH 10 buffer solution via photo-induced electron transfer.

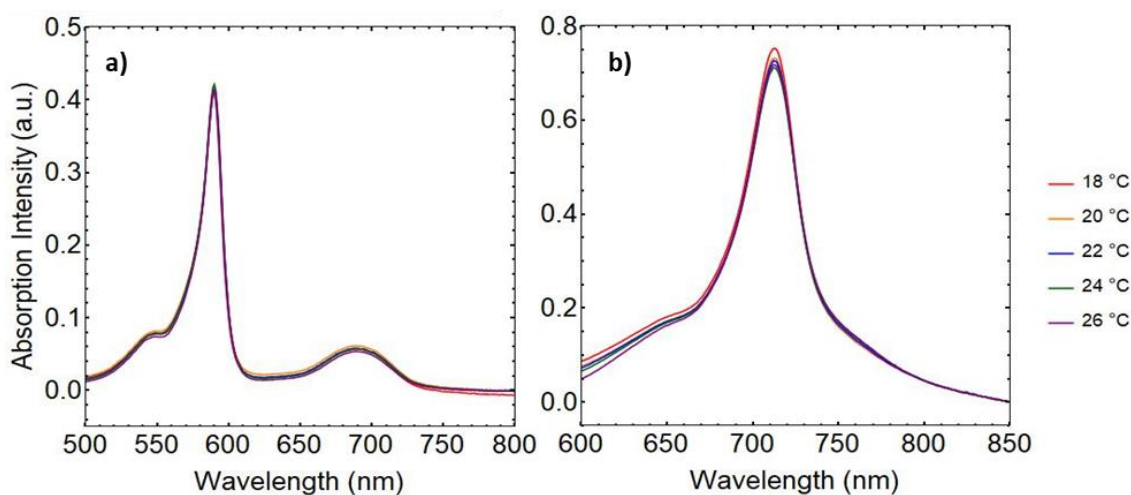


Figure 40 UV-vis absorption spectra at different temperatures for LCA tubes coated with a) D25 and b) D35

CHAPTER 5: TEMPLATED H-/J-AGGREGATE NANOTUBES FOR THE DETECTION OF DOPAMINE

Portions of this chapter were originally published in Rhodes, S.; Wang, X.; Liang, W.; Cho, H.J.; Fang, J.; Templated J-aggregate Nanotubes for the Detection of Dopamine. *J. Mat. Sci. and Chem. Eng.*, **2017**, 5, 142-154.

5.1 Introduction

J-aggregates of dye molecules represent an organized supramolecular structure, in which molecules form a head-to-tail staircase arrangement[39]. The strong interaction of transition dipole moments in J-aggregates leads to new electronic excitations. The new electronic excitations in J-aggregates are coherently delocalized over many molecules rather than confined to individual molecules. The delocalized excitation of J-aggregates leads to an intense absorption band (J-band) and favors for efficient electron transfer. Therefore, they have long been used for mimicking photosynthetic light-harvesting antennas[54, 117-119]. Due to the remarkable optical and transport properties, J-aggregates have also shown great promise in color photography[120], nonlinear optics[121, 122], light emitting diodes[123, 124], and solar cells[125, 126]. However, the application of J-aggregates in biosensors is still limited[78, 127, 128]. This is largely due to the poor stability of J-aggregates in biological fluids, in which the interaction of J-aggregates with proteins and salts may change their structures and consequently optical properties. Recently, efforts have been made in stabilizing J-aggregates by assembling them on lipid vesicles[128], lipid nanotubes[78], DNA helix[129], β -sheet fibrils[130], and peptide nanotubes[131].

J-aggregate nanotubes are attractive for efficient electron transfers because they share the molecular packing feature with photosynthetic light-harvesting antennas[55-57, 60, 61, 96]. In this

paper, we report the formation of templated J-aggregate nanotubes by the adsorption of 3,3'-diethylthiadicarbocyanine iodide (D25) on the self-assembled nanotubes of lithocholic acid (LCA). The optical and electronic properties of the templated J-aggregate nanotubes are investigated with UV-vis absorption spectra, cyclic voltammetry methods and current-voltage measurements. We fabricate a sensor platform by depositing the templated H-/J-aggregate nanotubes on interdigitated gold electrodes for the detection of dopamine (DA). DA is known to be an important neurotransmitter in central and peripheral nervous systems[132]. The concentration level of DA is associated with a series of neural diseases including Parkinson's and Alzheimer's diseases[133]. It is for this reason that DA has long been used as an important biomarker in the diagnosis of neural diseases. Electrochemical methods[134, 135], capillary electrophoresis[136, 137], and liquid chromatography-mass spectrometry[138] are conventional analytical methods for the detection of DA. However, these methods are time consuming and require expensive instruments. The sensitivity of the H-/J-aggregate nanotube-based sensor platform for DA is studied by measuring the photo-induced current change as a function of DA concentrations. We find that the detection limit of the H-/J-aggregate nanotube-based sensor platform for DA is 0.27 nM, which is two orders of magnitude lower than these conventional analytical methods.

5.2 Experimental

5.2.1 Materials

Lithocholic acid (LCA), NH₄OH solution, dopamine (DA), and uric acid (UA) were purchased from Sigma-Aldrich. 3,3'-diethylthiadicarbocyanine iodide (D25) was purchased from Molecular Probes. All chemicals were used without further purification. Water used in the

experiments was purified with Easypure II system (18 M Ω cm, pH 5.7). silicon wafer and carbon coated copper grids were from Sigma-Aldrich and Electron Microscopy Science, respectively.

5.2.2 Formation of Templated H-/J-aggregate Nanotubes

LCA was added into 10% w/w NH₄OH solution in a glass vial to achieve a final concentration of 3 mM, followed by 5 min sonication in an ultrasonic bath (Branson 1510, Branson Ultrasonics Co.) at 50°C. LCA nanotubes were formed when LCA solution was cooled to room temperature. Once LCA nanotubes were formed, 0.13 mM D25 was added. The mixture was incubated overnight for the adsorption of D25 on LCA nanotubes, leading to the formation of templated H-/J-aggregate nanotubes, which were then purified through centrifugation to remove excess D25. The templated H-/J-aggregate nanotubes are stable for weeks in the dark.

5.2.3 Characterization

The morphology of LCA nanotubes and templated H-/J-aggregate nanotubes was studied with a transmission electron microscope (TEM, FEW Technai F30), a scanning electron microscope (SEM, Hitachi S3500N), and an atomic force microscope (AFM, Dimension 3100 Veeco Instruments). For the TEM measurements, nanotubes were dried on carbon coated copper grids. AFM images of nanotubes were dried on carbon coated copper grids. AFM images of nanotubes dried on glass substrates were taken with a silicon nitride cantilever (Nanosensors) with a spring constant of 30 N/m and a resonant frequency of 260 kHz in tapping mode. The optical properties of H-/J-aggregate nanotubes were characterized with a Cary 300 UV-vis spectrophotometer. Cyclic voltammetry (CV) measurements were performed in aqueous solution containing 1M KCl using CS 350 Electrochemical workstation, in which templated J-aggregate nanotubes were deposited on an ITO working electrode, a platinum wire acted as the counter

electrode and Ag/AgCl served as a reference electrode. Current-voltage (I-V) measurements were performed with a Keithley 2400 sourcemeter.

5.2.4 Fabrication of H-/J-aggregate Nanotube-Based Sensor Platform

The interdigitated Au electrodes were cleaned with deionized water before the deposition of templated J-aggregate nanotubes. In our experiments, 4 μL of H-/J-aggregate nanotube solution was dropped on the interdigitated Au electrodes and dried in air at room temperature. The H-/J-aggregate nanotube-based sensor platform was immersed in buffer solution at pH 10 for 1 hour, followed by the addition of DA in the dark. After 30 min incubation, the H-/J-aggregate nanotube-based sensor was irradiated with visible light for 30 seconds, followed by measuring current changes with a sourcemeter.

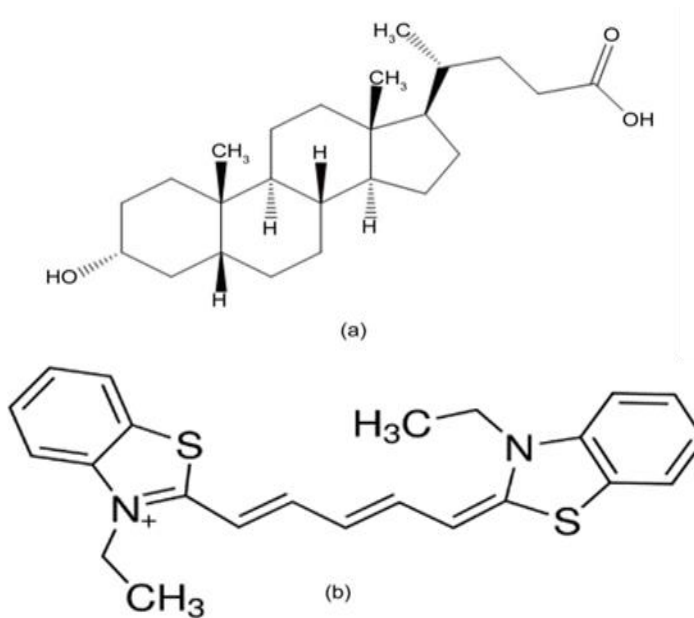


Figure 41 (a) Chemical structure of lithocholic acid and (b) 3,3'-diethylthiadicarbocyanine iodide.

5.3 Results and Discussion

The chemical structures of D25 and LCA are shown in Figure 41a and b, respectively. D25 is a positively charged carbocyanine dye consisting of two nitrogen-containing heterocyclic ring systems, which are linked by a methane bridge. LCA is a secondary bile acid having a nearly planar steroid backbone and a carboxyl group linked to the steroid backbone through a short alkyl chain. It has been shown that negatively charged LCA in alkaline aqueous solution can self-assemble into tubular structures with different diameters and shapes, depending on experimental conditions[27, 29, 68, 70, 71, 139]. Figure 42a is an AFM image of LCA nanotubes formed in NH_4OH solution. The LCA nanotubes show a smooth surface and a uniform diameter along their long axis. The hollowness of the LCA nanotubes is clearly visible in the TEM image shown in Figure 42b. They have an external diameter of ~ 80 nm and a wall thickness of ~ 15 nm. The wall thickness of the LCA nanotubes is larger than the length of the LCA molecule (~ 1.6 nm), suggesting that the wall of the LCA nanotubes has a multi-lamellar structure.

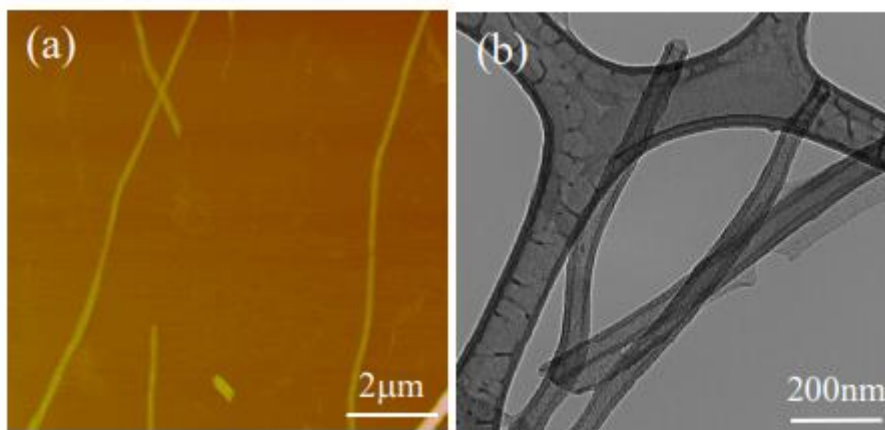


Figure 42(a) AFM of LCA nanotubes dried on glass substrates and (b) TEM images of LCA nanotubes dried on a carbon coated copper grid.

After the adsorption of positively charged D25 through electrostatic interaction, the surface of negatively charged LCA nanotubes becomes rough (Figure 43a). UV-vis absorption spectra show that the D25 molecules adsorbed on LCA nanotubes form J-aggregates (Figure 42b). The templated H-/J-aggregate nanotubes show an intense adsorption band (J-band) at 590 nm. The delocalized excitation length of J-aggregates, which represents the number of coherently coupled molecules (N_{coh}) in the J-aggregates, can be calculated from their absorption spectra according to the Equation (5) [140, 141], where $\Delta\nu_{\text{mon}}$ and $\Delta\nu_{\text{J}}$ are the full widths at the half maxima of monomer and J-aggregate absorption bands, respectively. Thus, we use the Equation (5) to calculate the delocalized excitation length of the templated J-aggregate nanotubes from their absorption spectra to be 22 monomers.

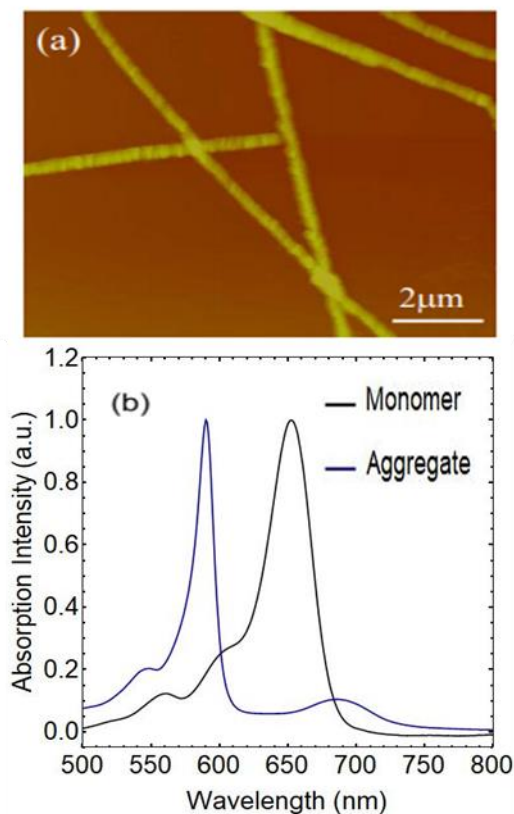


Figure 43 (a) AFM image of templated H-/J-aggregate nanotubes dried on a glass substrate. (b) Absorption spectra of templated H-/J-aggregate nanotubes and D25 monomer in NH_4OH solution.

The templated H-/J-aggregate nanotubes were deposited on the interdigitated Au electrodes with a gap of 20 μm for measuring their electronic properties (Figure 44a). As can be seen in Figure 44b, the templated H-/J-aggregate nanotubes form a network bridging the interdigitated Au electrodes. Individual H-/J-aggregate nanotubes without metallic coating are visible in the SEM

image shown in Figure 44c. The formation of H-/J-aggregate nanotube networks on interdigitated Au electrodes provides a large number of conductive paths for the connection of external circuits.

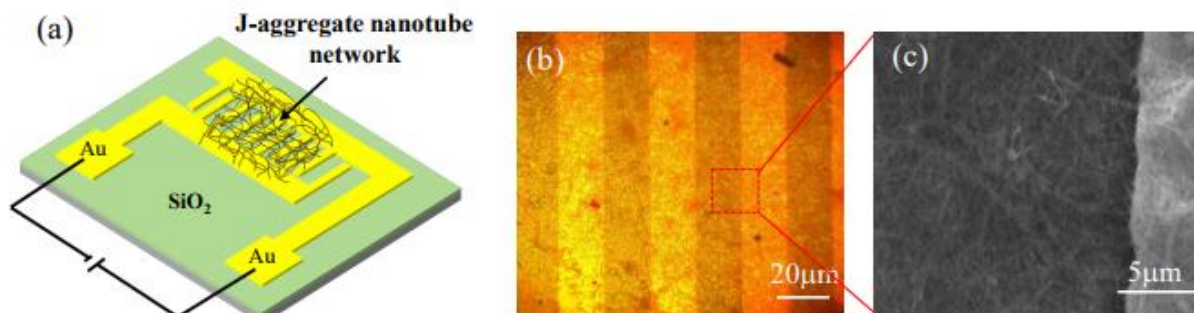


Figure 44 (a) Schematic of J-aggregate nanotube-based sensor platform. (b) Optical microscopy and (c) SEM images of interdigitated Au electrodes with deposited J-aggregate nanotube networks.

Figure 45 shows the current-voltage (I-V) curves of H-/J-aggregate nanotube networks in the applied voltage from -5V to +5V. These I-V curves are symmetrical. There is no change in the I-V curve observed when the H-/J-aggregate nanotube network is exposed to visible light irradiation (Figure 45). We note that the H-/J-aggregate nanotube networks deposited on the interdigitated Au electrodes with the gap of $20\mu\text{m}$ are stable in buffer solution over time and during multiple measurements. However, when the gap of interdigitated Au electrodes reduces to $8\mu\text{m}$, the deposited H-/J-aggregate nanotube networks become unstable after being immersed in buffer solution. This result suggests that the contact of H-/J-aggregate nanotubes with the SiO_2 layer plays an important role for immobilizing them on the interdigitated Au electrodes.

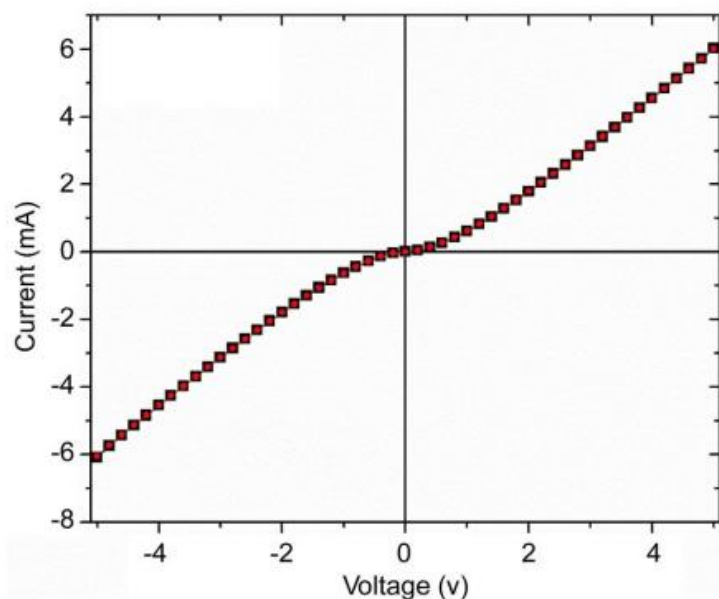


Figure 45 I-V curves of H-/J-aggregate nanotube-based sensors with (circle) and without (square) visible light irradiation.

We exploit the application of the H-/J-aggregate nanotube network deposited on the interdigitated Au electrodes with the gap of 20 μm as a sensor platform for the detection of DA in alkaline buffer solution. It has been shown that DA has pH-dependent oxidation and reduction potentials (Figure 46)[142]. In alkaline buffer solution, DA is easily oxidized into quinone by oxygen. DA-quinone is an electron acceptor[143]. In our experiments, the H-/J-aggregate nanotube based sensor platform was immersed in 50 mL buffer solution at pH 10, followed by the addition of DA in the dark. It has been shown that DA is able to adsorb on a variety of organic surfaces through strong intermolecular interactions including hydrogen-bonding, π - π interaction, and metal chelation[144]. The H-/J-aggregate nanotubes are stable in the buffer solution at pH 10. There is no adsorption spectrum change observed. After 30 min incubation at room temperature for the oxidization and adsorption of DA on the H-/J-aggregate nanotube networks, the H-/J-aggregate nanotube-based sensor was irradiated with visible light for 30 seconds, followed by

measuring the current change under the forward voltage at 5V. To avoid sensor-to-sensor variations, we used the normalized current change $\Delta I/I_0$ to represent the current response of H-/J-aggregate nanotube-based sensors to DA, where ΔI is $I_0 - I$, I_0 is the current without DA, and I is the current with DA. As can be seen in Figure 8, the normalized current change of H-/J-aggregate nanotube based sensors after the addition of 20 nM DA at the forward voltage of 5V with visible light irradiation is much higher than that without light irradiation. Thus, we infer that the current change of the H-/J-aggregate nanotube-based sensor in response to DA under visible light irradiation is a result of the photoinduced electron transfer (PET) from the excited H-/J-aggregate nanotubes to the adsorbed Da-quinone (see the schematic insert in Figure 47).

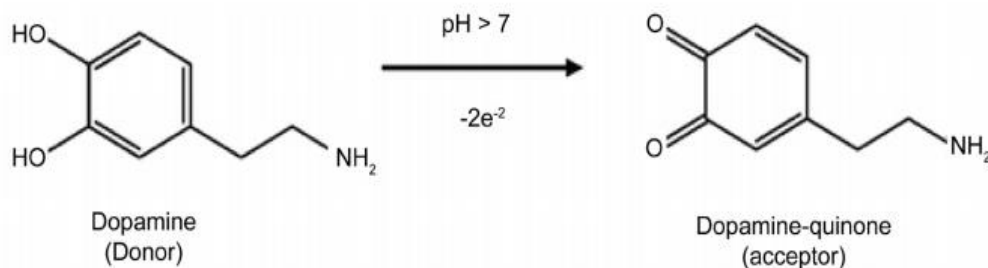


Figure 46 Schematic illustration of the oxidization of DA induced by pH values.

It is known that the relative HOMO and the LUMO levels between a donor and an acceptor determines the electron transfer. Cyclic voltammetry (CV) measurements show the irreversible oxidation of the templated H-/J-aggregate nanotubes immobilized on ITO in aqueous solution containing 1M KNO₃ (Figure 48). The templated H-/J-aggregate nanotubes are oxidized at the positive potential of +0.43V with no corresponding reduction peak. The highest occupied molecular orbital (HOMO) and the lowest unoccupied molecular orbital (LUMO) levels of H-/J-aggregate nanotubes can be calculated with Equation (6) and Equation (7) (6)[109], where E_{onset} is .43V and E_g is the optical band gap energy which can be calculated according to the

equation[145]: $E_g = 1242/\lambda_{\text{onset}}$. For the templated H-/J-aggregate nanotubes, λ_{onset} is 590 nm. Thus, E_g is calculated to be 2.10 eV. Using the empirical equations, we find that the E(HOMO) and E(LUMO) level of the templated H-/J-aggregate nanotubes is -4.83 eV and -2.73 eV, respectively. The LUMO level of DA-quinone is -3.85 eV [146], which is inside the HOMO-LUMO energy gap of the templated J-aggregate nanotubes, favoring the electron transfer from the excited H-/J-aggregate nanotube to the adsorbed DA-quinone.

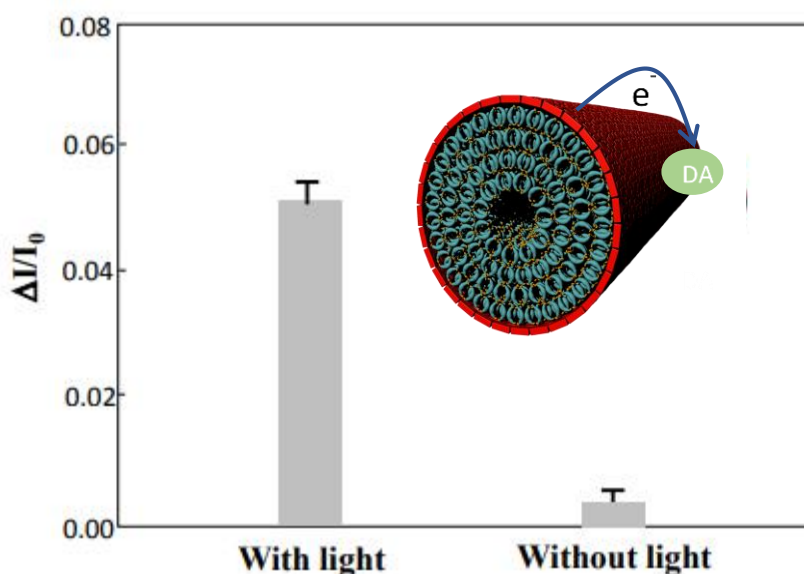


Figure 47 Current change of H-/J-aggregate nanotube-based sensor platform in response to 20 nM DA in buffer solution at pH 10 with and without 30s visible light irradiation. Schematic of photoinduced electron transfer (PET) from the templated H-/J-aggregate nanotube to the adsorbed DA is insert in figure.

The current change due to the PET from the excited H-/J-aggregate nanotubes to the adsorbed DA-quinone provides a basis for the detection of DA. Figure 49a shows a plot of $\Delta I/I_0$ as a function of DA concentration in buffer solution at pH 10. The plot can be fitted linearly with a correlation coefficient of 0.9748 in the concentration range from 10 nM to 70 nM, which falls within the concentration level of DA for patients with Parkinson's disease[147].

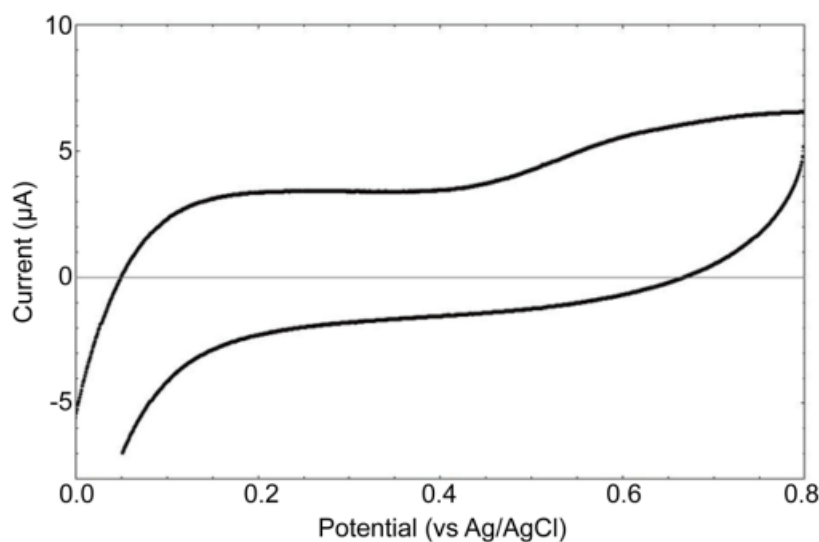


Figure 48 Cyclic voltammogram of H-/J-aggregate nanotubes immobilized on ITO in aqueous solution containing 1M KCL. Scan rate: 0.1 v/s

The detection limit of H-/J-aggregate nanotube sensors for DA is calculated by multiplying the ratio of the standard deviation to the slope of the linear fit curve by 3.3 to be ~0.27 nM. The detection of DA is often complicated by the presence of uric acid (UA), which coexists with DA in vivo at a concentration of 100-1000 times higher than DA[148]. We find that the current response of the H-/J-aggregate nanotube-based sensors for DA is significantly higher than that for UA even when the concentration of UA is 1000 times higher than DA (Figure 49b). The selectivity of H-/J-aggregate nanotube-based sensors for DA should associate with its high affinity to the H-/J-aggregate nanotubes and the efficient electron transfer between them.

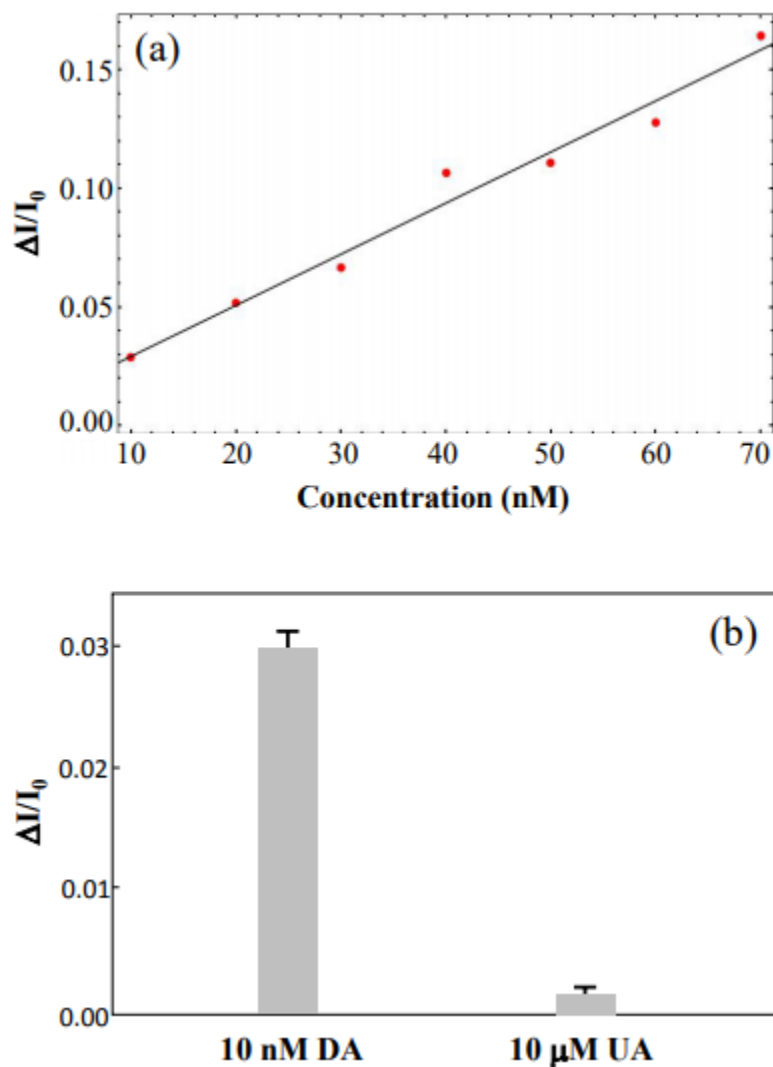


Figure 49(a) Current changes of H-/J-aggregate nanotube-based sensor platform as a function of DA concentrations in buffer solution at pH 10 with 30s visible light irradiation. (b) Current changes of H-/J-aggregate nanotube-based sensor platform in response to 10 nM DA and 10 μM UA in buffer solution at pH 10 with 30s visible light irradiation.

5.4 Conclusion

We have shown that the adsorption of D25 on self-assembled LCA nanotubes can lead to the formation of H-/J-aggregate nanotubes. The templated H-/J-aggregate nanotubes show an intense J-band at 590 nm, which is red-shifted with respect to the adsorption band of D25 monomer

at 550 nm. A sensor platform is fabricated by forming the network of the templated H-/J-aggregate nanotubes on interdigitated Au electrodes for the sensitive and selective detection of DA. The J-aggregate nanotube networks provide a high density of H-/J-aggregate nanotubes for the accessibility of DA and a large number of conductive paths to external circuits. The photo-induced electron transfer from the H-/J-aggregate nanotubes to the adsorbed DA leads to the current change of the H-/J-aggregate nanotube-based sensor, which serves as the basis for the detection of DA. We find that the current change of the H-/J-aggregate nanotube-based sensor in response to DA is linear in the concentration range from 10 nM to 70 nM with the detection limit of 0.27 nM, which is significantly lower than that of conventional analytical methods reported in the literature. The high sensitivity is a result of efficient photo-induced electron transfer from the H-/J-aggregate nanotubes to DA. The H-/J-aggregate nanotube-based sensors are portable and open up an important avenue for the label-free and sensitive detection of DA.

CHAPTER 6: CONCLUSION

In this dissertation we have examined the formation of J- and H-aggregates via the co-assembly of cyanine dyes and LCA. We found that at low ammonia concentration we are able to form spherulitic J-aggregates. These spherulites are the result of the low solubility of cyanine dye in 1% w/w ammonia concentration. The dye aggregates into particles that get slowly broken down by LCA. As LCA breaks down these aggregate particles, it forms a fiber structure with the cyanine dye arranging itself into a J-aggregate within the hydrophobic cavity of the LCA micelles. Over time the dye particles are completely broken down and a spherulite structure remains with J-aggregate fibers radiating out from the center. These spherulites can be broken down into individual fibers without destroying the dye aggregation within the fibers. They can also be dried on an interdigitated electrode and exhibit semiconductor behavior that is highly sensitive to variations in temperature. The current at low temperatures is at a much higher level than when measured at high temperatures. This variation in current level with temperature is due to the packing of the dye molecules in the fiber being changed as temperature increases. UV-vis absorption measurements showed that as temperature increases the number of molecules coherently coupled within the fibers decreases, verifying that temperature changes can alter the number of coupled molecules in the fibers.

When we take the same cyanine dye and dissolve it in different concentrations of ammonia we can alter the type of aggregation that takes place. When the mix ratio of LCA:dye remains constant at 5:1, J-aggregate is formed until the ammonia concentration reaches 15% w/w. At this point and beyond an H-aggregate appears and forms differently than the spherulites described above. In this case the dye and LCA couple in solution and aggregate together to form H-aggregate

fibers. If we increase the mix ratio from 5:1 to 1:1 at high ammonia concentrations we observe and even further shifted H-band. This band appears very broad in the UV-vis absorption spectrum and under the optical microscope appears brown in color while the H-aggregates formed at a mix ratio of 5:1 appear purple in color. At a mix ratio of 1:1 the H-aggregate rods formed show an interesting property upon the evaporation of ammonia counter ions. As the ammonia counterions evaporate out, the co-assembled rods split at the ends and eventually breakdown into a bunch of fibers that are pink in color. These fibers have a sharp J-band in the absorption spectra. It is believed that initially J-aggregate fibers are formed and these fibers bundle into rods. LCA has a negative charge in alkaline solution so the ammonia counterions screen that charge allowing for the formation of bundles. These individual J-aggregate fibers will exhibit H-type coupling with their neighboring fibers and therefore change color in the bundled rod, as well as exhibit a very broad H-band in the UV-vis absorption spectrum. This H- to J-aggregate transition is semi-reversible in nature. The H-aggregate formed in 5:1 and the J-aggregate formed via ammonia evaporation of the 1:1 mix ratio sample exhibit different electronic properties. The H-aggregate is a semiconductor while the J-aggregate is a conductor and this can be explained by the fact that the LUMO of the J-aggregate is closer to the Fermi level of Au than the H-aggregate. In order for current to flow through the H-aggregate fibers a threshold voltage needs to be achieved, therefore classifying it as a semiconductor.

H- and J-aggregates of cyanine dyes can also form via a two-step assembly process. In this case there is a preformed structure that can be coated by the dye. In our experiments we formed LCA nanotubes in ammonia solution and coated the tubes with cyanine dyes of similar conjugated length but different side chain lengths. We found that the dye with the shorter side chain length (D25) first forms a quasi-stable H-aggregate on the surface of the LCA tube while the longer side

chain dye (D35) forms a pure J-aggregate that is stable over time. As the transition between the quasi-stable H-aggregate and stable J-aggregate of the D25 coating occurs, the coating exhibits different electronic behavior. Early in the transition process when there is more H-aggregate than J-aggregate the D25 coating exhibits pure semiconductor behavior. However, as more J-aggregate appears the IV curve becomes less symmetric. When we examine the IV curve of the D35 coating we see that there is no symmetry under negative and positive bias with much larger current levels attained under negative bias. This again is due to the position of the LUMO level with respect to the fermi level of the Au electrodes. At first the H-aggregate has a large band gap with the fermi level of Au position in between the HOMO and LUMO levels. As the H- to J-aggregate transition occurs, this band gap is reduced due to the peak absorption wavelength shifting to longer wavelengths. This will alter the position of the Au fermi level with respect to the LUMO level of the D25 J-aggregate and cause a shift in the IV characteristic behavior. When a dye (D35) that forms pure J-aggregate is used, we see a complete flattening out of the IV curve under positive bias while large current levels are maintained under negative bias. Finally, we utilized the D25 coating as a sensor platform for the detection of dopamine-quinone in pH 10 buffer. We find that it is able to sensitively detect dopamine with a detection limit of .27 nM. This successful application of the D25 coating shows the promise of these molecular dye aggregates being used in further biosensor development.

The control of the morphology and size of cyanine dye aggregates has been notoriously difficult without expensive and time-consuming chemical engineering. By developing and investigating these simple methods for the controlled aggregation of cyanine dyes this dissertation has shown a way forward for the potential development of optoelectronic devices that utilize H- and J-aggregates. Future work in this area would involve a more detailed study of the coating

behavior of cyanine dyes on LCA tubes and how counterion concentration can affect the aggregation type of different categories of cyanine dyes.

REFERENCES

- [1] R. N. Redinger, "The Role of the Enterohepatic Circulation of Bile Salts and Nuclear Hormone Receptors in the Regulation of Cholesterol Homeostasis: Bile Salts as Ligands for Nuclear Hormone Receptors," *Canadian Journal of Gastroenterology*, vol. 17, no. 4, 2003.
- [2] A. F. Hofmann, "Bile Acids: The Good, the Bad, and the Ugly," *Physiology*, vol. 14, no. 1, pp. 24-29, 1999.
- [3] W. A. Alrefai and R. K. Gill, "Bile Acid Transporters: Structure, Function, Regulation and Pathophysiological Implications," *Pharmaceutical Research*, journal article vol. 24, no. 10, pp. 1803-1823, October 01 2007.
- [4] S. M. Houten, M. Watanabe, and J. Auwerx, "Endocrine functions of bile acids," *The EMBO Journal*, 10.1038/sj.emboj.7601049 vol. 25, no. 7, p. 1419, 2006.
- [5] T. Li and J. Y. L. Chiang, "Bile Acid Signaling in Metabolic Disease and Drug Therapy," *Pharmacological Reviews*, vol. 66, no. 4, pp. 948-983, 2014.
- [6] P. B. Hylemon, H. Zhou, W. M. Pandak, S. Ren, G. Gil, and P. Dent, "Bile acids as regulatory molecules," *Journal of Lipid Research*, vol. 50, no. 8, pp. 1509-1520, August 1, 2009 2009.
- [7] S. E. McGarr, J. M. Ridlon, and P. B. Hylemon, "Diet, anaerobic bacterial metabolism, and colon cancer: a review of the literature," *Journal of clinical gastroenterology*, vol. 39, no. 2, pp. 98-109, 2005.
- [8] C. Chatgililoglu and V. Snieckus, *Chemical synthesis: gnosis to prognosis*. Springer Science & Business Media, 2012.

- [9] W. Curatolo, "The physical properties of glycolipids," *Biochimica et Biophysica Acta (BBA)-Reviews on Biomembranes*, vol. 906, no. 2, pp. 111-136, 1987.
- [10] W. Curatolo, "Glycolipid function," *Biochimica et Biophysica Acta (BBA)-Reviews on Biomembranes*, vol. 906, no. 2, pp. 137-160, 1987.
- [11] D. Lombardo, M. A. Kiselev, S. Magazù, and P. Calandra, "Amphiphiles self-assembly: basic concepts and future perspectives of supramolecular approaches," *Advances in Condensed Matter Physics*, vol. 2015, 2015.
- [12] M. Salim, H. Minamikawa, A. Sugimura, and R. Hashim, "Amphiphilic designer nano-carriers for controlled release: from drug delivery to diagnostics," *MedChemComm*, 10.1039/C4MD00085D vol. 5, no. 11, pp. 1602-1618, 2014.
- [13] J. Israelachvili, "Thermodynamic and Geometric Aspects of Amphiphile Aggregation into Micelles, Vesicles and Bilayers, and the Interactions between them," *Proc. Int. School Phys. Enrico Fermi Course XC*, 1985.
- [14] L. B. Pártay, M. Sega, and P. Jedlovsky, "Morphology of Bile Salt Micelles as Studied by Computer Simulation Methods," *Langmuir*, vol. 23, no. 24, pp. 12322-12328, 2007/11/01 2007.
- [15] D. Small, P. Nair, and D. Kritchevsky, "The bile acids: chemistry, physiology and metabolism," *P. P. Nair, D. Kritchevsky (Eds.)*, vol. 1, pp. 249-356, 1971.
- [16] T. Shimizu, M. Masuda, and H. Minamikawa, "Supramolecular nanotube architectures based on amphiphilic molecules," *Chemical Reviews*, vol. 105, no. 4, pp. 1401-1444, 2005.
- [17] D. S. Chung, G. B. Benedek, F. M. Konikoff, and J. M. Donovan, "Elastic free energy of anisotropic helical ribbons as metastable intermediates in the crystallization of

- cholesterol," *Proceedings of the National Academy of Sciences*, vol. 90, no. 23, pp. 11341-11345, 1993.
- [18] N. Nakashima, S. Asakuma, and T. Kunitake, "Optical microscopic study of helical superstructures of chiral bilayer membranes," *Journal of the American Chemical Society*, vol. 107, no. 2, pp. 509-510, 1985.
- [19] D. A. Frankel and D. F. O'Brien, "Supramolecular assemblies of diacetylenic aldonamides," *Journal of the American Chemical Society*, vol. 116, no. 22, pp. 10057-10069, 1994.
- [20] J. H. Fuhrhop and W. Helfrich, "Fluid and solid fibers made of lipid molecular bilayers," *Chemical reviews*, vol. 93, no. 4, pp. 1565-1582, 1993.
- [21] G. John, M. Mason, P. M. Ajayan, and J. S. Dordick, "Lipid-based nanotubes as functional architectures with embedded fluorescence and recognition capabilities," *Journal of the American Chemical Society*, vol. 126, no. 46, pp. 15012-15013, 2004.
- [22] T. Imae, Y. Takahashi, and H. Muramatsu, "Formation of fibrous molecular assemblies by amino acid surfactants in water," *Journal of the American Chemical Society*, vol. 114, no. 9, pp. 3414-3419, 1992.
- [23] J. Song, Q. Cheng, S. Kopta, and R. C. Stevens, "Modulating artificial membrane morphology: pH-induced chromatic transition and nanostructural transformation of a bolaamphiphilic conjugated polymer from blue helical ribbons to red nanofibers," *Journal of the American Chemical Society*, vol. 123, no. 14, pp. 3205-3213, 2001.
- [24] C. Zhan, P. Gao, and M. Liu, "Self-assembled helical spherical-nanotubes from an L-glutamic acid based bolaamphiphilic low molecular mass organogelator," *Chemical communications*, no. 4, pp. 462-464, 2005.

- [25] E. Rogalska, M. Rogalski, T. Gulik-Krzywicki, A. Gulik, and C. Chipot, "Self-assembly of chlorophenols in water," *Proceedings of the National Academy of Sciences*, vol. 96, no. 12, pp. 6577-6580, 1999.
- [26] H. Yanagawa, Y. Ogawa, H. Furuta, and K. Tsuno, "Spontaneous formation of superhelical strands," *Journal of the American Chemical Society*, vol. 111, no. 13, pp. 4567-4570, 1989.
- [27] P. Terech and Y. Talmon, "Aqueous suspensions of steroid nanotubules: Structural and rheological characterizations," *Langmuir*, vol. 18, no. 19, pp. 7240-7244, 2002.
- [28] Y. V. Zastavker *et al.*, "Self-assembly of helical ribbons," *Proceedings of the National Academy of Sciences*, vol. 96, no. 14, pp. 7883-7887, 1999.
- [29] X. Zhang, J. Zou, K. Tamhane, F. F. Kobzeff, and J. Fang, "Self-Assembly of pH-Switchable Spiral Tubes: Supramolecular Chemical Springs," *Small*, vol. 6, no. 2, pp. 217-220, 2010.
- [30] Y. Yamamoto *et al.*, "Efficient light harvesting via sequential two-step energy accumulation using a Ru–Re5 multinuclear complex incorporated into periodic mesoporous organosilica," *Chemical Science*, vol. 5, no. 2, pp. 639-648, 2014.
- [31] M. W. Logan, S. Ayad, J. D. Adamson, T. Dilbeck, K. Hanson, and F. J. Uribe-Romo, "Systematic variation of the optical bandgap in titanium based isorecticular metal–organic frameworks for photocatalytic reduction of CO₂ under blue light," *Journal of Materials Chemistry A*, vol. 5, no. 23, pp. 11854-11863, 2017.
- [32] A. J. Bard and M. A. Fox, "Artificial photosynthesis: solar splitting of water to hydrogen and oxygen," *Accounts of Chemical Research*, vol. 28, no. 3, pp. 141-145, 1995.

- [33] D. Gust, T. A. Moore, and A. L. Moore, "Solar fuels via artificial photosynthesis," *Accounts of chemical research*, vol. 42, no. 12, pp. 1890-1898, 2009.
- [34] S. Ganapathy *et al.*, "Alternating syn-anti bacteriochlorophylls form concentric helical nanotubes in chlorosomes," *Proceedings of the National Academy of Sciences*, vol. 106, no. 21, pp. 8525-8530, 2009.
- [35] R. Cogdell, T. Howard, N. Isaacs, K. McLuskey, and A. Gardiner, "Structural factors which control the position of the Qy absorption band of bacteriochlorophyll a in purple bacterial antenna complexes," *Photosynthesis research*, vol. 74, no. 2, pp. 135-141, 2002.
- [36] G. T. Oostergetel, M. Reus, A. Gomez Maqueo Chew, D. A. Bryant, E. J. Boekema, and A. R. Holzwarth, "Long-range organization of bacteriochlorophyll in chlorosomes of *Chlorobium tepidum* investigated by cryo-electron microscopy," *FEBS letters*, vol. 581, no. 28, pp. 5435-5439, 2007.
- [37] J. Dostál, J. Pšenčík, and D. Zigmantas, "In situ mapping of the energy flow through the entire photosynthetic apparatus," *Nature Chemistry*, Article vol. 8, p. 705, 05/30/online 2016.
- [38] G. Scheibe, "Variability of the absorption spectra of some sensitizing dyes and its cause.," *Angewandte Chemie International Edition*, vol. 49, p. 563, 1936.
- [39] E. E. Jelley, "Molecular, Nematic and Crystal States of I: I-Diethyl--Cyanine Chloride," *Nature*, vol. 139, p. 631, 04/10/online 1937.
- [40] E. E. Jelley, "Spectral absorption and fluorescence of dyes in the molecular state," *Nature*, vol. 138, no. 3502, pp. 1009-1010, 1936.

- [41] G. Scheibe, "Über die Veränderlichkeit der Absorptionsspektren in Lösungen und die Nebenvalezen als ihre Ursache," *Angewandte Chemie*, vol. 50, no. 11, pp. 212-219, 1937.
- [42] A. Eisfeld and J. Briggs, "The J-and H-bands of organic dye aggregates," *Chemical Physics*, vol. 324, no. 2, pp. 376-384, 2006.
- [43] F. Würthner, T. E. Kaiser, and C. R. Saha-Möller, "J-Aggregates: From Serendipitous Discovery to Supramolecular Engineering of Functional Dye Materials," *Angewandte Chemie International Edition*, vol. 50, no. 15, pp. 3376-3410, 2011.
- [44] G. Pescitelli, L. Di Bari, and N. Berova, "Application of electronic circular dichroism in the study of supramolecular systems," *Chemical Society Reviews*, vol. 43, no. 15, pp. 5211-5233, 2014.
- [45] J. Frenkel, "On the Transformation of light into Heat in Solids. I," *Physical Review*, vol. 37, no. 1, pp. 17-44, 01/01/ 1931.
- [46] E. A. Bloemsma, *Exciton localization and optical spectroscopy of linear and tubular J-aggregates*. University of Groningen Library][Host], 2013.
- [47] V. M. Agranovich and G. C. La Rocca, *Organic nanostructures: science and applications*. IOS Press, 2002.
- [48] J. Knoester, "Modeling the optical properties of excitons in linear and tubular J-aggregates," *International Journal of Photoenergy*, vol. 2006, 2006.
- [49] C. t. l. Didraga, J. A. Klugkist, and J. Knoester, "Optical properties of helical cylindrical molecular aggregates: the homogeneous limit," *The Journal of Physical Chemistry B*, vol. 106, no. 44, pp. 11474-11486, 2002.

- [50] D. r. M. Eisele *et al.*, "Photoinitiated growth of sub-7 nm silver nanowires within a chemically active organic nanotubular template," *Journal of the American Chemical Society*, vol. 132, no. 7, pp. 2104-2105, 2010.
- [51] J. R. Tischler, M. S. Bradley, Q. Zhang, T. Atay, A. Nurmikko, and V. Bulović, "Solid state cavity QED: Strong coupling in organic thin films," *Organic Electronics*, vol. 8, no. 2, pp. 94-113, 2007.
- [52] A. Mishra, R. K. Behera, P. K. Behera, B. K. Mishra, and G. B. Behera, "Cyanines during the 1990s: A Review," *Chemical Reviews*, vol. 100, no. 6, pp. 1973-2012, 2000/06/01 2000.
- [53] F. Würthner, T. E. Kaiser, and C. R. Saha-Möller, "J-Aggregates: From Serendipitous Discovery to Supramolecular Engineering of Functional Dye Materials," *Angewandte Chemie International Edition*, vol. 50, no. 15, pp. 3376-3410, 2011.
- [54] T. S. Balaban, "Tailoring Porphyrins and Chlorins for Self-Assembly in Biomimetic Artificial Antenna Systems," *Accounts of Chemical Research*, vol. 38, no. 8, pp. 612-623, 2005/08/01 2005.
- [55] H. von Berlepsch, C. Böttcher, A. Ouart, C. Burger, S. Dähne, and S. Kirstein, "Supramolecular Structures of J-Aggregates of Carbocyanine Dyes in Solution," *The Journal of Physical Chemistry B*, vol. 104, no. 22, pp. 5255-5262, 2000/06/01 2000.
- [56] E. Lang, A. Sorokin, M. Drechsler, Y. V. Malyukin, and J. Köhler, "Optical spectroscopy on individual amphi-PIC J-aggregates," (in eng), *Nano letters*, vol. 5, no. 12, pp. 2635-2640, 2005/12// 2005.

- [57] N. Kameta, K. Ishikawa, M. Masuda, M. Asakawa, and T. Shimizu, "Soft Nanotubes Acting as a Light-Harvesting Antenna System," *Chemistry of Materials*, vol. 24, no. 1, pp. 209-214, 2012/01/10 2012.
- [58] D. M. Eisele *et al.*, "Utilizing redox-chemistry to elucidate the nature of exciton transitions in supramolecular dye nanotubes," *Nature Chemistry*, Article vol. 4, p. 655, 07/01/online 2012.
- [59] K. A. Clark, C. W. Cone, and D. A. Vanden Bout, "Quantifying the Polarization of Exciton Transitions in Double-Walled Nanotubular J-Aggregates," *The Journal of Physical Chemistry C*, vol. 117, no. 50, pp. 26473-26481, 2013/12/19 2013.
- [60] J. Yuen-Zhou *et al.*, "Coherent Exciton Dynamics in Supramolecular Light-Harvesting Nanotubes Revealed by Ultrafast Quantum Process Tomography," *ACS Nano*, vol. 8, no. 6, pp. 5527-5534, 2014/06/24 2014.
- [61] K. A. Clark, E. L. Krueger, and D. A. Vanden Bout, "Direct Measurement of Energy Migration in Supramolecular Carbocyanine Dye Nanotubes," *The Journal of Physical Chemistry Letters*, vol. 5, no. 13, pp. 2274-2282, 2014/07/03 2014.
- [62] D. M. Eisele *et al.*, "Robust excitons inhabit soft supramolecular nanotubes," *Proceedings of the National Academy of Sciences*, vol. 111, no. 33, pp. E3367-E3375, August 19, 2014 2014.
- [63] B. Kriete *et al.*, "Steering Self-Assembly of Amphiphilic Molecular Nanostructures via Halogen Exchange," *The Journal of Physical Chemistry Letters*, vol. 8, no. 13, pp. 2895-2901, 2017/07/06 2017.

- [64] H. von Berlepsch *et al.*, "Surfactant-Induced Changes of Morphology of J-Aggregates: Superhelix-to-Tubule Transformation," *Langmuir*, vol. 16, no. 14, pp. 5908-5916, 2000/07/01 2000.
- [65] H. von Berlepsch, S. Kirstein, and C. Böttcher, "Controlling the Helicity of Tubular J-Aggregates by Chiral Alcohols," *The Journal of Physical Chemistry B*, vol. 107, no. 36, pp. 9646-9654, 2003/09/01 2003.
- [66] G. Y. Guralchuk *et al.*, "Anomalous Surfactant-Induced Enhancement of Luminescence Quantum Yield of Cyanine Dye J-Aggregates," *The Journal of Physical Chemistry C*, vol. 112, no. 38, pp. 14762-14768, 2008/09/25 2008.
- [67] S. MUKHOPADHYAY and U. MAITRA, "Chemistry and biology of bile acids," *Current science*, vol. 87, no. 12, pp. 1666-1683, 2004.
- [68] P. Terech, B. Jean, and F. Ne, "Hexagonally Ordered Ammonium Lithocholate Self-Assembled Nanotubes with Highly Monodisperse Sections," *Advanced Materials*, vol. 18, no. 12, pp. 1571-1574, 2006.
- [69] P. Terech, N. M. Sangeetha, S. Bhat, J.-J. Allegraud, and E. Buhler, "Ammonium lithocholate nanotubes: stability and copper metallization," *Soft Matter*, vol. 2, no. 6, pp. 517-522, 2006.
- [70] A. Pal, H. Basit, S. Sen, V. K. Aswal, and S. Bhattacharya, "Structure and properties of two component hydrogels comprising lithocholic acid and organic amines," *Journal of Materials Chemistry*, vol. 19, no. 25, pp. 4325-4334, 2009.
- [71] X. Zhang, M. Mathew, A. J. Gesquiere, and J. Fang, "Fluorescent composite tubes with pH-controlled shapes," *Journal of Materials Chemistry*, vol. 20, no. 18, pp. 3716-3721, 2010.

- [72] K. Tamhane, X. Zhang, J. Zou, and J. Fang, "Assembly and disassembly of tubular spherulites," *Soft Matter*, vol. 6, no. 6, pp. 1224-1228, 2010.
- [73] P. Terech, S. KP Velu, P. Pernot, and L. Wiegart, "Salt effects in the formation of self-assembled lithocholate helical ribbons and tubes," *The Journal of Physical Chemistry B*, vol. 116, no. 36, pp. 11344-11355, 2012.
- [74] X. Zhang, T. Bera, W. Liang, and J. Fang, "Longitudinal zipping/unzipping of self-assembled organic tubes," *The Journal of Physical Chemistry B*, vol. 115, no. 49, pp. 14445-14449, 2011.
- [75] C. Liu, J. Cui, A. Song, and J. Hao, "A bile acid-induced aggregation transition and rheological properties in its mixtures with alkyltrimethylammonium hydroxide," *Soft Matter*, vol. 7, no. 19, pp. 8952-8960, 2011.
- [76] H. Wang, W. Xu, S. Song, L. Feng, A. Song, and J. Hao, "Hydrogels facilitated by monovalent cations and their use as efficient dye adsorbents," *The Journal of Physical Chemistry B*, vol. 118, no. 17, pp. 4693-4701, 2014.
- [77] M. Gubitosi *et al.*, "Tailoring supramolecular nanotubes by bile salt based surfactant mixtures," *Angewandte Chemie International Edition*, vol. 54, no. 24, pp. 7018-7021, 2015.
- [78] W. Liang, S. He, and J. Fang, "Self-assembly of J-aggregate nanotubes and their applications for sensing dopamine," *Langmuir*, vol. 30, no. 3, pp. 805-811, 2014.
- [79] M. Wang *et al.*, "Accelerated photobleaching of a cyanine dye in the presence of a ternary target DNA, PNA probe, dye catalytic complex: a molecular diagnostic," *Analytical chemistry*, vol. 81, no. 6, pp. 2043-2052, 2009.

- [80] W. J. Griffiths and J. Sjövall, "Bile acids: analysis in biological fluids and tissues," *Journal of lipid research*, vol. 51, no. 1, pp. 23-41, 2010.
- [81] A. F. Hofmann and A. Roda, "Physicochemical properties of bile acids and their relationship to biological properties: an overview of the problem," *Journal of lipid research*, vol. 25, no. 13, pp. 1477-1489, 1984.
- [82] A. G. Shtukenberg, Y. O. Punin, E. Gunn, and B. Kahr, "Spherulites," *Chemical reviews*, vol. 112, no. 3, pp. 1805-1838, 2011.
- [83] M. R. Krebs, C. E. MacPhee, A. F. Miller, I. E. Dunlop, C. M. Dobson, and A. M. Donald, "The formation of spherulites by amyloid fibrils of bovine insulin," *Proceedings of the National Academy of Sciences of the United States of America*, vol. 101, no. 40, pp. 14420-14424, 2004.
- [84] M. Krebs, E. Bromley, S. Rogers, and A. Donald, "The mechanism of amyloid spherulite formation by bovine insulin," *Biophysical journal*, vol. 88, no. 3, pp. 2013-2021, 2005.
- [85] K. Eden, R. Morris, J. Gillam, C. E. MacPhee, and R. J. Allen, "Competition between primary nucleation and autocatalysis in amyloid fibril self-assembly," *Biophysical journal*, vol. 108, no. 3, pp. 632-643, 2015.
- [86] C. J. O'Connor and R. G. Wallace, "Physico-chemical behavior of bile salts," *Advances in Colloid and Interface Science*, vol. 22, no. 1, pp. 1-111, 1985.
- [87] G. Li and L. B. McGown, "A new approach to polydispersity studies of sodium taurocholate and sodium taurodeoxycholate aggregates using dynamic fluorescence anisotropy," *The Journal of Physical Chemistry*, vol. 97, no. 25, pp. 6745-6752, 1993.
- [88] C. Ju and C. Böhne, "Dynamics of probe complexation to bile salt aggregates," *The Journal of Physical Chemistry*, vol. 100, no. 9, pp. 3847-3854, 1996.

- [89] F. J. Hoeben, P. Jonkheijm, E. Meijer, and A. P. Schenning, "About supramolecular assemblies of π -conjugated systems," *Chemical Reviews*, vol. 105, no. 4, pp. 1491-1546, 2005.
- [90] Z. Chen, A. Lohr, C. R. Saha-Möller, and F. Würthner, "Self-assembled π -stacks of functional dyes in solution: structural and thermodynamic features," *Chemical Society Reviews*, vol. 38, no. 2, pp. 564-584, 2009.
- [91] V. Faramarzi *et al.*, "Light-triggered self-construction of supramolecular organic nanowires as metallic interconnects," *Nature chemistry*, vol. 4, no. 6, p. 485, 2012.
- [92] A. T. Haedler *et al.*, "Long-range energy transport in single supramolecular nanofibres at room temperature," *Nature*, vol. 523, no. 7559, p. 196, 2015.
- [93] A. Jain and S. J. George, "New directions in supramolecular electronics," *Materials Today*, vol. 18, no. 4, pp. 206-214, 2015.
- [94] X. Li *et al.*, "Uniform electroactive fibre-like micelle nanowires for organic electronics," *Nature communications*, vol. 8, p. 15909, 2017.
- [95] B. Green and W. W. Parson, *Light-harvesting antennas in photosynthesis*. Springer Science & Business Media, 2003.
- [96] D. M. Eisele, J. Knoester, S. Kirstein, J. P. Rabe, and D. A. V. Bout, "Uniform exciton fluorescence from individual molecular nanotubes immobilized on solid substrates," *Nature nanotechnology*, vol. 4, no. 10, pp. 658-663, 2009.
- [97] F. S. Freyria *et al.*, "Near-Infrared Quantum Dot Emission Enhanced by Stabilized Self-Assembled J-Aggregate Antennas," *Nano letters*, vol. 17, no. 12, pp. 7665-7674, 2017.

- [98] Z. Chen *et al.*, "Near-IR Absorbing J-Aggregate of an Amphiphilic BF2-Azadipyrrromethene Dye by Kinetic Cooperative Self-Assembly," *Angewandte Chemie International Edition*, vol. 56, no. 21, pp. 5729-5733, 2017.
- [99] H. v. Berlepsch and C. Böttcher, "H-aggregates of an indocyanine Cy5 dye: transition from strong to weak molecular coupling," *The Journal of Physical Chemistry B*, vol. 119, no. 35, pp. 11900-11909, 2015.
- [100] K. C. Hannah and B. A. Armitage, "DNA-templated assembly of helical cyanine dye aggregates: a supramolecular chain polymerization," *Accounts of chemical research*, vol. 37, no. 11, pp. 845-853, 2004.
- [101] O.-K. Kim, J. Je, G. Jernigan, L. Buckley, and D. Whitten, "Super-helix formation induced by cyanine J-aggregates onto random-coil carboxymethyl amylose as template," *Journal of the American Chemical Society*, vol. 128, no. 2, pp. 510-516, 2006.
- [102] P. Makam and E. Gazit, "Minimalistic peptide supramolecular co-assembly: expanding the conformational space for nanotechnology," *Chemical Society Reviews*, 10.1039/C7CS00827A 2018.
- [103] Y. Tsuchiya, T. Noguchi, D. Yoshihara, B. Roy, T. Yamamoto, and S. Shinkai, "Conformation Control of a Conjugated Polymer through Complexation with Bile Acids Generates Its Novel Spectral and Morphological Properties," *Langmuir*, vol. 32, no. 47, pp. 12403-12412, 2016.
- [104] S. Rhodes, W. Liang, E. Shteinberg, and J. Fang, "Formation of Spherulitic J-Aggregates from the Coassembly of Lithocholic Acid and Cyanine Dye," *The Journal of Physical Chemistry Letters*, vol. 8, no. 18, pp. 4504-4509, 2017/09/21 2017.

- [105] H. Yao, K. Domoto, T. Isohashi, and K. Kimura, "In situ detection of birefringent mesoscopic H and J aggregates of thiacyanocyanine dye in solution," *Langmuir*, vol. 21, no. 3, pp. 1067-1073, 2005.
- [106] T. Eder *et al.*, "Switching between H-and J-type electronic coupling in single conjugated polymer aggregates," *Nature Communications*, vol. 8, no. 1, p. 1641, 2017.
- [107] I. Fedorov, I. Bobrinetskiy, B. Shapiro, A. Romashkin, and V. Nevolin, "Photoelectric response of thiamonomethinecyanine J-aggregate nanoribbons deposited via dielectrophoresis technique," *Physics Letters A*, vol. 378, no. 3, pp. 226-228, 2014.
- [108] B. J. Walker, A. Dorn, V. Bulovic, and M. G. Bawendi, "Color-selective photocurrent enhancement in coupled J-aggregate/nanowires formed in solution," *Nano letters*, vol. 11, no. 7, pp. 2655-2659, 2011.
- [109] J. Bredas, R. Silbey, D. Boudreaux, and R. Chance, "Chain-length dependence of electronic and electrochemical properties of conjugated systems: polyacetylene, polyphenylene, polythiophene, and polypyrrole," *Journal of the American Chemical Society*, vol. 105, no. 22, pp. 6555-6559, 1983.
- [110] A. Bilić, J. R. Reimers, N. S. Hush, and J. Hafner, "Adsorption of ammonia on the gold (111) surface," *The Journal of chemical physics*, vol. 116, no. 20, pp. 8981-8987, 2002.
- [111] A. Kahn, "Fermi level, work function and vacuum level," *Materials Horizons*, vol. 3, no. 1, pp. 7-10, 2016.
- [112] A. Chowdhury, S. Wachsmann-Hogiu, P. R. Bangal, I. Raheem, and L. A. Peteanu, "Characterization of chiral H and J aggregates of cyanine dyes formed by DNA templating using stark and fluorescence spectroscopies," *The Journal of Physical Chemistry B*, vol. 105, no. 48, pp. 12196-12201, 2001.

- [113] E. Rousseau, M. Van der Auweraer, and F. De Schryver, "Steady-state and time-resolved spectroscopy of a self-assembled cyanine dye multilayer," *Langmuir*, vol. 16, no. 23, pp. 8865-8870, 2000.
- [114] Y. Chiu, K. Mittal, and P. Bothorel, "Surfactants in Solution," ed: Plenum, 1986.
- [115] M. S. Spector, J. V. Selinger, and J. M. Schnur, *Chiral molecular self-assembly*. John Wiley & Sons, Inc.: Hoboken, NJ, 2004.
- [116] G. Briganti, A. A. D'Archivio, L. Galantini, and E. Giglio, "Structural study of the micellar aggregates of sodium and rubidium glyco-and taurodeoxycholate," *Langmuir*, vol. 12, no. 5, pp. 1180-1187, 1996.
- [117] G. D. Scholes, G. R. Fleming, A. Olaya-Castro, and R. Van Grondelle, "Lessons from nature about solar light harvesting," *Nature chemistry*, vol. 3, no. 10, pp. 763-774, 2011.
- [118] S. Sengupta and F. Würthner, "Chlorophyll J-aggregates: From bioinspired dye stacks to nanotubes, liquid crystals, and biosupramolecular electronics," *Accounts of chemical research*, vol. 46, no. 11, pp. 2498-2512, 2013.
- [119] S. K. Saikin, A. Eisfeld, S. Valleau, and A. Aspuru-Guzik, "Photonics meets excitonics: natural and artificial molecular aggregates," *Nanophotonics*, vol. 2, no. 1, pp. 21-38, 2013.
- [120] T. Tani, *J-aggregates in spectral sensitization of photographic materials*. World Scientific: Singapore, 1996.
- [121] E. Collini, C. Ferrante, R. Bozio, A. Lodi, and G. Ponterini, "Large third-order nonlinear optical response of porphyrin J-aggregates oriented in self-assembled thin films," *Journal of Materials Chemistry*, vol. 16, no. 16, pp. 1573-1578, 2006.

- [122] L. Cui *et al.*, "Organized Aggregation of Porphyrins in Lipid Bilayers for Third Harmonic Generation Microscopy," *Angewandte Chemie International Edition*, vol. 54, no. 47, pp. 13928-13932, 2015.
- [123] M. Era, C. Adachi, T. Tsutsui, and S. Saito, "Double-heterostructure electroluminescent device with cyanine-dye bimolecular layer as an emitter," *Chemical physics letters*, vol. 178, no. 5-6, pp. 488-490, 1991.
- [124] E. I. Mal'tsev *et al.*, "Electroluminescence of polymer/J-aggregate composites," *Applied physics letters*, vol. 75, no. 13, pp. 1896-1898, 1999.
- [125] S. Spencer *et al.*, "Critical electron transfer rates for exciton dissociation governed by extent of crystallinity in small molecule organic photovoltaics," *The Journal of Physical Chemistry C*, vol. 118, no. 27, pp. 14840-14847, 2014.
- [126] G. Chen *et al.*, "J-aggregation of a squaraine dye and its application in organic photovoltaic cells," *Journal of Materials Chemistry C*, vol. 1, no. 40, pp. 6547-6552, 2013.
- [127] R. M. Jones, L. Lu, R. Helgeson, T. S. Bergstedt, D. W. McBranch, and D. G. Whitten, "Building highly sensitive dye assemblies for biosensing from molecular building blocks," *Proceedings of the National Academy of Sciences*, vol. 98, no. 26, pp. 14769-14772, 2001.
- [128] K. K. Ng *et al.*, "Stimuli-responsive photoacoustic nanoswitch for in vivo sensing applications," *ACS nano*, vol. 8, no. 8, pp. 8363-8373, 2014.
- [129] M. Wang, G. L. Silva, and B. A. Armitage, "DNA-templated formation of a helical cyanine dye J-aggregate," *Journal of the American Chemical Society*, vol. 122, no. 41, pp. 9977-9986, 2000.

- [130] H. v. Berlepsch, E. Brandenburg, B. Koksche, and C. Böttcher, "Peptide adsorption to cyanine dye aggregates revealed by cryo-transmission electron microscopy," *Langmuir*, vol. 26, no. 13, pp. 11452-11460, 2010.
- [131] J. H. Kim, M. Lee, J. S. Lee, and C. B. Park, "Self-Assembled Light-Harvesting Peptide Nanotubes for Mimicking Natural Photosynthesis," *Angewandte Chemie International Edition*, vol. 51, no. 2, pp. 517-520, 2012.
- [132] M. Jaber, S. W. Robinson, C. Missale, and M. G. Caron, "Dopamine receptors and brain function," *Neuropharmacology*, vol. 35, no. 11, pp. 1503-1519, 1996.
- [133] A. Bowirrat and M. Oscar-Berman, "Relationship between dopaminergic neurotransmission, alcoholism, and reward deficiency syndrome," *American Journal of Medical Genetics Part B: Neuropsychiatric Genetics*, vol. 132, no. 1, pp. 29-37, 2005.
- [134] D. J. Wiedemann, K. T. Kawagoe, R. T. Kennedy, E. L. Ciolkowski, and R. M. Wightman, "Strategies for low detection limit measurements with cyclic voltammetry," *Analytical chemistry*, vol. 63, no. 24, pp. 2965-2970, 1991.
- [135] D. W. Arrigan, M. Ghita, and V. Beni, "Selective voltammetric detection of dopamine in the presence of ascorbate," *Chemical Communications*, no. 6, pp. 732-733, 2004.
- [136] Y. H. Park, X. Zhang, S. S. Rubakhin, and J. V. Sweedler, "Independent optimization of capillary electrophoresis separation and native fluorescence detection conditions for indolamine and catecholamine measurements," *Analytical chemistry*, vol. 71, no. 21, pp. 4997-5002, 1999.
- [137] J. R. Thabano, M. C. Breadmore, J. P. Hutchinson, C. Johns, and P. R. Haddad, "Capillary electrophoresis of neurotransmitters using in-line solid-phase extraction and preconcentration using a methacrylate-based weak cation-exchange monolithic stationary

- phase and a pH step gradient," *Journal of Chromatography A*, vol. 1175, no. 1, pp. 117-126, 2007.
- [138] V. Carrera, E. Sabater, E. Vilanova, and M. A. Sogorb, "A simple and rapid HPLC–MS method for the simultaneous determination of epinephrine, norepinephrine, dopamine and 5-hydroxytryptamine: Application to the secretion of bovine chromaffin cell cultures," *Journal of Chromatography B*, vol. 847, no. 2, pp. 88-94, 2007.
- [139] Y. Qiao *et al.*, "Unique temperature-dependent supramolecular self-assembly: from hierarchical 1D nanostructures to super hydrogel," *The Journal of Physical Chemistry B*, vol. 114, no. 36, pp. 11725-11730, 2010.
- [140] G. F. Bassani and V. Agranovich, *Electronic excitations in organic based nanostructures*. Academic Press, 2003.
- [141] A. V. Sorokin, I. I. Filimonova, R. S. Grynyov, G. Y. Guralchuk, S. L. Yefimova, and Y. V. Malyukin, "Control of exciton migration efficiency in disordered J-aggregates," *The Journal of Physical Chemistry C*, vol. 114, no. 2, pp. 1299-1305, 2009.
- [142] A. Klegeris, L. G. Korkina, and S. A. Greenfield, "Autoxidation of dopamine: a comparison of luminescent and spectrophotometric detection in basic solutions," *Free Radical Biology and Medicine*, vol. 18, no. 2, pp. 215-222, 1995.
- [143] I. L. Medintz *et al.*, "Quantum-dot/dopamine bioconjugates function as redox coupled assemblies for in vitro and intracellular pH sensing," *Nature materials*, vol. 9, no. 8, pp. 676-684, 2010.
- [144] H. Lee, S. M. Dellatore, W. M. Miller, and P. B. Messersmith, "Mussel-inspired surface chemistry for multifunctional coatings," *science*, vol. 318, no. 5849, pp. 426-430, 2007.

- [145] M. Mohamed, A. H. Eichborn, and S. H. Eichborn, "Measurement and prediction of electronic properties of discotic triphenylenes and phtalocianines," *ECS Transactions*, vol. 25, pp. 1-10, 2010.
- [146] H. Mohammad-Shiri, M. Ghaemi, S. Riahi, and A. Akbari-Sehat, "Computational and electrochemical studies on the redox reaction of dopamine in aqueous solution," *Int. J. Electrochem. Sci*, vol. 6, pp. 317-336, 2011.
- [147] T. M. Dawson and V. L. Dawson, "Molecular pathways of neurodegeneration in Parkinson's disease," *Science*, vol. 302, no. 5646, pp. 819-822, 2003.
- [148] T. Zetterström, T. Sharp, C. Marsden, and U. Ungerstedt, "In vivo measurement of dopamine and its metabolites by intracerebral dialysis: Changes after D-amphetamine," *Journal of neurochemistry*, vol. 41, no. 6, pp. 1769-1773, 1983.